# A DIAGNOSTIC APPROACH TO OBTAINING PLANETARY BOUNDARY LAYER WINDS USING SATELLITE-DERIVED THERMAL DATA



Final Report
Contract NAS8-33370

by

Carol L. Belt
Henry E. Fuelberg

Department of Earth and Atmospheric Sciences
Saint Louis University
Saint Louis, Missouri 63103

Prepared for

George C. Marshall Space Flight Center
National Aeronautics and Space Administration
Marshall Space Flight Center, Alabama 35812

March 1984

# A DIAGNOSTIC APPROACH TO OBTAINING PLANETARY BOUNDARY LAYER WINDS USING SATELLITE-DERIVED THERMAL DATA

Final Report
Contract NAS8-33370

by

Carol L. Belt
Henry E. Fuelberg

Department of Earth and Atmospheric Sciences
Saint Louis University
Saint Louis, Missouri 63103

Prepared for

George C. Marshall Space Flight Center
National Aeronautics and Space Administration
Marshall Space Flight Center, Alabama 35812

March 1984

ABSTRACT

The feasibility of using satellite-derived thermal data to generate realistic synoptic-scale winds within the planetary boundary layer (PBL) is examined. Diagnostic "modified Ekman" wind equations from the Air Force Global Weather Central (AFGWC) Boundary Layer Model are used to compute winds at seven levels within the PBL transition layer (50 m to 1600 m AGL). Satellite-derived winds based on 62 predawn (0921 GMT 19 April 1979) TIROS-N soundings are compared to similarly-derived wind fields based on 39 AVE-SESAME II rawinsonde (RAOB) soundings taken 2 h later. Actual wind fields are also used as a basis for comparison. Qualitative and statistical comparisons show that the Ekman winds from both sources are in very close agreement, with an average vector correlation coefficient of 0.815. Best results are obtained at 300 m AGL. Satellite winds tend to be slightly weaker than their RAOB counterparts and exhibit a greater degree of cross-isobaric flow. The modified Ekman winds show a significant improvement over geostrophic values at levels nearest the surface.

Horizontal moisture divergence, moisture advection, velocity divergence and relative vorticity are computed at 300 m AGL using satellite-derived winds and moisture data. Results show excellent agreement with corresponding RAOB-derived values. Areas of horizontal moisture convergence, velocity convergence, and positive vorticity are nearly coincident and align in regions which later develop intense convection. Vertical motion at 1600 m AGL is computed using stepwise integration of the satellite winds through the PBL. Values and patterns are similar to those obtained using the RAOB-derived winds. Regions of maximum upward motion correspond with areas of greatest moisture convergence and the convection that later develops.

## ACKNOWLEDGMENTS

The authors gratefully acknowledge the many helpful suggestions of Drs. Gandikota V. Rao, Yeong-jer Lin and David O'C. Starr. Special thanks go to Mr. Gary Jedlovec for his assistance in data acquisition; the Technical Services Branch of AFGWC for providing information on the Boundary Layer Model; the USAF Environmental Technical Applications Center Library for background research; and particularly to Mr. Mark Fenbers for assisting in preliminary calculations, typing the manuscript and drafting the figures.

This research was sponsored in part by the National Aeronautics and Space Administration under Contract NAS8-33370 and is under the auspices of the Atmospheric Sciences Division, Systems Dynamics Laboratory, NASA Marshall Space Flight Center, Alabama. The author is also indebted to the Air Force Institute of Technology for providing a scholarship to Saint Louis University.

TABLE OF CONTENTS

TABLE OF CONTENTS (CONTINUED)

TABLE OF CONTENTS (CONTINUED)

## LIST OF TABLES

## LIST OF FIGURES

LIST OF FIGURES (CONTINUED)

LIST OF FIGURES (CONTINUED)

# 1. INTRODUCTION

## a. Background

Radiosonde observations (RAOBs) have traditionally been the primary source of meteorological data above the earth's surface. Increasingly, however, weather satellite systems are becoming a major contributor of valuable sounding data that were previously unattainable. As noted by Scoggins et al. (1981), this new data source can greatly enhance our knowledge of atmospheric structure in that: 1) satellite soundings can be made on a global scale with greater time and space resolution than is possible with the current RAOB network; 2) all measurements are made by the same instrument, eliminating errors resulting from the variability between radiosondes; and 3) a satellite measures the entire vertical extent of the sounding almost instantaneously, thereby eliminating errors due to downstream drift of radiosonde balloons.

An inherent difference between a satellite sounding system and a conventional radiosonde is that a satellite measurement describes mean temperature and humidity within a volume of the atmosphere, whereas a radiosonde measures these parameters on a point-by-point basis. And, as noted by Shen et al. (1975),

> "although the radiosonde is capable of observing with much higher vertical resolution than is the remote satellite sounder (meters compared to kilometers), the satellite sounding system usually can

> achieve much higher spatial resolution and more meaningful horizontal gradients than those possible with a practical radiosonde network".

Another difference between the two systems is that the presence of clouds adversely affects satellite soundings, but has little effect on radiosonde measurements.

One way in which our knowledge of atmospheric motion is being significantly improved is by obtaining wind fields from satellite data. Current satellite sensors do not directly measure winds; however, these systems do provide sufficient information from which wind profiles can be computed. Two popular techniques for ascertaining wind fields are cloud tracking and use of thermal wind relationships.

Cloud-derived winds are based on the assumption that certain clouds, especially small cumulus and cirrus, move at or near the environmental wind velocity in which they are embedded. This assumption has been verified through *in situ* aircraft studies by Hasler *et al.* (1977) and Hasler *et al.* (1979). Several earlier studies found favorable relationships between cloud-derived winds and the observed flow, notably Hubert and Whitney (1971), Fujita *et al.* (1975), and Suchman and Martin (1976). More recent studies have employed satellite cloud motion techniques to successfully compute divergence (Peslen, 1980), kinematic vertical motion (Wilson and Houghton, 1979) and low-level moisture convergence (Negri and Vonder

Haar, 1980). Although cloud tracking has been shown to be a valuable method for describing wind flow, the procedure has several limitations. First, the time required for cloud tracking at several levels may be extensive, even when interactive computer methods are used (Johnson and Suchman, 1980). Second, trackable clouds may not be present at the areas and levels of interest, or may be obscured by clouds at higher levels.

Application of thermal wind relations to satellite-derived temperature data provides an alternate or supplemental source of information about atmospheric flow. This procedure calls for the addition of geopotential thickness, derived from satellite data, to known height values at a "tie-on" level (often the surface), thereby yielding the geopotential field at the level of interest. From this field, geostrophic winds may be computed. Favorable results from the thermal wind technique have been obtained by examining cross-sections through baroclinic zones which were based on Nimbus 5-derived temperature data (Smith and Woolf, 1974; Shen et al., 1975; Smith et al., 1975; Arnold et al., 1976; Horn et al., 1976). Peterson and Horn (1977) used Nimbus 6 thermal data to obtain geopotential heights and geostrophic winds; their results showed good agreement with bracketing data from the National Meteorological Center (NMC) and had good continuity during the three day period of study. Moyer et al. (1978) determined that Nimbus 6-derived winds were sufficiently accurate to describe the

major features of synoptic-scale systems apparent on constant-pressure charts obtained from RAOB data.

Several more elaborate techniques for obtaining thermally-derived winds have been tested recently using TIROS-N soundings. Mancuso and Endlich (1980) employed TIROS-N data in combination with GOES (Geostationary Operational Environmental Satellite) cloud-motion measurements to test several procedures for determining satellite-derived wind profiles. Their techniques included (a) using the thermal wind to build upward or downward from the cloud-motion level, (b) introducing the balance relationship to (a), and (c) using an eigenvector approach. The eigenvector procedure, based on the use of an initial gradient wind profile that is built upward from the given surface winds, provided the most representative results.

The studies described above were concerned primarily with deriving wind fields in the free atmosphere --- that part of the atmosphere beginning above the "geostrophic (or gradient) wind level". To the author's knowledge, the only study thus far to apply satellite thermal data to wind computations in the planetary boundary layer (PBL) was performed by Carle and Scoggins (1981). Sounding data from Nimbus 6 were used to derive geostrophic wind fields at the mandatory pressure levels (850 mb, 700 mb, etc.); the logarithmic wind law (Hess, 1959) was then applied to "extrapolate" through the PBL (selected as <

150 m) to compute surface wind speed and direction. Surface winds were not calculated in the western United States due to the method's inability to handle large variabilities in terrain height. However, in areas where surface winds were computed, the logarithmic wind law produced results which agreed well with observed values in most regions.

b. Statement of the problem

Further study into the feasibility of using satellite-derived thermal data to obtain wind fields in the planetary boundary layer seems justified. With satellite technology providing an ever-improving product (the most recent is the geosynchronous VAS* system), it is reasonable to assume that research aimed towards blending satellite data directly into operational boundary layer models will soon begin. Such research, if successful, offers several potential benefits. Satellite-derived PBL winds could yield an improved method of determining low-level horizontal moisture convergence, already shown to be a precursor of many severe storm outbreaks (Hudson, 1971; Negri and Vonder Haar, 1980). Procedures dealing with other kinematic parameters (e.g., low-level divergence and vorticity) would also benefit from the improved data source. The addition of satellite-derived data into stability indices which

* Visible Infrared Spin Scan Radiometer (VISSR) Atmospheric Sounder

incorporate low-level wind speed and direction (e.g., the Air Force Global Weather Central (AFGWC) Severe WEAther Threat (SWEAT) Index) would help to better define potential areas of severe convective weather.

The research documented in the following pages expands upon the initial effort of Carle and Scoggins (1981) by examining the feasibility of using satellite-derived temperature data to compute winds at several levels within the planetary boundary layer. The study is diagnostic in nature; prognostic and operational applications are subjects for future research. The main goal of the investigation is to obtain meaningful horizontal wind fields and vertical wind profiles in the lowest 1600 m of the atmosphere. A secondary goal is to combine these winds with humidity data to define areas of horizontal moisture convergence, hopefully leading to the identification of potential regions of intense convection.

TIROS-N sounding data collected during the 1979 Atmospheric Variability Experiment-Severe Environmental Storms and Mesoscale Experiments (AVE-SESAME '79) are incorporated into the thermal wind relation and modified Ekman equations contained in the AFGWC Boundary Layer Model (AFGWC-BLM). Described in detail by Hadeen and Friend (1972), the model has been operational since March 1969 and is based on work by Gerrity (1967). In particular, data from AVE-SESAME II (19 April

1979) are employed. RAOB soundings for this period are used as a basis for comparing the computed satellite-derived wind values.

Before outlining in greater detail the methodology of this investigation (Chapter 5), it is prudent to review the phenomenology of the problem. An examination of the characteristics and classic formulations of the PBL (Chapter 2) will be followed by pertinent details of the AFGWC Boundary Layer Model (Chapter 3). In Chapter 4, the TIROS-N and RAOB sounding data will be described. Finally, results of the study will be presented in Chapter 6.

## 2. REVIEW OF THE PBL THEORY

### a. PBL structure

The planetary boundary layer occupies the atmospheric domain nearest the earth, wherein wind shear and/or thermal convection give rise to small-scale turbulence (Deardorff, 1972). As noted by Sutton (1977), the PBL may be subdivided into two layers: A shallow surface (constant flux) layer, lying immediately adjacent to the earth, extends to a height of $\sim$50 m and is characterized by eddy stresses which are nearly constant with height and which are an order of magnitude greater than the horizontal pressure gradient and Coriolis forces. The vertical wind speed profile, with wind direction assumed constant with height, is determined primarily by the vertical temperature gradient and the nature of the underlying terrain.

The Ekman (transition) layer extends from the surface layer to the lower boundary of the free atmosphere (where the atmosphere is treated as an ideal fluid in geostrophic equilibrium), a height of 1-2 km. In this layer of transition from the disturbed flow near the surface to the (supposedly) smooth flow of the free atmosphere, the wind profile is determined by a balance between the pressure gradient force, Coriolis force, and residual frictional effects of the earth's surface. Here,

turbulent eddy stress is the same order of magnitude as the pressure gradient and Coriolis forces. Above the PBL, turbulent transport is caused by clear air turbulence (associated with internal gravity waves), towering cumulus clouds, and terrain effects on a scale large enough to cause upward propagation of energy through the PBL (Deardorff, 1972).

b. Classic surface layer formulations

Parameterization of turbulent transport has proven historically to be the main stumbling block for PBL modelers. The eddy viscosity method, or "K-theory", has long been used to simulate boundary layer flow (Estoque, 1973; Sutton, 1977; Krishna, 1981). Analogous to molecular turbulence theory, eddy stresses are assumed to be proportional to the product of the shear of a scalar quantity (such as heat or a component of momentum) and an eddy exchange coefficient (eddy conductivity or eddy viscosity, respectively). In terms of momentum transfer and the mean vertical wind shear, for example,

$$\left.\begin{aligned} \tau_{xz} &= -\bar{\rho}\,\overline{u'w'} = K_m\,\bar{\rho}\,\frac{\partial \bar{u}}{\partial z} \\ \text{and} \qquad \tau_{yz} &= -\bar{\rho}\,\overline{v'w'} = K_m\,\bar{\rho}\,\frac{\partial \bar{v}}{\partial z}. \end{aligned}\right\} \tag{2-1}$$

where $\tau_{ij}$ $(= -\bar{\rho}\overline{u_i'u_j'})$ is the appropriate Reynolds' stress, $\bar{\rho}$ denotes density and $K_m$ is the eddy viscosity. Since the eddy stresses are expressed directly in terms of the gradients of

mean motion, K-theory is referred to as a "first-order closure" scheme. Prandtl (1934) extended the exchange coefficient hypothesis by introducing the mixing length, similar to the molecular mean free path:

$$\left.\begin{aligned} K_m &= l^2\left|\frac{\partial \overline{u}}{\partial z}\right| \\ \text{and} \qquad & \\ K_m &= l^2\left|\frac{\partial \overline{v}}{\partial z}\right|. \end{aligned}\right\} \tag{2-2}$$

where the mixing length $l$ represents the mean distance that a turbulent eddy with excess momentum $u'$(or $v'$) will travel before blending in with the environment. In a surface layer exhibiting neutral static stability, the mixing length is zero at the surface and increases linearly with height, such that $l = kz$ where $k$ is the (dimensionless) von Karman constant ($\sim$0.4). Considering the subscripts in (2-1) to be "understood", substitution from (2-2) yields the general expression (see for example, Hess, 1959)

$$\tau = (kz)^2 \rho \left[\frac{\partial \overline{u}}{\partial z}\right]^2 \qquad \text{or} \qquad \frac{\partial \overline{u}}{\partial z} = \frac{u_*}{kz}, \tag{2-3}$$

where $u_* = \left[\frac{\tau}{\rho}\right]^{1/2}$ is termed the frictional velocity. The eddy viscosity can thus be rewritten

$$K_m = (kz)^2 \frac{\partial \overline{u}}{\partial z} = kzu_* . \tag{2-4}$$

Integration of (2-3) produces the well known logarithmic wind profile for a neutral surface layer

$$\overline{u}(z) = \frac{u_*}{k} \ln\left[\frac{z}{z_o}\right]. \tag{2-5}$$

where $z_o$ is the roughness parameter (denoting the level at which the mean wind speed is presumed to vanish). Under non-neutral conditions, (2-3) may be modified by employing the similarity theory of Monin and Obukhov (Haltiner and Williams, 1980), such that

$$\frac{\partial \overline{u}}{\partial z} = \frac{u_*}{kz}\,\varphi_m\left(\frac{z}{L}\right), \tag{2-6}$$

where $\varphi_m$ is an empirical function expressing the adjustment of the velocity profile due to conditions of non-neutral stability ($\varphi_m = 1$ for neutral stability), and $L$ is the Monin-Obukhov length

$$L = \frac{\overline{T}}{gk^2}\,\frac{u_*^2}{T_{*v}}, \qquad \text{where} \qquad T_{*v} = -\frac{\overline{w'\vartheta'}}{u_*}, \tag{2-7}$$

which indicates the height at which the magnitude of mechanical turbulence (due to Reynolds' stresses) equals the magnitude of thermally induced turbulence. Here, $T$ denotes temperature, $g$ indicates acceleration due to gravity, and $\vartheta$ represents potential temperature. Integration of (2-6) in the manner shown by Priestly (1959) yields

$$\overline{u}(z) = \frac{u_*}{k}\ln\left[\frac{z}{z_o}\right] + \frac{u_*}{k}\,\frac{\alpha z}{L}, \tag{2-8}$$

where $\alpha = 0.6$ is an empirical expansion coefficient. This may be termed the log-plus-linear wind profile. From (2-3) and (2-6) it can be shown that the eddy viscosity for the non-neutral surface layer is

$$K_m = \frac{ku_*z}{\varphi_m\left(\frac{z}{L}\right)}. \tag{2-9}$$

while the mixing length becomes

$$l = \frac{kz}{\varphi_m(\frac{z}{L})} . \tag{2-10}$$

Similarity theory and numerous empirical studies indicate that there are two principal turbulence regimes, viz., free and forced convection. The decision as to which regime is applicable is often based on the value of the Richardson number, $R_i$, which may be expressed (Gerrity, 1967)

$$R_i = \frac{g}{\vartheta}\left[\frac{\partial T}{\partial z} + \frac{g}{c_p}\right]\left[\frac{\partial s}{\partial z}\right]^{-2} . \tag{2-11}$$

The magnitude of the wind is denoted by $s$, while $c_p$ is the specific heat at constant pressure. The ratio $\left[\frac{z}{L}\right]$ can be expressed in terms of $R_i$ (see for example, Haltiner and Williams, 1980), and appropriate expressions for $K_m$ may be obtained (Estoque, 1963):

<u>For $R_i \geq -0.03$ (forced convection)</u>

$$K_m = [k(z + z_o)(1+\alpha R_i)]^2 \frac{\partial s}{\partial z} . \tag{2-12a}$$

<u>For $R_i \leq -0.03$ (free convection)</u>

$$K_m = C(z + z_o)^2 \left[\frac{g}{\vartheta}\right]^{1/2} \left|\frac{\partial \vartheta}{\partial z}\right|^{1/2} . \tag{2-12b}$$

An average value of $\alpha = -3.0$ was deduced from wind and temperature data collected for the Great Plains Turbulence Program (Lettau and Davidson, 1957). Priestly (1959) has shown the constant $C$ to be equal to 0.9. Various authors have studied the PBL turbulent flux (e.g., Dyer and Hicks, 1970; Hess <u>et</u>

al., 1981; Rubenstein, 1981) and wind profile data (e.g., Lettau and Davidson, 1957; Priestly, 1959; Boundary Layer Branch, 1967; Wieringa, 1980) from which $K_m$ can be computed. While $K_m$ is of the order of 1 $m^2$ $s^{-1}$ in the Ekman layer (Rao and Hassebrock, 1972), Priestly notes that, for example, near the surface (viz., 1.5 m above grassland) values around 0.25 $m^2$ $s^{-1}$ are typical in the presence of winds 4 m $s^{-1}$ and slight to moderate instability. The greater the instability, the greater will be the value of $K_m$.

c. Classic Ekman layer formations

Extension of K-theory to the remainder of the PBL above the surface layer has met with the difficulty of determining an appropriate form for the mixing length, upon which $K_m$ partly depends. The approach classically taken (Hess, 1959; Sutton, 1977; Haltiner and Williams, 1980) is to require that the eddy viscosity be constant with height and equal to the value at the top of the surface layer.

Characterizing the Ekman layer in its simplest form --- that of a steady, hydrostatically stable (neutrally buoyant) region --- the wind profile is classically obtained through manipulation of the horizontal equations of motion (see, for example, Estoque, 1973). Assuming (a) horizontal mean motion; (b) that horizontal mean wind shears are small compared to the

vertical mean wind shears; and (c) a balance among the Coriolis, pressure gradient and residual frictional forces, the momentum equations may be written

$$\left.\begin{aligned} \frac{1}{\rho}\frac{\partial \tau_x}{\partial z} + fv &= \frac{1}{\rho}\frac{\partial p}{\partial x} \\ \text{and} \\ \frac{1}{\rho}\frac{\partial \tau_y}{\partial z} - fu &= \frac{1}{\rho}\frac{\partial p}{\partial y}, \end{aligned}\right\} \qquad (2\text{-}13)$$

where $\tau_x$ and $\tau_y$ are defined by (2-1), and $f$ denotes the Coriolis parameter.

Further assumptions leading to the Ekman equations are that (d) $K_m$ is independent of height and (e) that the large-scale pressure gradient and density do not vary significantly with height and may be considered constant. This implies that the shearing stress, $\tau$, is a function of height only. Finally, it is assumed (f) that the geostrophic wind is constant with height $\left[\frac{\partial \vec{V}_g}{\partial z} = 0\right]$, with its components defined as

$$u_g = -\frac{1}{\rho f}\frac{\partial p}{\partial y} \qquad \text{and} \qquad v_g = \frac{1}{\rho}\frac{\partial p}{\partial x}.$$

Boundary conditions are chosen such that at

$$z = 0: \qquad u = v = 0,$$

and at

$$z = H: \qquad u = u_g, \quad v = v_g,$$

where $H$ denotes the top of PBL. Finally, assuming, for simplicity, that the geostrophic flow is entirely zonal ($v_g = 0$), the wind profile in the Ekman layer may be written (see, for exam-

ple, Holton (1979)

$$\left.\begin{aligned} u &= u_g\,[1 - e^{-mz}\cos(mz)] \\ \text{and} \\ v &= u_g\,[e^{-mz}\sin(mz)]. \end{aligned}\right\} \qquad (2\text{-}14)$$

where $m = \left[\frac{f}{2K_m}\right]^{1/2}$. Equations (2-14) combine through the relationship $\beta = \tan^{-1}\left[\frac{v}{u}\right]$ to produce the Ekman spiral, where $\beta$ represents the cross-isobaric angle. This relation describes the wind as turning clockwise (veering) with elevation through the PBL.

It must be noted that one or more of the assumptions made in deriving the classical Ekman spiral equations (2-14) may not be satisfied during individual cases. For example, the eddy viscosity is often, in reality, variable with height. As noted by Hess (1959), this should not prevent the wind flow from turning clockwise with elevation in the PBL, but may cause it to turn at a different rate than that described by the "spiral". Another point is that strong warm and cold air advection will cause the pressure gradient to change rapidly with height instead of remaining constant. Hoxit (1974) examined the effects of warm and cold air advection on geostrophic wind profiles. His findings suggested that the majority of observed vertical wind variability for the lowest 2.5 km is related to changes in stability, wind speed and/or the direction and magnitude of the thermal wind. Thermal stratification (stability) determined, to a large extent, the vertical distri-

distribution of turbulence (momentum transport). When geostrophic shear existed in the PBL, the vertical momentum transport was modified from that expected under barotropic conditions; this, in turn, modified the cross-isobaric angle. As noted by Hoxit, and later documented by Krishna (1981), the result is that warm (cold) air advection decreases (increases) the cross-isobaric angle of the surface wind and increases (reduces) the veering with height of the Ekman layer winds (Fig. 1).

A third factor concerning the classic Ekman spiral equations is the assumption that the geostrophic wind does not vary with height. This assumption is valid for barotropic conditions; however, as noted by Arya and Wyngaard (1975), the lower atmosphere is normally highly baroclinic, with geostrophic shears produced by large horizontal temperature gradients associated with various mesoscale systems. Lastly, if one is adhering strictly to the assumptions, (2-14) should be applied only to purely zonal geostrophic wind flow conditions.

Despite these deficiencies, first-order closure (K-theory) formulations, because of their mathematical simplicity, have been widely used and have provided acceptable results for many applications (Bodin, 1980).

d. Higher-order closure models

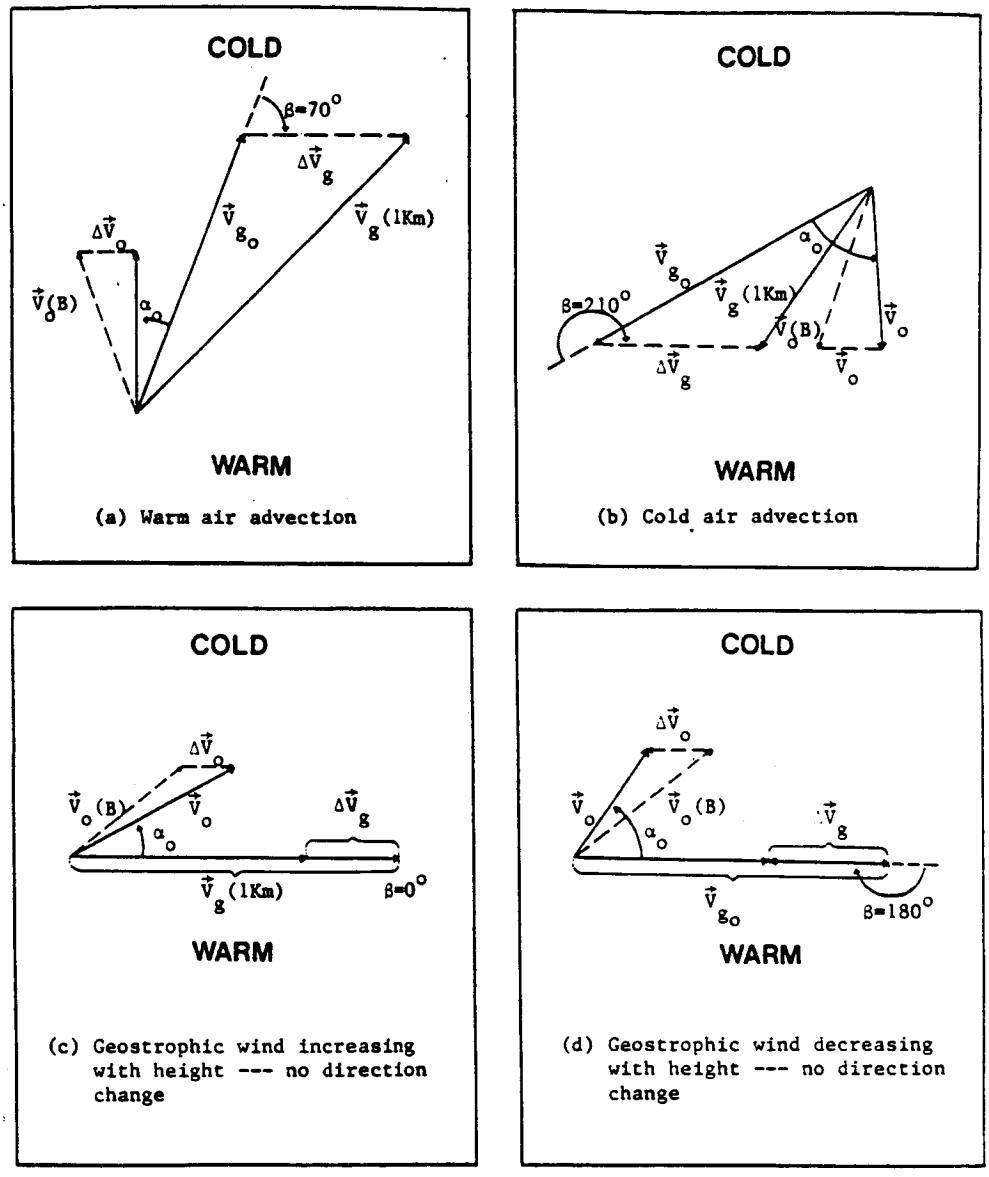


Fig. 1. Schematic examples of how additional downward momentum transport, resulting from geostrophic shear in the turbulent boundary layer, modifies the surface crossing angle from that expected in a barotropic atmosphere (after Hoxit, 1974). $\vec{V}_o$ denotes the surface wind vector; $\vec{V}_o(B)$, the surface wind vector for barotropic conditions; $\vec{V}_g$, the geostrophic wind vector; $\vec{V}_{g_o}$, the surface geostrophic wind vector; $\alpha_o$, the angle between the surface wind vector and surface isobars; and $\beta$, the angle measured clockwise from the direction of $\vec{V}_{g_o}$ to the direction of the mean thermal wind in the lowest 100 mb.

In recent years, various turbulent energy (higher-order closure) schemes have been under development. While the first-order schemes use the turbulent transfer coefficient $K$ ($K_m$ for momentum flux), the higher-order closure models use transfer coefficients in integrated flux form (Businger, 1973). The result is a considerable complication of the closure problem, leading to many additional equations for a complete model (see, for example, Mellor and Yamada, 1974; Wyngaard et al., 1974; Arya and Wyngaard, 1975; Haltiner and Williams, 1980). Such models require fairly fine-resolution input data (e.g., the Wangara Experiment data, described by Hess et al., 1981). The satellite data available for this study, however, have a much coarser resolution, with only one time period available for use. Although the higher-order schemes provide an improvement upon the classic K-theory formulations as regards detail of analysis, such procedures are beyond the scope of the current investigation, which focuses on a simpler parameterization of the mean properties of the PBL.

## 3. THE AFGWC BOUNDARY LAYER MODEL

The AFGWC Boundary Layer Model generates prognostic temperature values which are inserted into diagnostic wind equations to yield three-dimensional wind fields in the lowest 1600 m of the atmosphere (Hadeen and Friend, 1972). Based on work by Gerrity (1967), the horizontal wind flow is deduced using a modified version of the Ekman spiral equations described in Chapter 2. A goal of the current research is to obtain meaningful "satellite-derived" horizontal wind fields by inserting observed TIROS-N thermal data into Gerrity's modified Ekman equations. Pertinent equations from the model are presented in this chapter, with detailed derivations provided in Appendix A.

### a. Fundamental aspects of the model

A terrain-following coordinate system derived for a spherical, rotating earth (Gerrity, 1967) is employed in the AFGWC-BLM. The model coordinates are defined

$$x = a\, n(\varphi) \cos\varphi \cos\lambda,$$

$$y = a\, n(\varphi) \cos\varphi \sin\lambda,$$

$$z = r_e - a - E(x,y),$$

where $(r_e,\varphi,\lambda)$ are the spherical coordinates; "$a$" is the mean radius of the earth; $E(x,y)$ is the elevation, in meters, of the terrain above mean sea level; and $n(\varphi)$ is the polar stereographic map scale factor.

The model defines the PBL as the region between $z = 0$ and $z = H$, where $H$ = 1600 m (Hadeen, 1970). The surface layer occupies $0 \leq z \leq h$ where $h$ = 50 m, while the transition layer occupies $h \leq z \leq H$.

Based on the above-described coordinate system, the horizontal equations of motion may be written:

$$\frac{du}{dt} - fv = -\frac{1}{\rho}\left[\frac{\partial p}{\partial x} + \rho g \frac{\partial E}{\partial x}\right] + \frac{\partial}{\partial z}\left[K_m \frac{\partial u}{\partial z}\right] \tag{3-1}$$

and

$$\frac{dv}{dt} + fu = -\frac{1}{\rho}\left[\frac{\partial p}{\partial y} + \rho g \frac{\partial E}{\partial y}\right] + \frac{\partial}{\partial z}\left[K_m \frac{\partial v}{\partial z}\right]. \tag{3-2}$$

Here, the following assumptions have been made: (1) all terms involving vertical velocity which are not part of the individual derivative are neglected and (2) all terms dealing with the variability of the map scale factor, $n(\varphi)$, or the convergence of meridians are neglected. The map scale factor is taken to equal unity, its value at the standard latitude for a polar stereographic projection.

b. Surface layer equations

A desirable aspect of the AFGWC-BLM is that it treats the PBL in terms of the mean flow, rather than requiring use of flux-form data. This circumvents difficulties in defining the Monin-Obukhov length, L in (2-7), when flux data are not available. With the assumption that eddy fluxes in the surface

layer are independent of height (noted in Chapter 2, Section a), we may write the following relationships (Gerrity, 1967):

$$K \frac{\partial s}{\partial z} = u_*^2 \tag{3-3}$$

and

$$K\left[\frac{\partial T}{\partial z} + \frac{g}{c_p}\right] = u_* \vartheta_*, \tag{3-4}$$

where $K$ is the eddy exchange coefficient, $s$ is the horizontal wind speed, and $\vartheta_*$ is a constant with units of $^{\circ}K$.

Recall (from Chapter 2, Section b) that two types of turbulence regimes exist: free and forced convection. When $R_i \leq -0.03$, free convection (buoyancy force) is assumed to dominate, and the eddy exchange coefficient is given by (Priestly, 1959)

$$K = \lambda z^2 \left[\frac{g}{\vartheta}\left|\frac{\partial T}{\partial z} + \frac{g}{c_p}\right|\right]^{1/2}. \tag{3-5}$$

When $R_i > -0.03$, however, forced convection (inertial force) is assumed to prevail and the eddy exchange coefficient is given by

$$K = [kz(1-\beta R_i)]^2 \frac{\partial s}{\partial z}. \tag{3-6}$$

Gerrity defines the dimensionless quantities $\lambda$ and $\beta$ to equal 1.2 and 2.0, respectively. (From this point on, $\beta$ no longer denotes the cross-isobaric angle.) Appropriate surface layer equations for both convection regimes are given below (see Appendix A for derivations):

Forced convection regime

Equations defining wind speed and $K_m$ at $z = h$ during forced convection conditions are, respectively:

$$S \equiv s(z=h) = \frac{u_*}{k} \ln\left(\frac{h}{z_o}\right) + \frac{\vartheta_*}{u_*} \frac{\beta g}{\bar{\vartheta}} (h - z_o) \tag{3-7}$$

and

$$K_m = khu_* \left[1.0 + \frac{\beta g}{\bar{\vartheta}} \frac{\vartheta_*}{u_*^2} kh\right]^{-1}. \tag{3-8}$$

Free convection regime

Equations for wind speed and $K_m$ at $z = h$ during free convection conditions are, respectively:

$$S \equiv s(z=h) = \frac{u_*}{k} \ln\left[\frac{z_o+1}{z_o}\right] - \frac{3.8\, u_*^2}{\lambda^{2/3} |u_* \vartheta_*|^{1/3}} \left[\frac{\bar{\vartheta}}{g}\right]^{1/3} \left[h^{-1/3} - (z_o+1)^{-1/3}\right] \tag{3-9}$$

and

$$K_m = \left[0.49\, \lambda^2 h^4 \left[\frac{g}{\bar{\vartheta}}\right] |u_* \vartheta_*|\right]^{1/3}. \tag{3-10}$$

Expressions for variables common to both the free and forced equations are:

$$\vartheta_* = -\frac{u_*^2 \bar{\vartheta}}{2\beta g} \frac{\ln(\frac{h}{z_i})}{k(h-z_i)} \left[1.0 - \left\{1.0 + \frac{4\beta g}{\bar{\vartheta} u_*^2} \left[\frac{T_h - T_i}{h - z_i} + \frac{g}{c_p}\right] \left[\frac{k(h-z_i)}{\ln(\frac{h}{z_i})}\right]^2\right\}^{1/2}\right]. \tag{3-11}$$

$$u_* = C(0.07625 - 0.00625 \log R_o), \tag{3-12}$$

$$R_o = \frac{C}{f z_o} \qquad \text{(Rossby Number)}, \tag{3-13}$$

where $C$ represents the magnitude of the surface geostrophic wind, and $T_h$ denotes the temperature at $z = h$ (obtained from

sounding data). $T_i$ is the temperature at $z = z_i$, the height of the instrument shelter; for the purposes of this study, $T_i = T_{sfc}$ and $z_i = 1$ m.

The angle of deviation, $\psi$, between the wind in the surface layer, S, and the surface geostrophic wind, G, is an empirical relationship given by Gerrity as

$$\psi = 0.825(\log R_o)^2 - 12.750(\log R_o) + 80.625, \tag{3-14}$$

where $\psi$, in degrees, varies between $15.6^o$ for $R_o = 10^{10}$ and $32.5^o$ for $R_o = 10^6$. Expressions for the components of $S$, viz., $U$ and $V$, may be obtained from relationships among $S$, $\psi$ and $C$ $(=[C_x^2 + C_y^2]^{1/2})$:

$$U = (C_x K_1 - C_y K_2)\,(C_x^2 + C_y^2)^{-1} \tag{3-15}$$

and

$$V = (C_y K_1 + C_x K_2)\,(C_x^2 + C_y^2)^{-1}, \tag{3-16}$$

where

$$K_1 = S\,(C_x^2 + C_y^2)^{1/2} \cos\psi \tag{3-17}$$

and

$$K_2 = S\,(C_x^2 + C_y^2)^{1/2} \sin\psi. \tag{3-18}$$

c. Computational scheme for the surface layer

A determination of the appropriate stability regime within the surface layer must be made at each computational point; the choices for the model are (1) strongly stable, (2) forced convection, and (3) free convection. As noted previously, $R_i$ is often used to indicate the extent of turbulence present.

However, the classical definition for $R_i$ (2-11) cannot be used in this research because the vertical wind shear ($\frac{\partial s}{\partial z}$ in 2-11 and 3-6) is not immediately discernible from the thermal data. Gerrity has derived an alternate expression for $R_i$ in terms of variables already presented, viz.,

$$R_i = \frac{1}{\beta}\left\{1.0 - \left[1.0 + \frac{\beta g}{\bar{\vartheta}} \frac{\vartheta_*}{u_*^2} kh\right]^{-1}\right\}. \tag{3-19}$$

Using this equation, determination of the appropriate convection regime is made as follows.

The first decision to be made is whether conditions are strongly stable or forced. The limiting factor for forced convection on the "stable side" is that $K_m$ must be a positive term. Recalling (3-8), $\vartheta_*$ is the only variable which may be negative. Therefore, $K_m$ can become negative when

$$[1.0 + \frac{\beta g}{\bar{\vartheta}} \frac{\vartheta_*}{u_*^2} kh]^{-1} < 0. \tag{3-20}$$

Substituting zero for this term in (3-19) yields

$$R_i = \frac{1}{\beta} = \frac{1}{2.0} = 0.5.$$

Thus, when $R_i > 0.5$ the surface layer may be considered strongly stable, and the equations for $S$ and $K_m$ are

$$S = 0.176\, G \tag{3-21}$$

and

$$K_m = 1.0 \text{ m}^2 \text{ s}^{-1}. \tag{3-22}$$

The fraction 0.176 was estimated by Gerrity from the classic Ekman spiral in which $K = 1.0$ m$^2$ s$^{-1}$, $f = 10^{-4}$ s$^{-1}$ and the wind

is assumed to vanish at $z = 0$. Equation (3-22) is the classical minimum value of $K_m$.

The determination of whether the surface layer is in a free or forced convection regime must consider the internal constraint in the expression for $\vartheta_*$ (3-11). The value for $\vartheta_*$ will be complex if:

$$1.0 + \frac{4\beta g}{\bar{\vartheta} u_*^2}\left[\frac{T_h - T_i}{h - z_i} + \frac{g}{c_p}\right]\left[\frac{k(h-z_i)}{\ln(\frac{h}{z_i})}\right]^2 < 0. \qquad (3\text{-}23)$$

Such a situation will occur when the "surface" temperature, $T_i$, is several degrees warmer than the temperature at $z = 50$ m, $T_h$ --- an unquestionably free convection condition. In other words, the equation for $\vartheta_*$ may be considered valid for forced convection conditions as long as (after manipulation of (3-23)):

$$\left[\frac{T_h - T_i}{h - z_i} + \frac{g}{c_p}\right] \geq -\frac{u_*^2 \bar{\vartheta}}{4\beta g}\left[\frac{\ln(\frac{h}{z_i})}{k(h-z_i)}\right]^2. \qquad (3\text{-}24)$$

Further, as noted previously, turbulence is assumed to be of the forced convection type when

$$-0.03 < R_i \leq 0.5. \qquad (3\text{-}25)$$

Thus, for this study, the tests for determining the appropriate turbulence regime in the surface layer are:

1) For $R_i > 0.5$, <u>strongly stable</u> conditions are assumed, and (3-21) and (3-22) are used to compute $S$ and $K_m$.

2) If (3-24) <u>and</u> (3-25) are satisfied, <u>forced con-</u>

vection conditions are assumed to exist, and (3-7) and (3-8) are used to compute $S$ and $K_m$. If the resultant value for $K_m$ is found to be negative, both parameters are recomputed using the free convection equations.

3) When $R_i \leq -0.03$, free convection conditions are assumed, and (3-9) and (3-10) are used to compute $S$ and $K_m$.

This computational scheme differs in several respects to that outlined by Gerrity, most notably in the equalization in (3-24).

d. Transition layer equations

Recall assumptions (1) and (2) presented in Section a. As noted by Gerrity, (3-1) and (3-2) may be further simplified for the transition layer by assuming: (3) the individual derivatives may be neglected (see Appendix D), (4) $K_m$ is independent of height, and (5) the geostrophic wind components, defined as

$$u_g = -\frac{1}{\rho f}\left[\frac{\partial p}{\partial y} + \rho g \frac{\partial E}{\partial y}\right] \tag{3-26}$$

and

$$v_g = \frac{1}{\rho f}\left[\frac{\partial p}{\partial x} + \rho g \frac{\partial E}{\partial x}\right], \tag{3-27}$$

are the following linear functions of height:

$$u_g = u_g^H + b(H-z) \tag{3-28}$$

and

$$v_g = v_g^H + c(H-z). \tag{3-29}$$

Substituting (3-26) and (3-27) into (3-1) and (3-2), respectively, the horizontal equations of motion may be written (recall $m = \left[\frac{f}{2K_m}\right]^{1/2}$),

$$\frac{\partial^2 u}{\partial z^2} = -2m^2(v - v_g) \tag{3-30}$$

and

$$\frac{\partial^2 v}{\partial z^2} = 2m^2(u - u_g). \tag{3-31}$$

Choosing boundary conditions such that

$$\left.\begin{aligned} u &\to u_g \\ v &\to v_g \end{aligned}\right\} \text{ as } z \to \infty \quad (\equiv H \text{ for the PBL})$$

and

$$\left.\begin{aligned} u &\to U \\ v &\to V \end{aligned}\right\} \text{ as } z \to h,$$

the solutions to (3-30) and (3-31) yield the <u>modified Ekman equations</u>:

$$u = u_g + e^{-m(z-h)}\{(U - u_g^h)\cos[m(z-h)] + (V - v_g^h)\sin[m(z-h)]\} \tag{3-32}$$

and

$$v = v_g + e^{-m(z-h)}\{(V - v_g^h)\cos[m(z-h)] - (U - u_g^h)\sin[m(z-h)]\}. \tag{3-33}$$

Constants $b$ and $c$ in (3-28) and (3-29) are obtained through manipulation of the Hypsometric Equation and Equation of State; the resulting expressions for $u_g$ and $v_g$, are:

$$u_g = u_g^H + \frac{H-z}{H-h}\left\{(u_g^H - \tilde{u})\left[\frac{T_h - T_H}{T_H}\right] - T_h \frac{g}{f}(H-h)\frac{\partial}{\partial y}\left[\frac{1}{\overline{T^*}}\right]\right\} \tag{3-34}$$

and

$$v_g = v_g^H + \frac{H-z}{H-h}\left\{(v_g^H - \tilde{v})\left[\frac{T_h - T_H}{T_H}\right] + T_h \frac{g}{f}(H-h)\frac{\partial}{\partial x}\left[\frac{1}{\overline{T^*}}\right]\right\}. \tag{3-35}$$

where

$$\tilde{u} = -\frac{g}{f}\frac{\partial E}{\partial y}. \tag{3-36}$$

and

$$\tilde{v} = \frac{g}{f}\frac{\partial E}{\partial x}. \tag{3-37}$$

The geostrophic wind components at the top of the transition layer, $u_g^H$ and $v_g^H$, are computed using (3-26) and (3-27). Values for $u_g^h$ and $v_g^h$ are obtained using (3-34) and (3-35) for $z = h$. $T_h$ and $T_H$ are temperatures at $z = h$ and $z = H$, respectively, while $\frac{1}{\overline{T^*}}$ is evaluated over the entire layer, $h \leq z \leq H$. These modified geostrophic wind equations, (3-34) and (3-35), are a variation of expressions for the thermal wind (see, for example, Arya and Wyngaard, 1975), and serve as input to the modified Ekman equations (3-32) and (3-33).

e. Computational scheme for the transition layer

Since the surface layer is taken to be the lowest 50 m of the PBL, wind flow within that narrow region has not been calculated in this study. However, data at its boundaries (surface and 50 m) are used to compute the wind components and the eddy viscosity coefficients at the upper boundary (lowest level of the Ekman layer). The surface parameters are then input into the modified Ekman equations to obtain horizontal wind fields at 50, 150, 300, 600, 900, 1200, and 1600 m above ground level (AGL). The fixed geometrical thickness between levels

insures that a detailed description of the boundary layer winds can be obtained over variable terrain (Fig. 2).

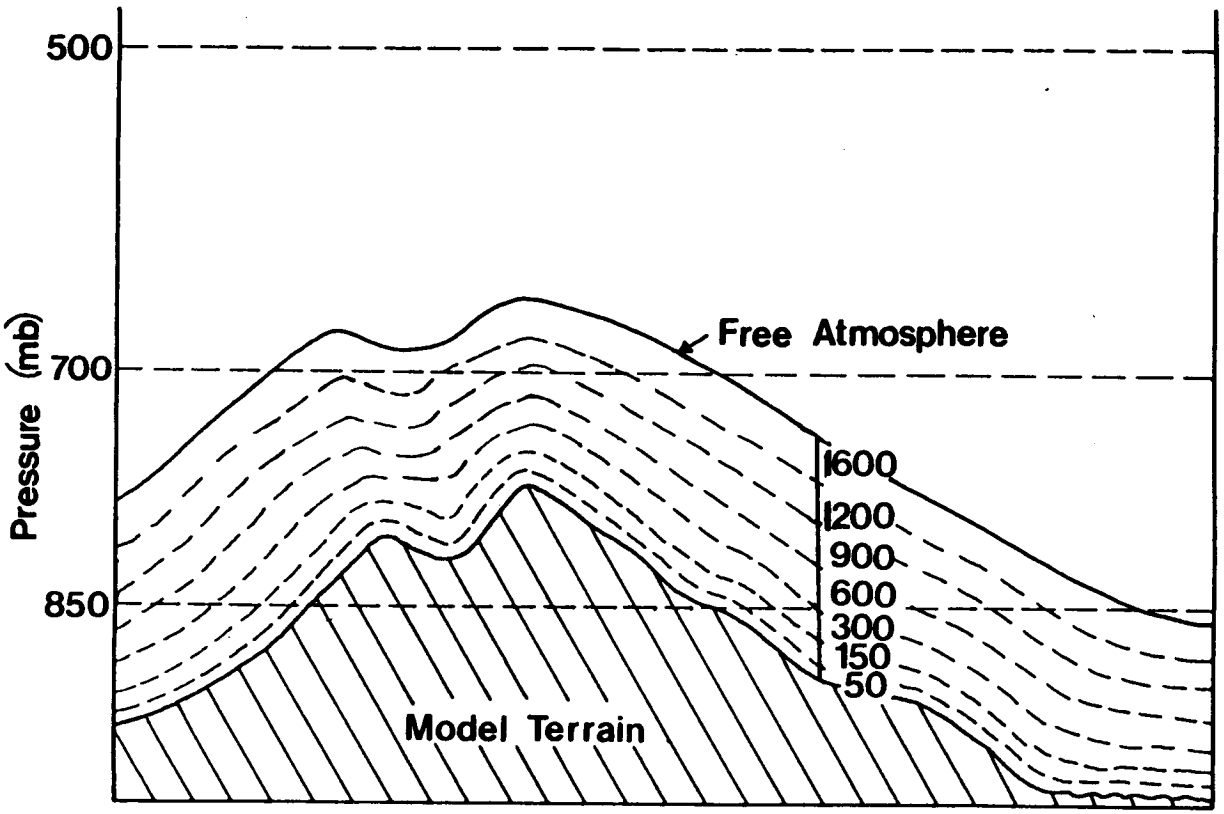


Fig. 2. Vertical depiction of the AFGWC Boundary Layer Model (after Hadeen, 1970).

## 4. DATA

### a. Satellite data

TIROS-N sounding data, processed by the National Environmental Satellite Service (University of Wisconsin), were made available through the auspices of NASA's Marshall Space Flight Center, Huntsville, AL. The data retrieval and processing techniques are described in Smith et al. (1978). The sixty-two satellite soundings (Fig. 3), obtained at 0921 GMT 19 April 1979, included temperature, dewpoint, and geopotential height data at the surface and at ten pressure levels (1000, 850, 700, 500, 400, 300, 250, 200, 150, and 100 mb). Smith et al. (1981) have shown that TIROS-N soundings have a nominal global horizontal resolution and spacing of 250 km, with a higher horizontal resolution of 50 km being possible for limited areas when man-machine interactive processing methods (e.g., McIDAS) are employed. The soundings used in this study have an average spacing of approximately 150 km.

Several studies have evaluated the representativeness of TIROS-N temperature data through direct comparisons with corresponding RAOB soundings (Phillips et al., 1979; Smith et al., 1979; Schlatter, 1980 and 1981; Scoggins et al., 1981). Schlatter (1980 and 1981) found that the average TIROS-N sounding was too warm near the surface, too cool in the middle tro-

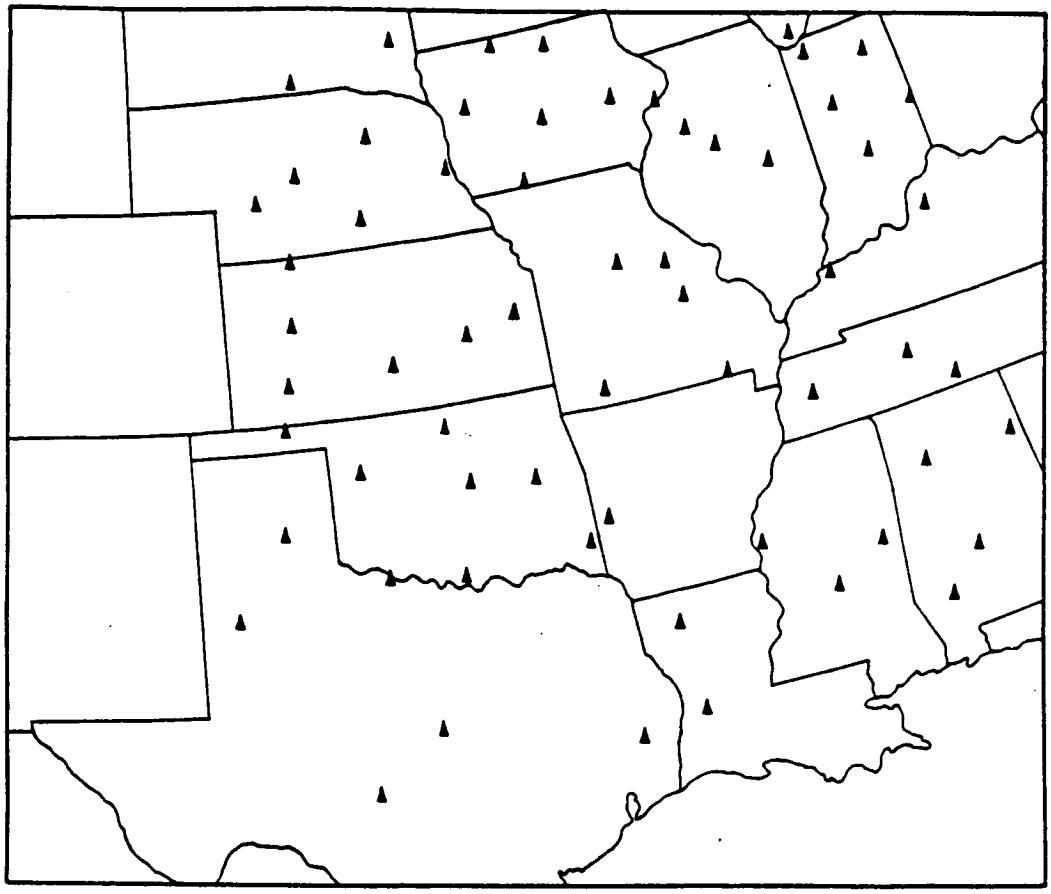

Fig. 3. TIROS-N sounding sites at 0921 GMT 19 April 1979.

posphere, and too warm at the tropopause. Root-mean-square (RMS) differences were < 2°C in the 1000-850 mb layer. The study also indicated that horizontal temperature gradients inferred from TIROS-N soundings were consistently weaker than analyzed gradients. A comprehensive study by Scoggins et al. (1981) compared TIROS-N data with radiosonde soundings during AVE-SESAME I (10-11 April 1979). Results showed a mean difference of -0.5°C over the entire sounding, indicating that the TIROS-N-derived temperatures contained a negative bias relative to radiosonde-derived temperatures. Further, a mean RMS difference of 1.8°C was found.

Cloud contamination is a factor in producing discrepancies between satellite and radiosonde data. Schlatter (1981) noted that discrepancies are enhanced in cloudy regions, such that cloudy retrievals are more than 1°C too warm in the 1000-850 mb layer. In the lower troposphere, RMS differences for partly cloudy soundings are larger than those for clear soundings. Hillger and Vonder Haar (1977), Phillips et al. (1979) and Smith et al. (1979) also have documented the effect of clouds on satellite temperature retrievals.

The above-mentioned studies provide general guidelines about the nature of the input satellite data. However, comparison statistics are not a true measure of the satellite's accuracy (Yates, 1974; Bruce et al., 1977; Phillips et al.,

1979; Smith et al., 1979). As noted earlier, discrepancies between the two sensors are due in part to the fact that a radiosonde gives a point measurement while the satellite-inferred value represents average conditions over a volume which is several tens of kilometers wide and several kilometers in depth. Also, there is usually a time difference between a given satellite pass and corresponding radiosonde soundings. Hillger and Vonder Haar (1979) more clearly defined the accuracy of satellite thermal data by performing structure function analyses of satellite soundings alone. This procedure eliminates those components of the discrepancies attributable to sensors not being co-located in space and time. Their study found a noise level of 0.5°C for temperatures at 700, 500, and 300 mb, a value much smaller than the 1-3°C error usually associated with direct satellite-radiosonde comparisons.

b. Radiosonde data

Rawinsonde data from AVE-SESAME II, viz., 1200 GMT 19 April 1979, consisted of standard upper-air measurements from twenty-three National Weather Service (NWS) stations and sixteen special sites (Fig. 4). Although denoted as 1200 GMT soundings, most releases actually were made at approximately 1115 GMT. The NWS stations alone yield synoptic-scale resolution through an average station spacing of 400 km, while the combination of NWS and special site stations results in

subsynoptic-scale resolution with an average station spacing of 250 km. These data, also provided by the Marshall Space Flight Center, were available in two formats: (1) soundings with data at 25 mb intervals and (2) baroswitch contact data (from which the 25 mb soundings were interpolated) at intervals of approximately 10 mb (100 m). Reduction procedures used to process the rawinsonde data are described by Fuelberg (1974). Further details about the AVE-SESAME '79 experiments are given by Alberty et al. (1979) and Hill et al. (1979). Particulars concerning the AVE-SESAME II period are provided by Williams et al. (1980a,b).

c. Synoptic situation

At 1200 GMT 19 April 1979 a cold front anchored in West Texas extended through low pressure in eastern Colorado, and northward across western Nebraska and South Dakota (Fig. 5). A weak warm front stretched from South Dakota southeastward to Georgia. A few areas of weak-to-moderate convection were scattered over southern Texas and along the Mississippi River Valley. Low-level subsidence and radiation inversions were prevalent at the various reporting sites (Fig. 6). As the day progressed, a low-level tongue of warm, moist air flowed northward from the Gulf of Mexico, and the northern end of the front began to swing across Nebraska into eastern Iowa. By 1800 GMT major thunderstorm activity began developing over much of

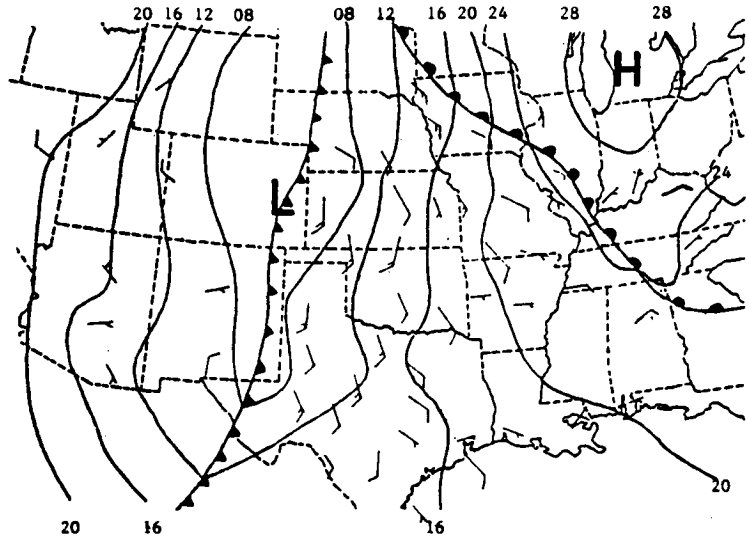


Surface

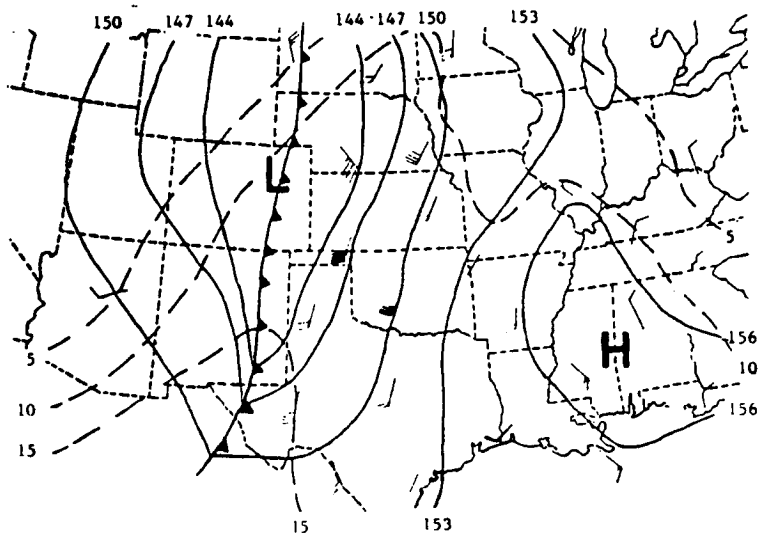


850 mb

Fig. 5. Synoptic conditions at the surface and 850 mb at 1200 GMT 19 April 1979 (after Williams et al., 1980b).

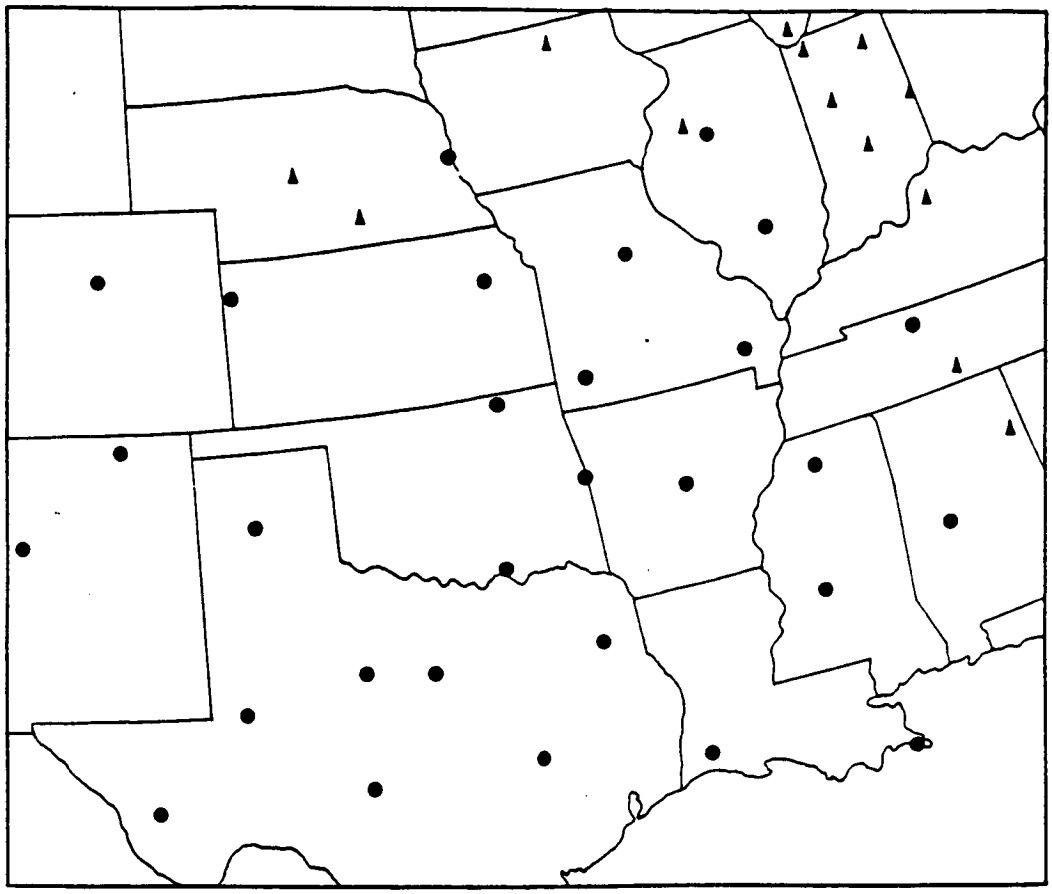

Fig. 6. Sounding sites exhibiting low-level inversions. RAOB sites are denoted by circles, satellite soundings by triangles.

Texas, northwestern Missouri and central Iowa, and by 2100 GMT a line of intense activity had formed through central Nebraska, central Kansas and western Oklahoma. A detailed synoptic discussion of the entire AVE-SESAME II period (1200 GMT 19 April-1200 GMT 20 April) is presented by Williams et al. (1980b).

## 5. METHODOLOGY

The main thrust of this study is to obtain wind profiles in the PBL using satellite thermal data. The mechanics of the research are outlined below, while remarks on statistical and qualitative comparisons performed at the various steps are presented in Chapter 6.

### a. Generation of input data

Soundings from the 62 TIROS-N and 39 rawinsonde (25 mb-interval) observations were plotted manually on Skew T, Log p diagrams. Temperature, dewpoint and pressure values for each site were linearly interpolated to the seven "above ground" model levels from the plotted soundings. As a check on the interpolation procedure, constant height maps of the three parameters were plotted and analyzed to insure continuity of the fields.

### b. Objective analyses of the input data

#### 1) Grid structure

The Barnes (1973) objective analysis scheme was used to obtain gridded fields of the various input parameters. A 17x20 base grid, with a mesh of 127 km, encompassed all TIROS-N and RAOB sounding sites (see Fig. 7). The grid was oriented to a

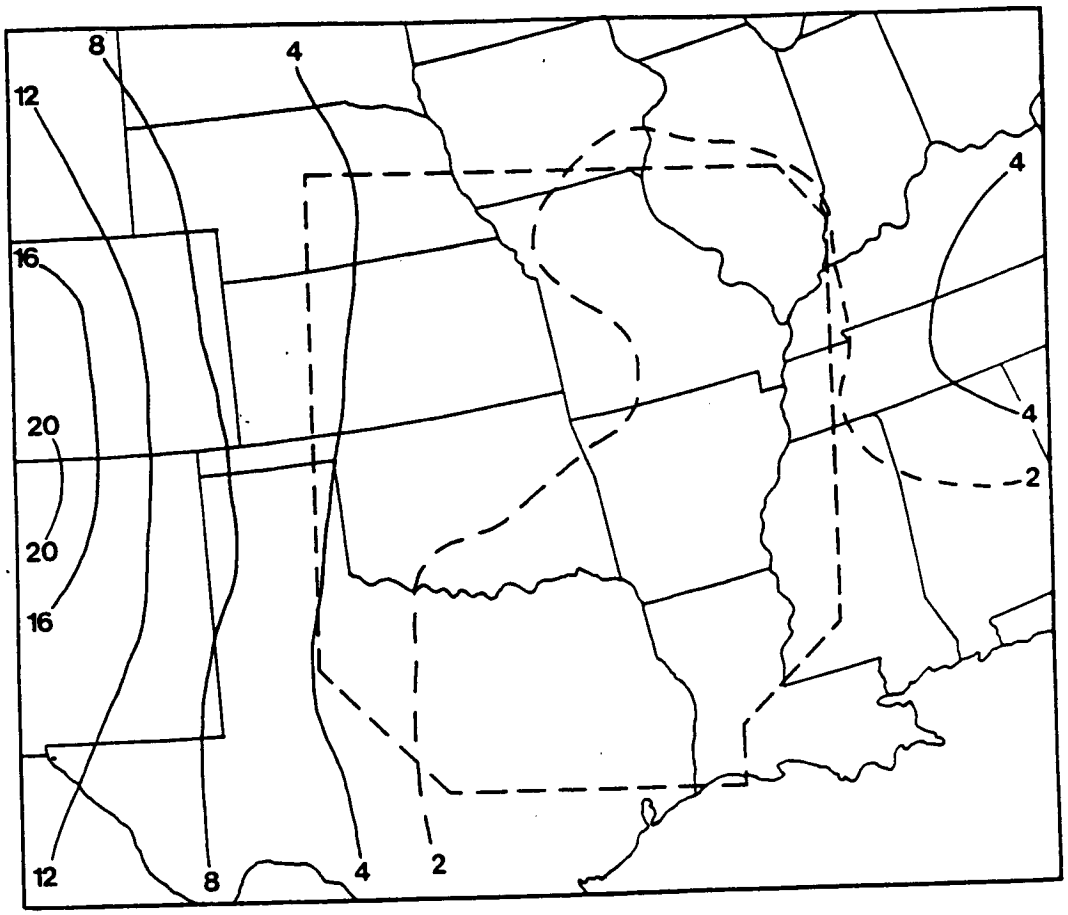


Fig. 7. Outlines denoting the 17 x 20 grid area in which objective analyses of input data were performed (solid line) and the inner region (dashed line) used in qualitative and statistical comparisons. Terrain elevations are given in hundreds of meters.

1:10,000,000 polar stereographic map projection such that the upper left corner of the grid was anchored at 45°N 107°W, with the lefthand side parallel to the 107°W meridian (see Saucier, 1955). A subset of the total region, comprising the common areas of satellite and rawinsonde soundings (also seen in Fig. 7), was used to evaluate the computed winds and kinematic parameters which are discussed in Chapter 6. This smaller area contains 111 gridpoints; a larger statistical data base would be desirable, however 111 is the maximum number of "common" points feasible using the given data. Thus, statistics discussed in this study should be considered for comparison (inspection) purposes only, and not as definitive statements for all TIROS-N data.

2) Temperature and dewpoint

Separate 17x20 gridded fields of satellite and RAOB temperatures and dewpoints were generated for each model level.

3) Pressure

Pressure fields at the eight levels were obtained by first reducing the given station pressures to mean sea level (MSL) using the standard pressure-height relation:

$$p_{msl} = p_{sta} + 0.1065(z_{sta}). \qquad (5\text{-}1)$$

Here, pressures at MSL, $p_{msl}$, and the station elevation, $p_{sta}$,

are in mb, while the station heights, $z_{sta}$, are in meters. The Barnes scheme was then applied to yield separate 17x20 grids of $p_{msl}$ for both the RAOB and satellite data. Using terrain elevations provided by AFGWC (shown in Fig. 7), "station pressures" for each gridpoint were computed by reversing the pressure-height relation such that:

$$p_{sfc} = p_{msl} - 0.1065(z_{gp}). \tag{5-2}$$

where $p_{sfc}$ denotes the surface pressure at a given gridpoint and $z_{gp}$ is the terrain elevation in meters at that gridpoint. Pressures for the seven "above ground" levels at each gridpoint were then computed using the Hypsometric Equation:

$$p_2 = p_1 \exp\left[-\left[\frac{\Psi_2-\Psi_1}{29.27}\right]\left[\frac{1}{\overline{T^*} + 273}\right]\right]. \tag{5-3}$$

where $p_1$ and $\Psi_1$ are pressure (mb) and height (m), respectively, at the lower boundary of the model layer under consideration, and $p_2$ and $\Psi_2$ correspond to the upper boundary. The mean virtual temperature, $\overline{T^*}$ was obtained as an average of $T^*$ at the upper and lower limits of the given layer. Virtual temperature, $T^*$, was computed using the approximate relation

$$T^* \approx T + \frac{w}{6}. \tag{5-4}$$

where $T^*$ and the temperature, $T$, at the level in question are in $^{o}C$; the mixing ratio, $w$, is given in g $kg^{-1}$ and is defined by

$$w = 0.622\left[\frac{e}{p}\right](10^3). \tag{5-5}$$

The vapor pressure, $e$ (in mb), was obtained by inserting the appropriate dewpoint temperature, $T_D$, into Lowe's polynomial

algorithm (Lowe, 1977):

$$e = a_0 + T_D(a_1 + T_D(a_2 + T_D(a_3 + T_D(a_4 + T_D(a_5 + a_6 T_D))))), \qquad (5\text{-}6)$$

where, for $T_D$ in $^{o}$C,

$$a_0 = 6.107799961,$$

$$a_1 = 4.436518521\times10^{-1},$$

$$a_2 = 1.428945805\times10^{-2},$$

$$a_3 = 2.650648471\times10^{-4},$$

$$a_4 = 3.031240396\times10^{-6},$$

$$a_5 = 2.034080948\times10^{-8}, \text{ and}$$

$$a_6 = 6.136820929\times10^{-11}.$$

c. Computation of modified Ekman winds

Equations (3-34) and (3-35) were solved at each gridpoint for all above-ground model levels, using temperatures at the top ($H$) and bottom ($h$) of the PBL generated in Section b-2. Equations (3-32) and (3-33) were then solved (also at each gridpoint). Surface geostrophic wind components, $G_x$ and $G_y$, were calculated at a given point using (3-26) and (3-27), where we let $u_g \equiv G_x$ and $v_g \equiv G_y$.

d. Computation of standard geostrophic winds

Equations (3-26) and (3-27) were also solved at each model level to provide standard geostrophic winds. These fields served as a basis for comparisons outlined in Chapter 6.

e. Validation of technique

In the operational AFGWC-BLM, several variables used in computing the modified Ekman winds are obtained from various prediction algorithms. In the current study, however, all variables are obtained solely from observed data. This fundamental difference in procedure requires a careful validation of the computational approach.

A two-step verification procedure was employed. Twenty-six of the rawinsonde sites provided contact ("actual") winds at ∿100 m intervals within the PBL (Fig. 4). Values were linearly interpolated to the model levels and then objectively analyzed as noted earlier to smooth out the mesoscale features. If the RAOB-derived PBL winds (computed by inserting AVE-SESAME '79 data into the BLM equations) compared favorably with these "actual" wind fields, the computational approach was judged to be suitable. The second step involved the satellite data. RAOB-derived modified Ekman winds were used as a basis of comparison with their satellite-derived counterparts. A favorable agreement established the utility of using the satellite data in the BLM scheme.

f. Response determination

It would be desirable to take advantage of the relatively small horizontal spacing of the satellite (and RAOB) data to

determine not only whether satellite thermal data would yield reasonable PBL winds, but also whether such winds would be representative of the mesoscale. Two factors, however, do not permit this investigation to strive for such a fine resolution. First, the technique chosen (modified Ekman approach) is based on geostrophic theory and therefore cannot produce mesoscale PBL winds which, in reality, are often ageostrophic. Second, it would be desirable to compare satellite-derived PBL winds to actual winds as well as to the RAOB-derived wind data. Since the "actual" wind data are from twenty-six RAOB sites with an average spacing slightly less than 400 km (Fig. 4), mesoscale evaluations would not be possible.

The Barnes (1973) procedure allows one to select percentages of originally resolved amplitudes, as functions of wavelength, that are retained by the analysis. This selection can be described by means of response curves or resolution profiles. Ten different choices were investigated for use in the current study (Fig. 8). An ∿50% response was obtained for amplitudes having wavelengths from 300 to 2000 km (right curve). The goal was to select a response that would reduce "noise" generated by the random data errors as well as small scale features that could not be consistently resolved by the data sets, while simultaneously yielding synoptic-scale resolution.

To determine the response most compatible with the various

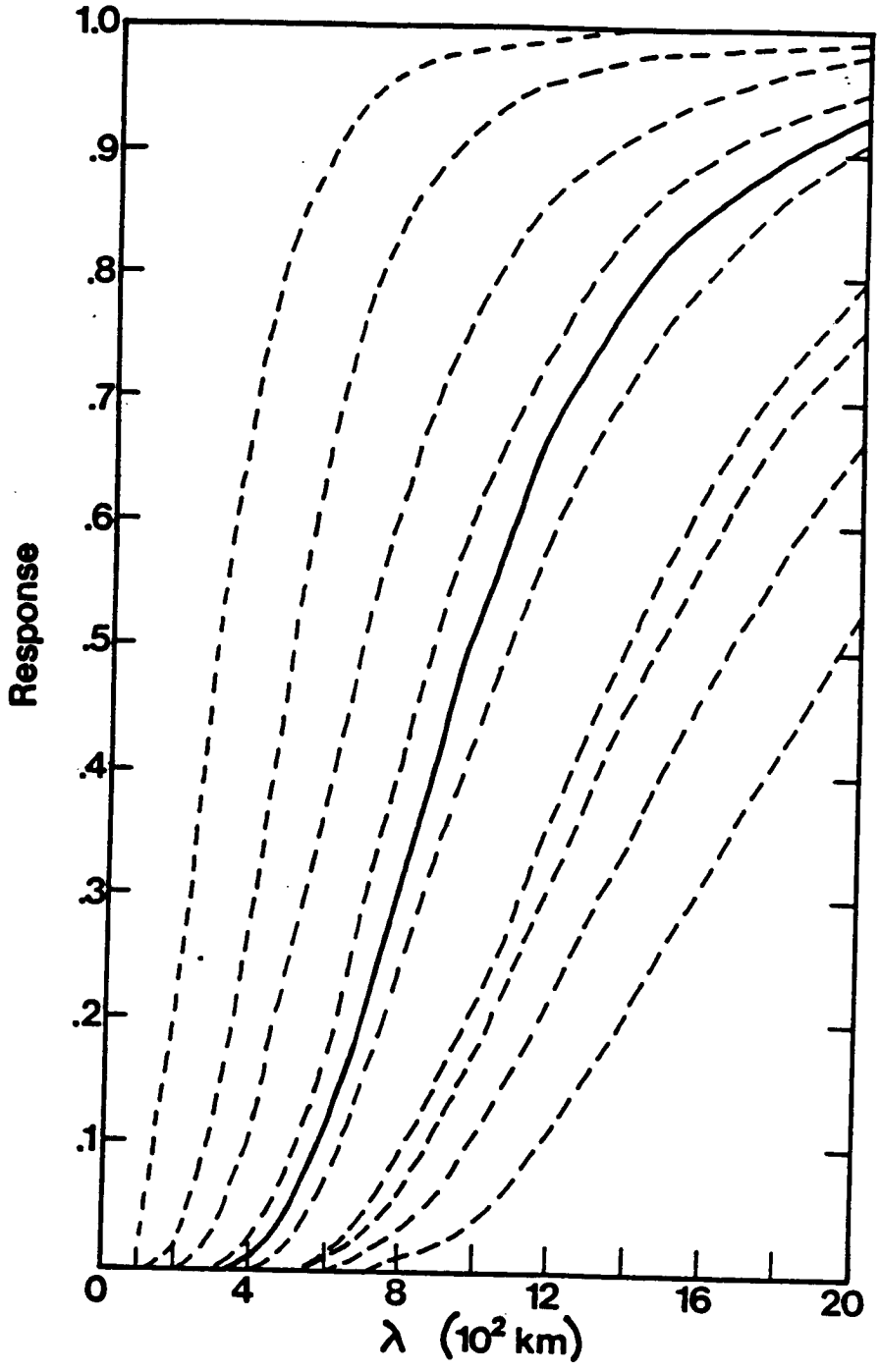


Fig. 8. Resolution profiles tested, with the solid line denoting an ∿50% response at wavelengths of 1000 km.

data sets, the procedure described in Sections b-2 through e were repeated for the ten options. Based on statistical evaluations between the thermally-derived winds and their observed counterparts (see Appendix B), the most appropriate response appeared to be ∿50% at a wavelength of 1000 km (solid curve in Fig. 8). All results that follow are based on input data and observed winds objectively analyzed at this resolution. This response isolates larger-scale features of the flow which should be quasi-geostrophic in nature, except for the effects of friction, and which should be verifiable with the available data. It has the added advantage of removing input data errors that would appear as short wave phenomenon.

## g. Computation of kinematic parameters

Gridded fields of horizontal moisture divergence, $MD_2$, (where negative divergence implies moisture convergence) were computed using the standard expression:

$$MD_2 = \vec{\nabla}_2 \cdot (w\vec{V}_2), \tag{5-7}$$

where, again, $w$ is the mixing ratio (g kg$^{-1}$) and $\vec{V}$ denotes the velocity vector. Expansion of (5-7) yields

$$\left.\begin{aligned} \vec{\nabla}_2 \cdot (w\vec{V}_2) &= \frac{\partial}{\partial x}(wu) + \frac{\partial}{\partial y}(wv) \\ &= w\left[\frac{\partial u}{\partial x} + \frac{\partial v}{\partial y}\right] + u\,\frac{\partial w}{\partial x} + v\,\frac{\partial w}{\partial y} \\ &= w(\vec{\nabla}_2 \cdot \vec{V}_2) + \vec{V}_2 \cdot (\vec{\nabla}_2 w) \\ MD_2 &= (\text{divergence term})_2 + (\text{advective term})_2 . \end{aligned}\right\} \tag{5-8}$$

As noted by Negri and Vonder Haar (1980), horizontal moisture

convergence (negative $MD_2$) can occur when significant horizontal convergence $[\omega(\vec{\nabla}_2 \cdot \vec{V}_2) < 0]$ and/or advection of moist air $[\vec{V}_2 \cdot \vec{\nabla}_2 \omega < 0]$ are present. Moisture convergence fields for the seven above-ground model levels were computed in three ways: First, a "control" data set was obtained by solving (5-8) using RAOB-derived modified Ekman wind components and values for mixing ratios derived from RAOB dewpoint temperatures. A second set of moisture convergence fields was computed using corresponding satellite-derived modified Ekman and mixing ratio data. As a test of the "usability" of TIROS-N moisture data, a third set of horizontal moisture convergence fields was obtained for comparison by combining satellite-derived modified Ekman wind components with RAOB-derived mixing ratios.

To more fully examine the nature of the resultant moisture convergence values, fields of horizontal velocity divergence and moisture advection were analyzed using both the RAOB and satellite data sets. Values of horizontal divergence ($DIV_2$) were calculated using the standard definition,

$$DIV_2 = \vec{\nabla}_2 \cdot \vec{V}_2. \tag{5-9}$$

while moisture advection was obtained through the last term of (5-8).

Computation of relative vorticity $[\vec{k} \cdot (\vec{\nabla}_2 \times \vec{V}_2)]$ and vertical motion ($VM$) were additional tests of the "accuracy" of the satellite-derived winds. While each of the four previous

kinematic parameters were calculated at individual model levels, vertical velocities were generated at 1600 m AGL using stepwise integration through the PBL. Assuming zero vertical motion at the surface and constant density, the Continuity Equation yields:

$$VM_{1600} = \sum_{i=2}^{8} [-\overline{DIV}_2 (z_i - z_{i-1})] \qquad (5\text{-}10)$$

where summation is over the eight model levels and $\overline{DIV}_2$ denotes the mean horizontal velocity divergence in a given layer. $DIV_2$ at 50 m AGL was assumed to be representative of the divergence in the surface layer. Since, as noted by O'Brien (1970), essentially no correction to kinematic vertical velocities is required in the lower atmosphere, current values were not adjusted.

## 6. RESULTS

Results from the procedure outlined in Chapter 5 are given in the following manner:

First, gridded fields of temperature, dewpoint and pressure are presented to compare the input RAOB and TIROS-N data. Next, RAOB-derived geostrophic and modified Ekman winds are evaluated with "actual" wind fields to determine the validity of the computational technique. The goal is to show that the modified Ekman approach is not only feasible, but that it yields better results than those from the much simpler standard geostrophic wind equations.

With the RAOB-derived Ekman winds established as a basis for comparison, the satellite-derived Ekman winds are then examined. A great similarity between the two Ekman wind sets will demonstrate the usefulness of satellite-derived thermal data in computing synoptic-scale PBL winds. A sensitivity analysis then examines the effects of three variables on the computed winds, viz., the depth of the surface layer, the character of $K_m$ and the computational scheme's handling of random error in the input satellite thermal data. Finally, fields of kinematic parameters derived using satellite data are compared to their RAOB-derived counterparts.

### a. Comparison of input data

Objectively analyzed fields of input temperature based on RAOB and satellite data are shown in Figs. 9 and 10, respectively. From the surface to 600 m AGL, both versions exhibit thermal ridges extending from central Texas into Kansas, and from Louisiana northward along the Arkansas-Mississippi border. Coldest temperatures are located in the northeastern quadrant of the area, over southern Illinois. Based on the satellite data, the warm tongue located over the southern Mississippi River Valley (above 600 m AGL) extends northwestward into Kansas and Nebraska. With the RAOB data, however, the warm region over the Midwest extends from western Texas. Furthermore, the cold area in the northeast attains more of a trough-like pattern that stretches into eastern Texas.

The satellite temperatures, shown in Table 1, tend to be $\sim 2^{\circ}C$ cooler than their RAOB counterparts. This is observed for both the horizontal mean and maximum values. Greatest average differences of 3.2 and $3.3^{\circ}C$ occur at 600 and 900 m AGL, respectively. Standard deviations for the satellite data are only slightly smaller than those for the RAOB data. Thus, the two sources indicate similar horizontal variability even though their mean values are slightly different. A portion of the differences is assumed to be due to the TIROS-N soundings being taken approximately 2 h earlier than the rawinsonde soundings. Nonetheless, the statistical comparisons are in good agreement with those from previous evaluations (e.g., Arnold *et al.*,

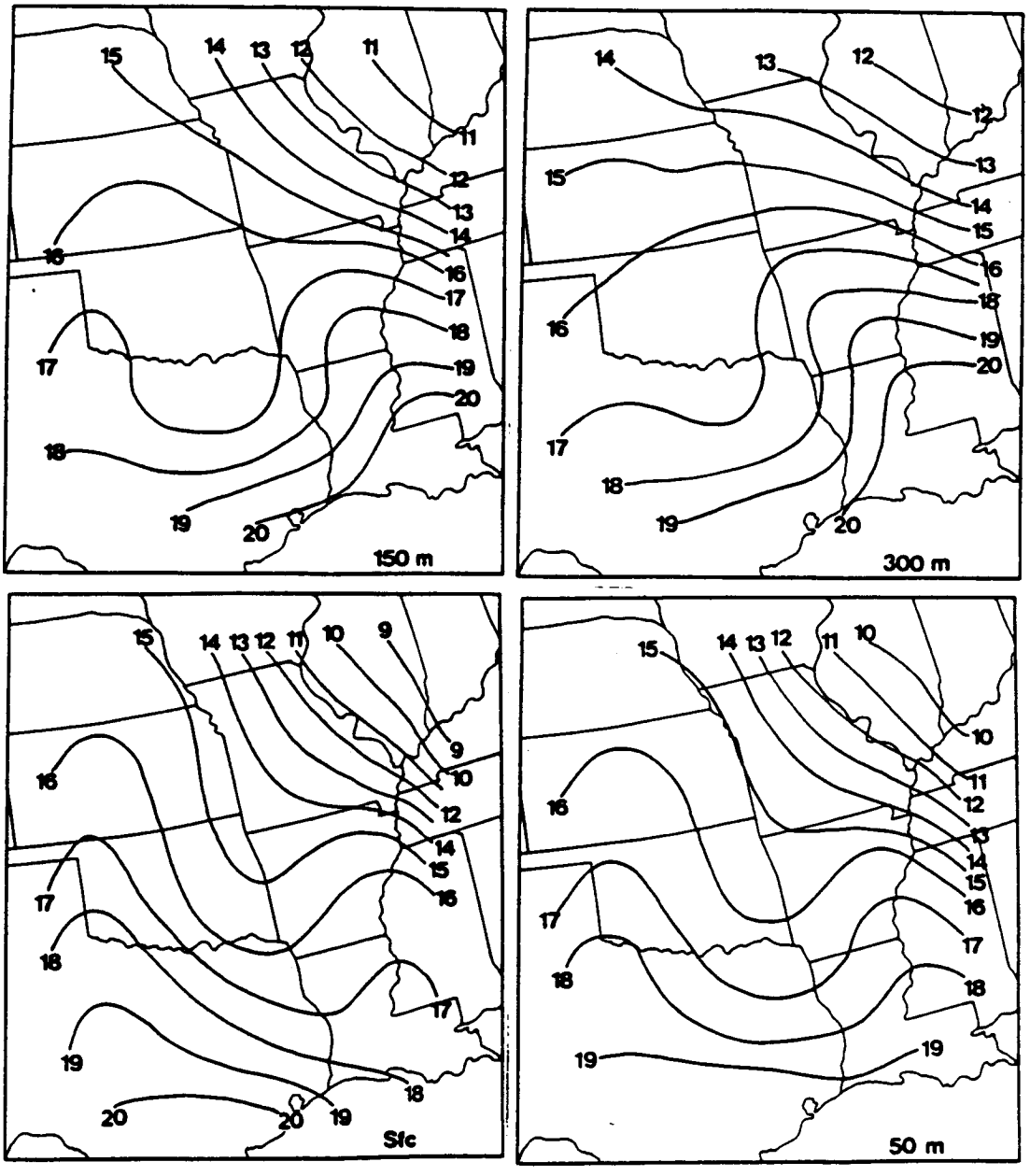


Fig. 9. Objectively analyzed fields of input RAOB temperatures (°C).

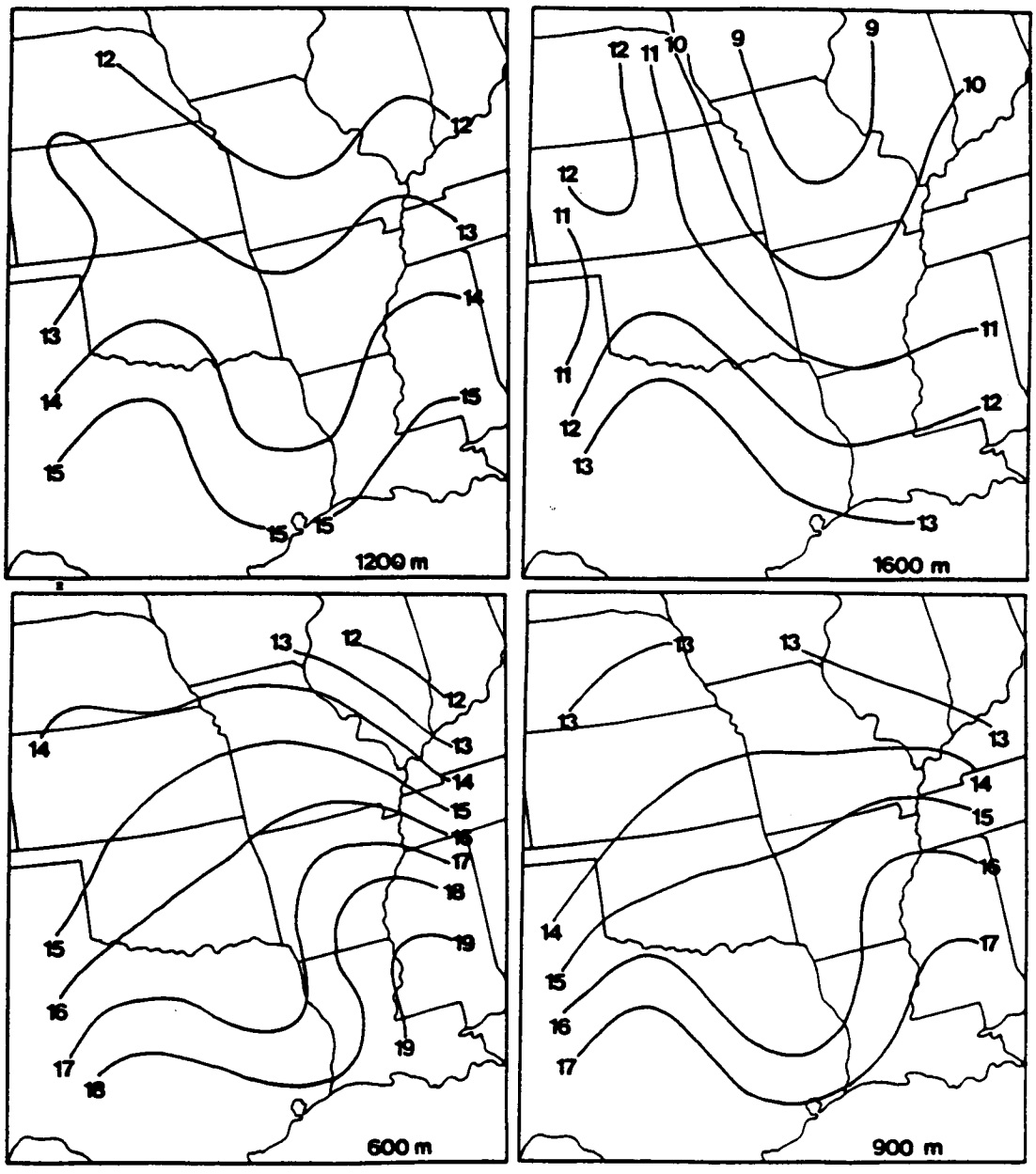


Fig. 9. Continued.

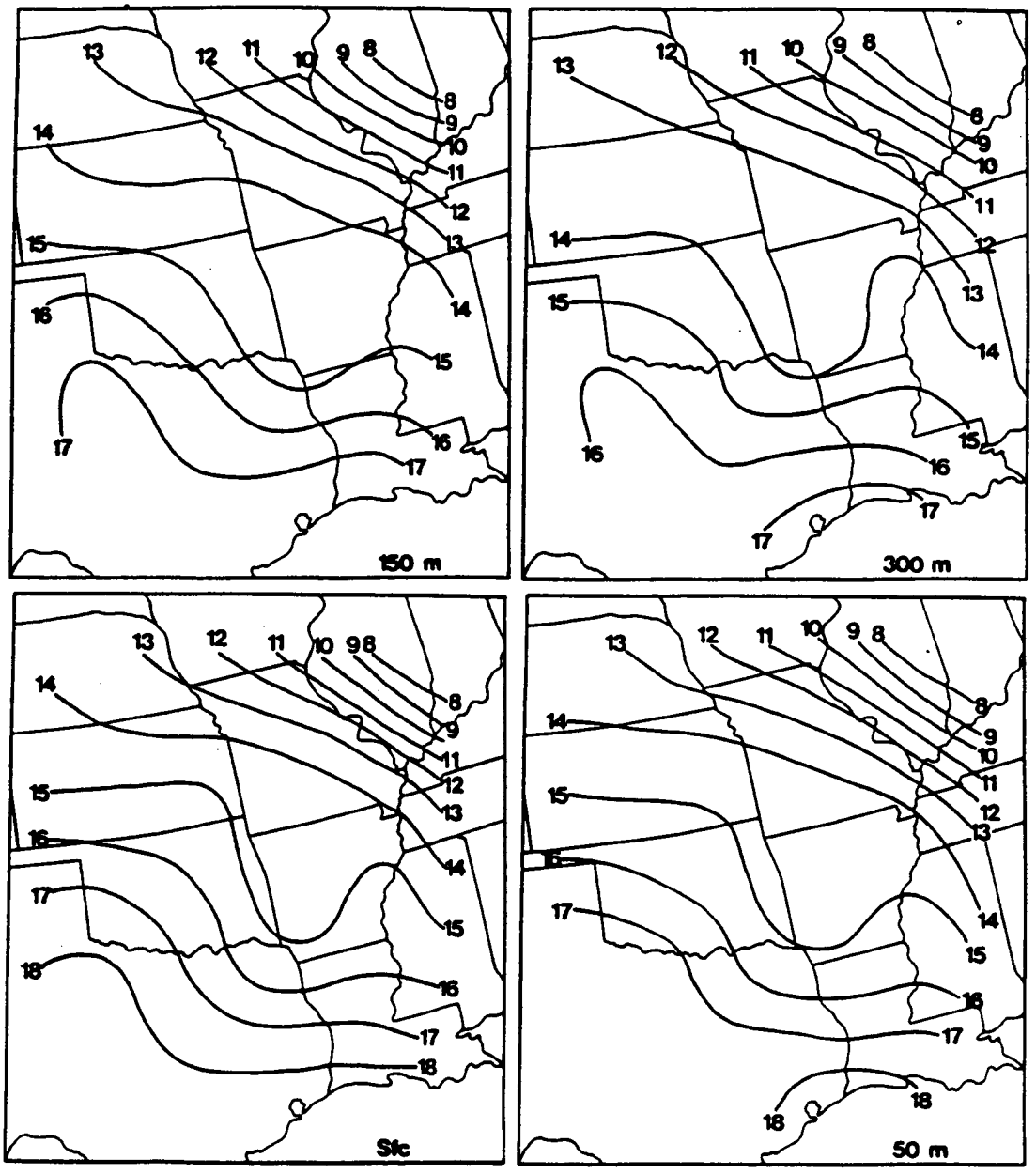


Fig. 10. Objectively analyzed fields of input TIROS-N temperatures (°C).

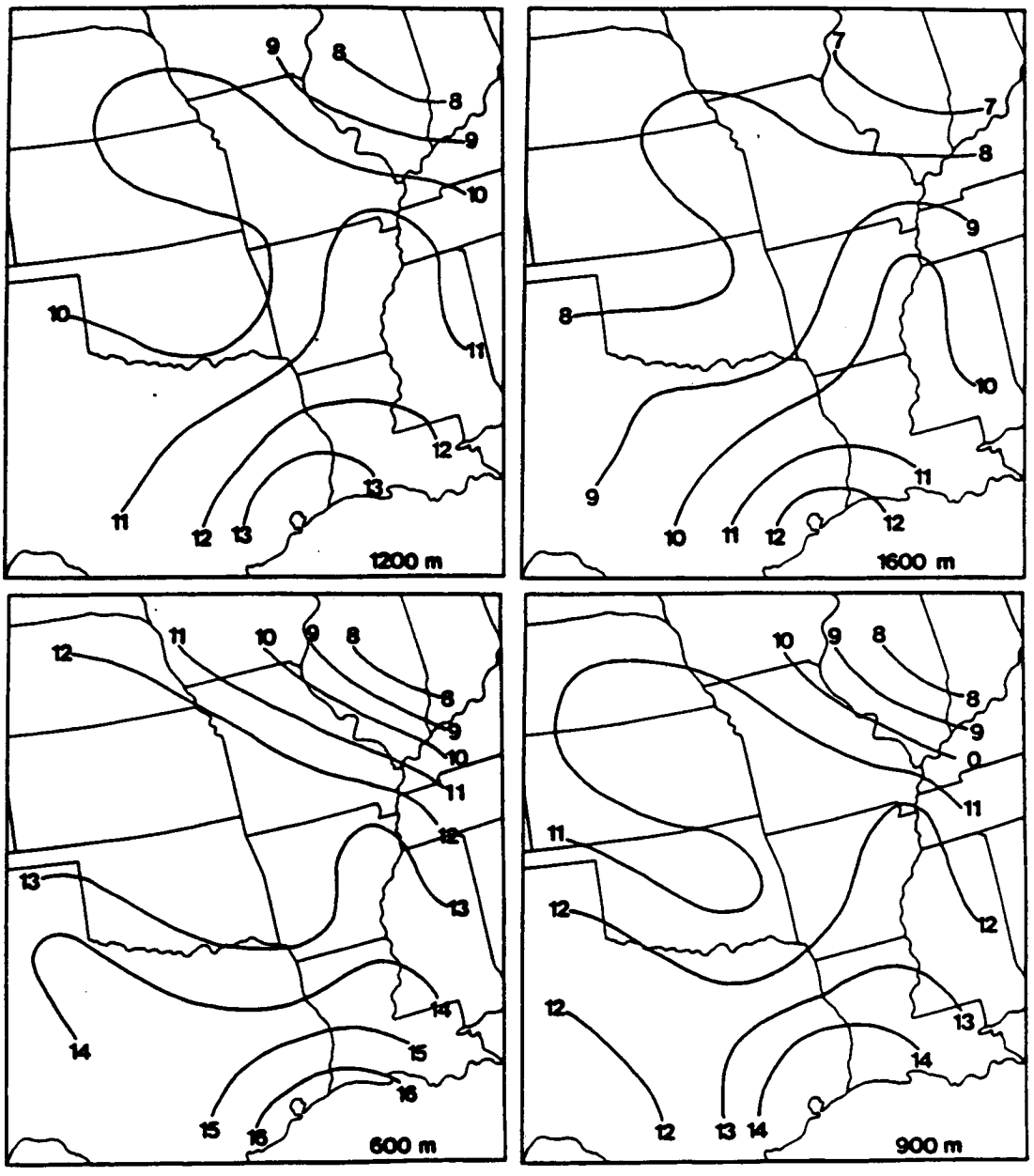


Fig. 10. Continued.

Table 1. Average and maximum values, as well as standard deviations (σ), of the gridded RAOB and satellite temperature, dewpoint and pressure fields.

RAOB

| | Temperature (°C) | | | Dewpoint (°C) | | | Pressure (mb) | | |
|---|---|---|---|---|---|---|---|---|---|
| Level (m) | Avg | Max | σ | Avg | Max | σ | Avg | Max | σ |
| 1600 | 11.1 | 13.8 | 1.4 | 3.8 | 10.0 | 6.1 | 824 | 844 | 13.4 |
| 1200 | 13.4 | 15.8 | 1.1 | 7.1 | 12.8 | 4.0 | 864 | 885 | 14.1 |
| 900 | 15.0 | 17.5 | 1.3 | 7.2 | 15.0 | 8.5 | 896 | 917 | 14.6 |
| 600 | 16.0 | 19.5 | 1.7 | 10.0 | 16.9 | 5.4 | 928 | 950 | 15.0 |
| 300 | 16.4 | 20.8 | 2.0 | 11.2 | 18.8 | 5.4 | 961 | 984 | 15.4 |
| 150 | 16.2 | 20.3 | 2.0 | 12.2 | 19.0 | 4.5 | 979 | 1000 | 15.7 |
| 50 | 16.0 | 19.4 | 2.2 | 12.8 | 18.3 | 4.0 | 990 | 1010 | 15.9 |
| Sfc | 15.7 | 19.8 | 2.4 | 13.0 | 18.2 | 3.7 | 996 | 1020 | 15.9 |

TIROS-N

| | Temperature (°C) | | | Dewpoint (°C) | | | Pressure (mb) | | |
|---|---|---|---|---|---|---|---|---|---|
| Level (m) | Avg | Max | σ | Avg | Max | σ | Avg | Max | σ |
| 1600 | 8.9 | 12.2 | 1.2 | -1.2 | 10.3 | 4.5 | 822 | 843 | 13.2 |
| 1200 | 10.6 | 13.7 | 1.1 | 2.8 | 12.3 | 4.6 | 863 | 884 | 13.8 |
| 900 | 11.7 | 14.9 | 1.2 | 5.4 | 13.6 | 4.4 | 895 | 917 | 14.2 |
| 600 | 12.8 | 16.1 | 1.5 | 7.7 | 15.1 | 4.1 | 927 | 950 | 14.7 |
| 300 | 13.9 | 17.3 | 1.8 | 9.9 | 16.4 | 3.8 | 961 | 984 | 15.2 |
| 150 | 14.5 | 17.8 | 2.0 | 10.9 | 17.0 | 3.7 | 978 | 1000 | 15.5 |
| 50 | 14.9 | 18.2 | 2.1 | 11.6 | 17.3 | 3.6 | 990 | 1010 | 15.7 |
| Sfc | 15.1 | 18.4 | 2.2 | 12.0 | 17.7 | 3.6 | 996 | 1020 | 15.7 |

1976; Moyer et al., 1978).

Statistics for the gridded dewpoint temperatures are also presented in Table 1. Average values indicate that TIROS-N diagnosed the atmosphere as being drier than when "observed" by rawinsondes, particularly at 1200 and 1600 m AGL. Maximum values of satellite-derived dewpoints are also consistently "drier" (smaller) than their RAOB counterparts, except at 1600 m AGL where a slightly larger value is noted. Based on the computed standard deviations, less vertical variation is found in the satellite data than in the RAOB data. This is indicative of the volumetric sampling of the satellite's radiometers that results in considerably less vertical resolution than is obtainable from radiosondes. Also, the satellite standard deviations are substantially smaller than rawinsonde-derived versions in the midlevels, particularly at 900 m AGL where values are 4.4 and 8.5°C, respectively.

The relative inability of TIROS-N to capture features of the moisture field is clearly revealed in patterns of dewpoint depression. In the RAOB data (Fig. 11), the highest moisture content is found along a line stretching from Texas to Nebraska. This feature is evident at all levels, tilting to the east with height. Drier air is indicated along the Mississippi River Valley, and, above 900 m AGL, in the western third of the area. Although differences are evident between the pat-

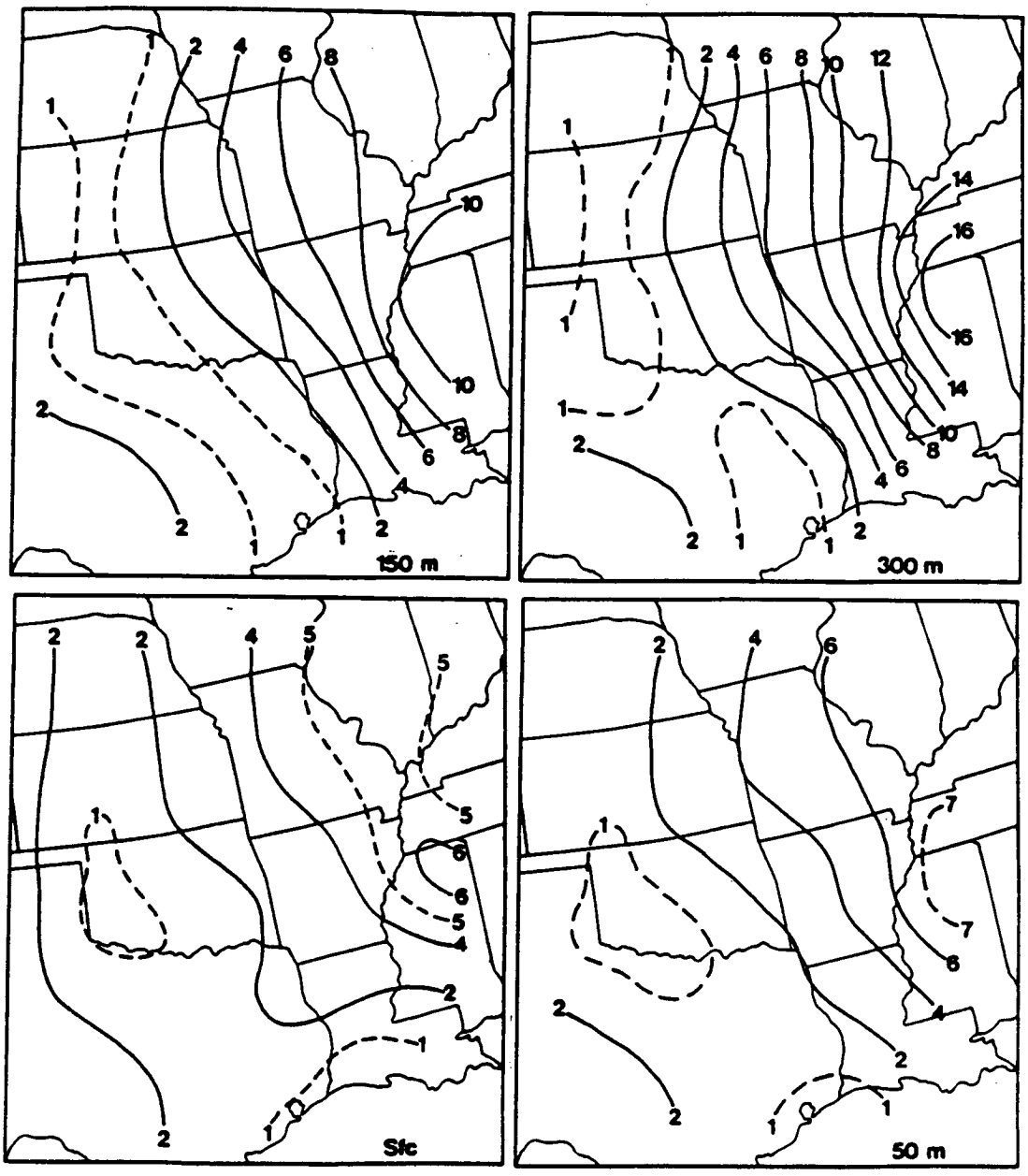


Fig. 11. Patterns of dewpoint depression based on objectively analyzed fields of input RAOB dewpoint temperatures (°C).

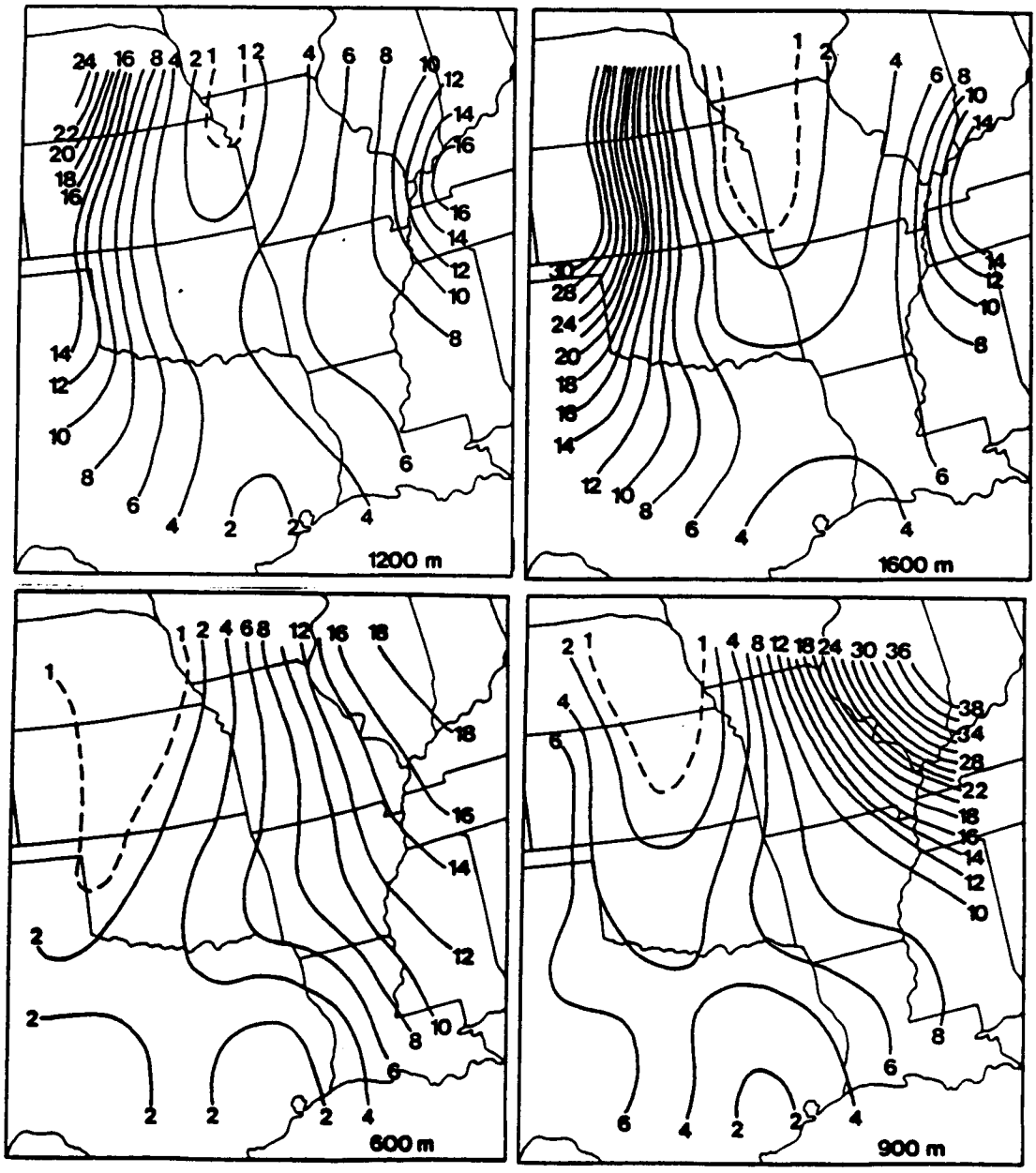


Fig. 11. Continued.

terns derived from RAOB and satellite data, common features include the southern extent of the moist tongue through the midsection of the region, as well as the drier area along the central Mississippi River Valley (Fig. 12).

Input fields of pressure from the RAOB and satellite data are nearly identical at all model levels. This can be seen both in the statistics (Table 1) and in the horizontal fields shown in Figs. 13 and 14. Generally, a ridge of high pressure stretches from the Gulf of Mexico to Illinois. A weak trough along the eastern Kansas-Oklahoma border is oriented toward southwestern Missouri. Additionally, low pressure extends along the western boundary of the region.

b. Evaluation of RAOB-derived winds

Fields of horizontal winds obtained from rawinsonde thermal data will now be compared with observed ("actual") patterns. Based on various statistics that are described later, the "best" and "worst" results generally occur at 300 m and 1200 m, respectively. Thus, gridded vector depictions of the various winds will be presented for these levels. In addition, fields at 50 m AGL are included to show details at the surface layer/transition layer interface.

1) "Actual" winds

"Actual" wind fields at 50, 300, 1200 m AGL are shown in

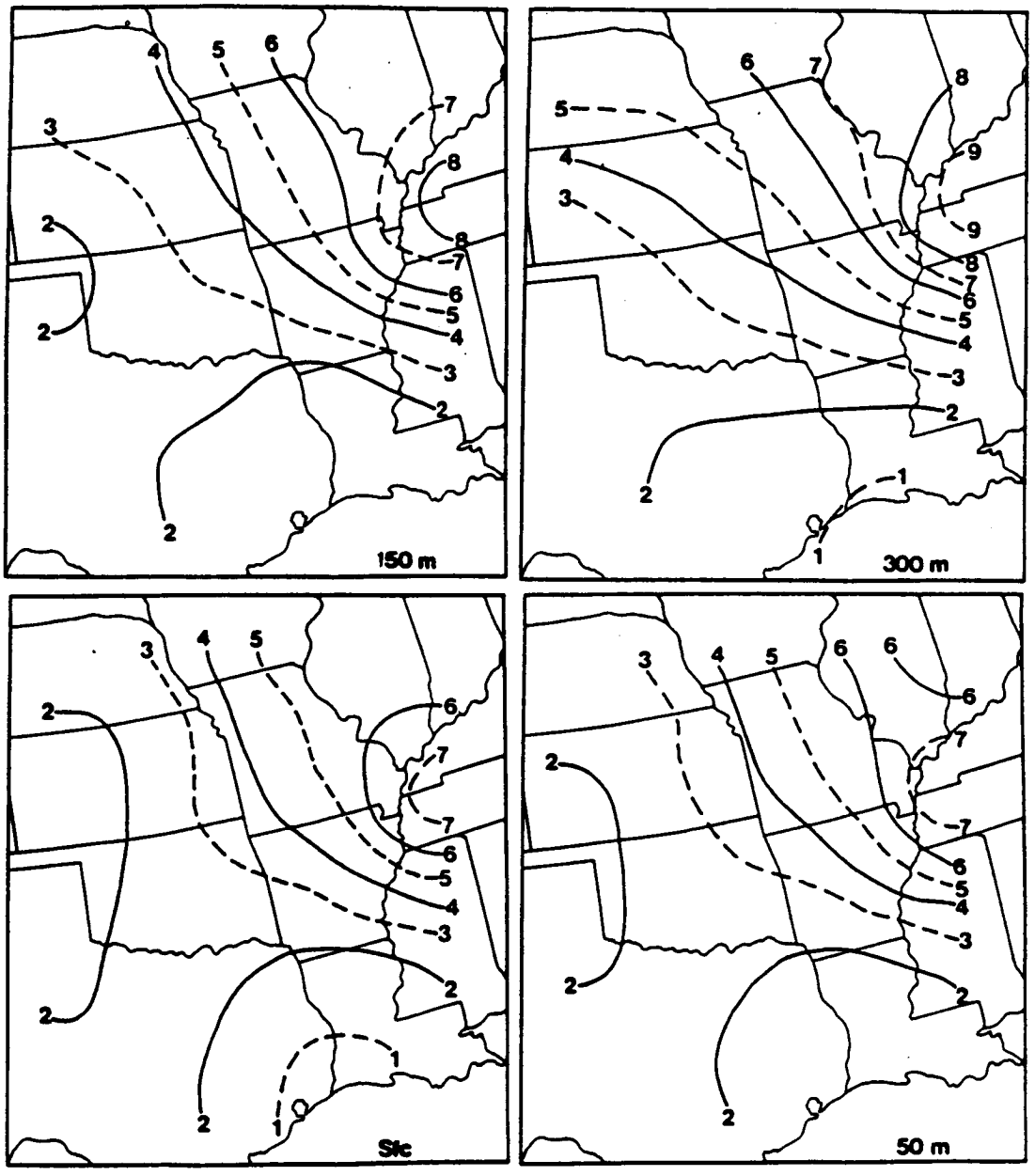


Fig. 12. Patterns of dewpoint depression based on objectively analyzed fields of input TIROS-N dewpoint temperatures (°C).

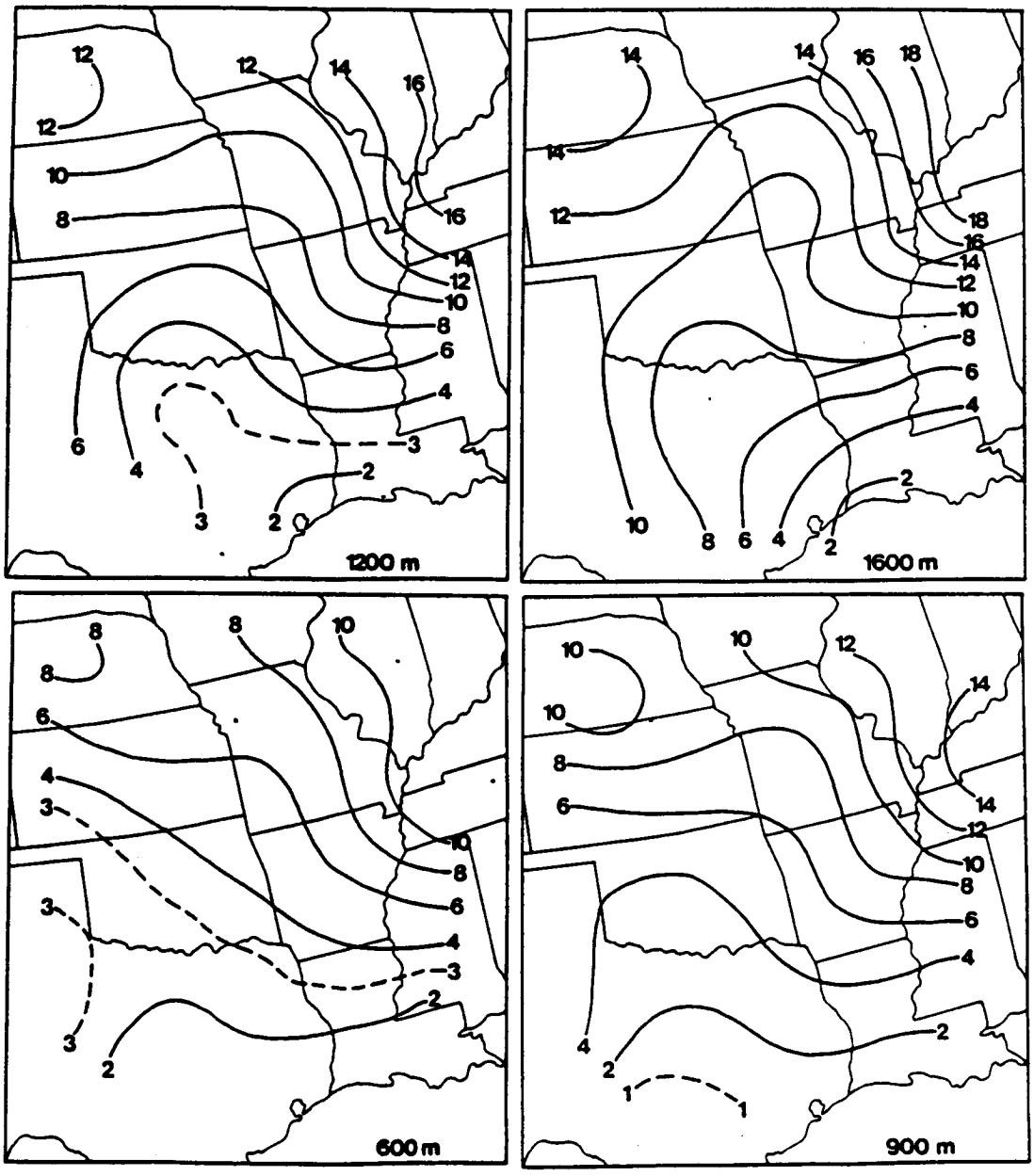


Fig. 12. Continued.

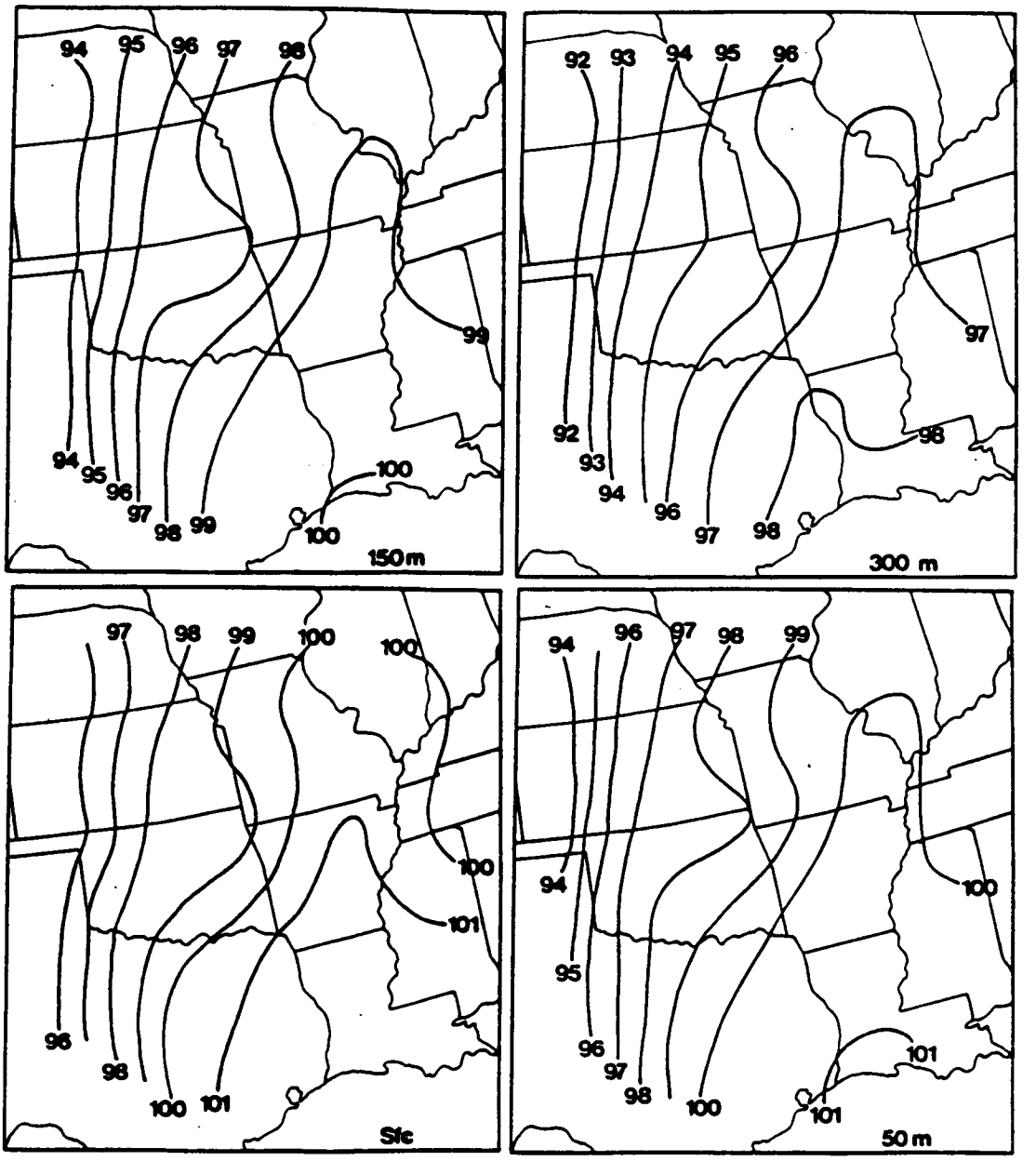


Fig. 13. Objectively analyzed fields of input RAOB pressures ($10^1$ mb).

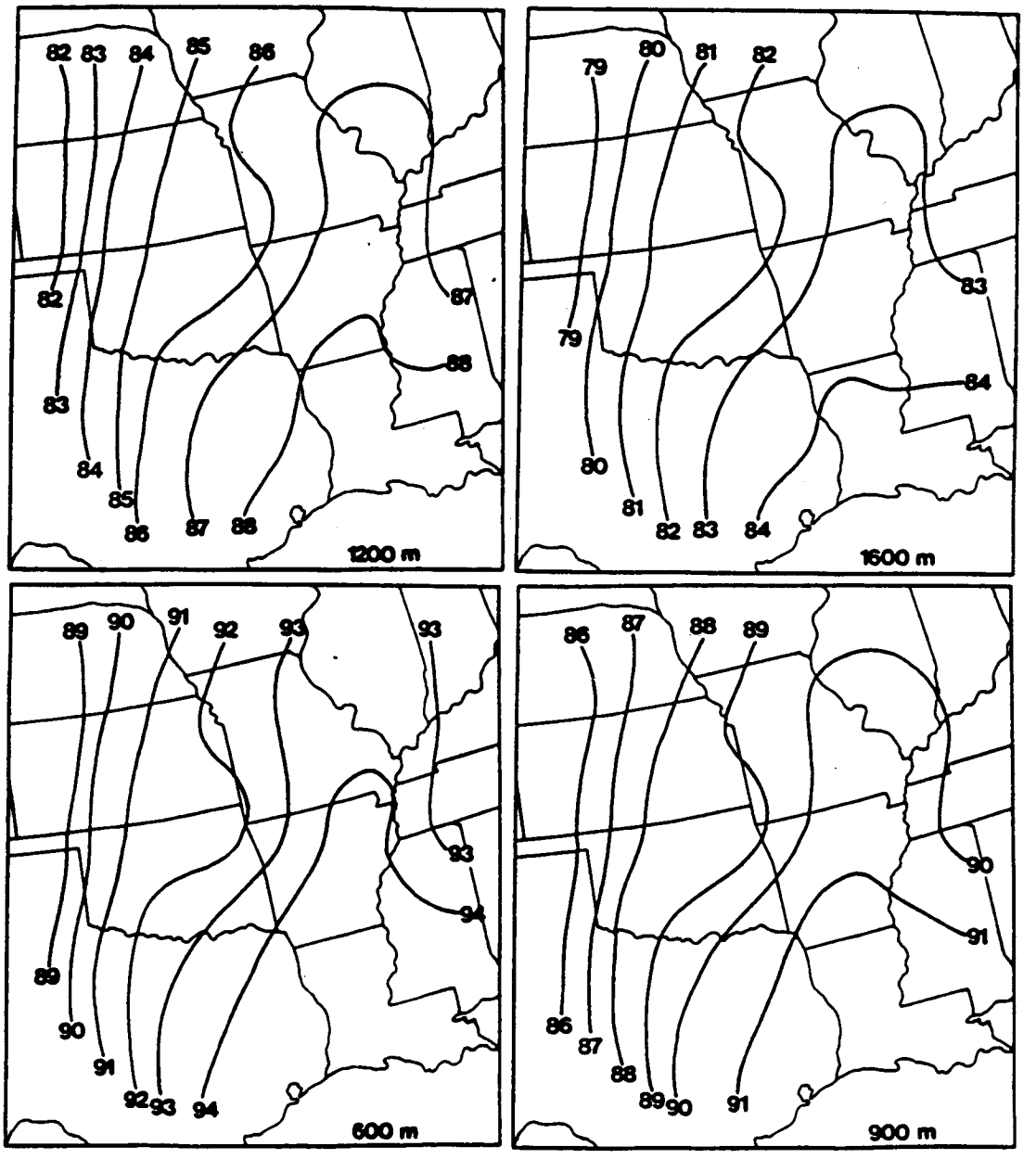


Fig. 13. Continued.

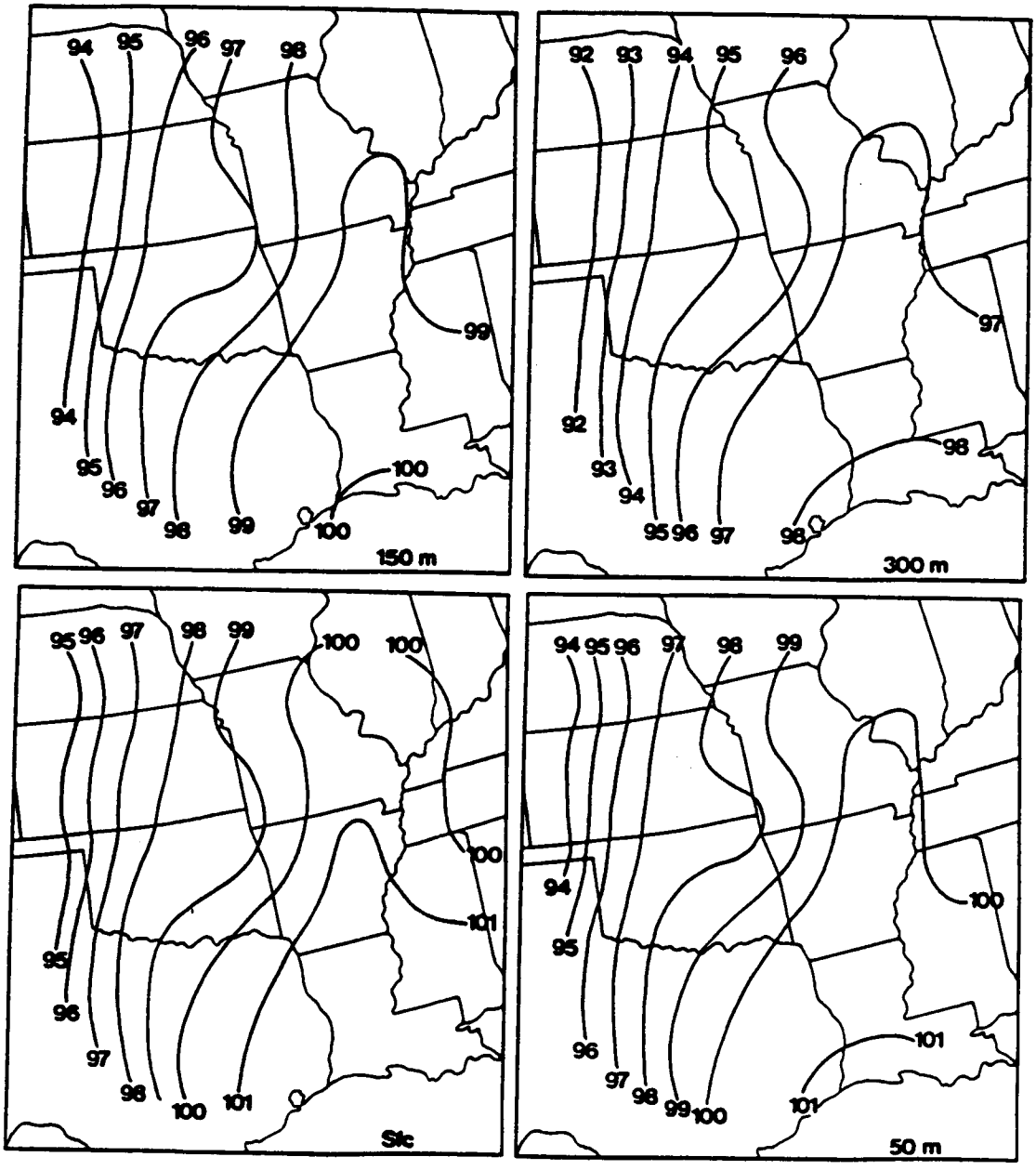


Fig. 14. Objectively analyzed fields of input TIROS-N pressures ($10^1$ mb).

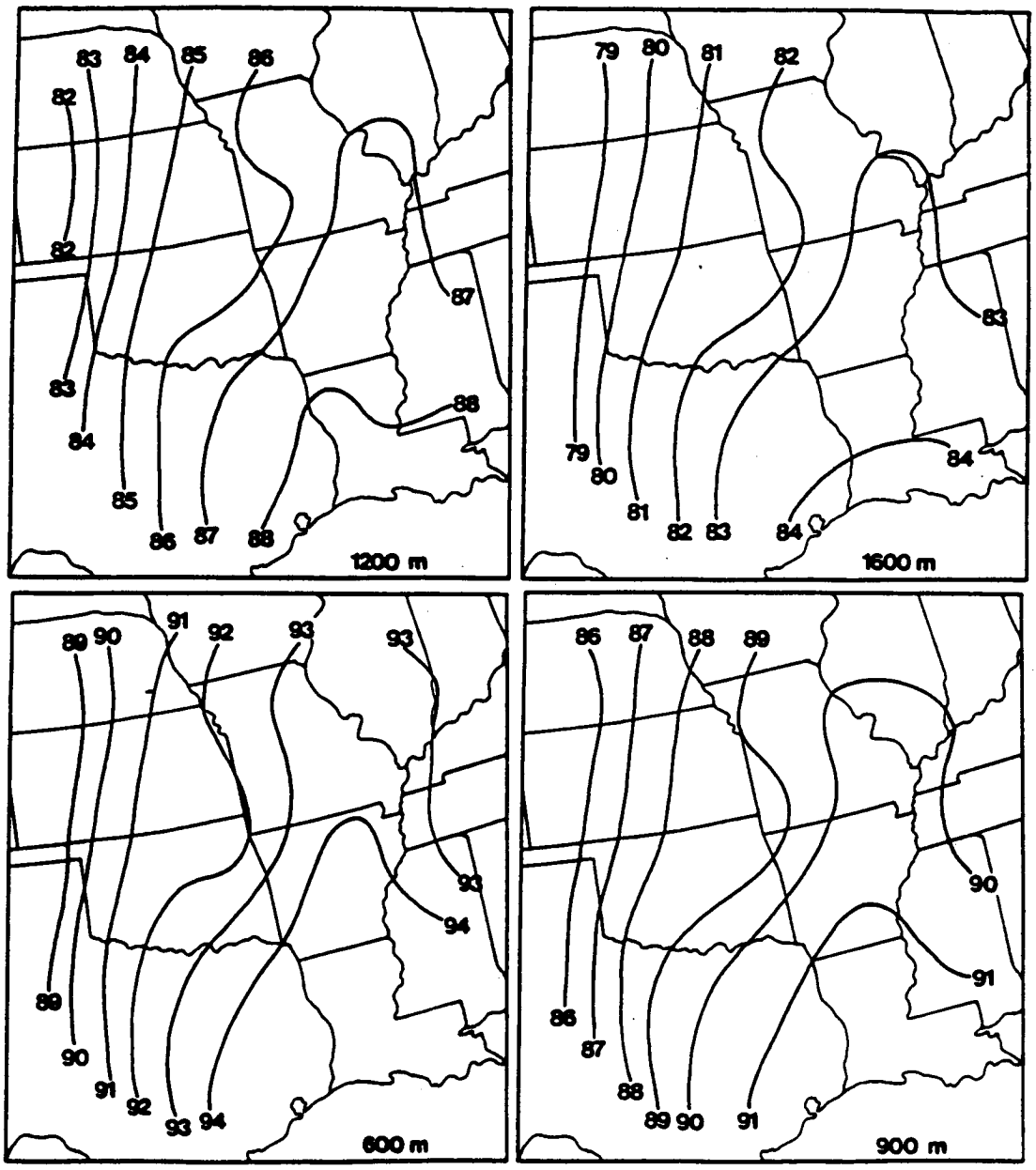


Fig. 14. Continued.

Fig. 15. Meridional flow is predominant over the area, with the wind directions veering from south-southeast to south-southwest with height. Comparison with Fig. 13 reveals that winds in the lowest levels are crossing the isobars toward lower pressure, as is expected near the surface. The southerly flow pattern is also evident in the horizontal mean values given in Table 2. The vertically averaged u-component is -1.9 m $s^{-1}$, while the average v-component is much stronger (10.3 m $s^{-1}$). Standard deviations of the v-components are greater than those for the u-components; vertical averages are 3.7 and 2.8 m $s^{-1}$, respectively. Wind speeds through the PBL average 11.8 m $s^{-1}$, with strongest mean values occurring at 600 m and 900 m AGL. Standard deviations of the wind speeds at individual levels fall between corresponding values for the two components.

Since "actual" fields are based on only 26 observation sites with an average spacing of slightly less than 400 km (Fig. 4), the resulting patterns should contain somewhat less detail than obtained from thermally-derived winds based on either the 39 RAOB soundings (with $\sim$250 km spacings) or the 62 satellite soundings (with $\sim$150 km spacings). This result is expected even though each of the three data sets was objectively analyzed to achieve approximately a 50% response for wavelengths of 1000 km.

2) RAOB-derived winds

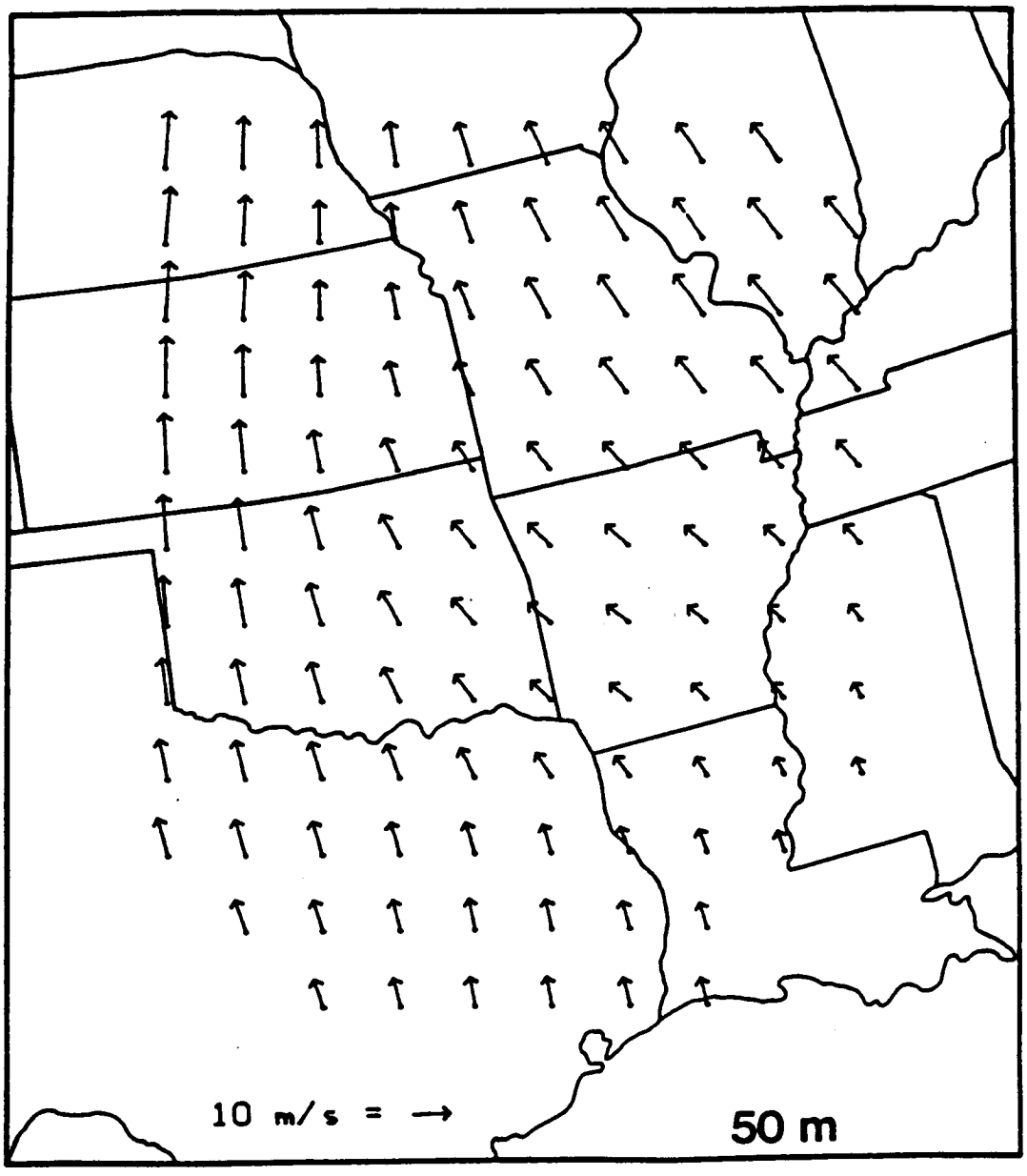


Fig. 15. "Actual" wind fields (m $s^{-1}$) at 50, 300 and 1200 m AGL.

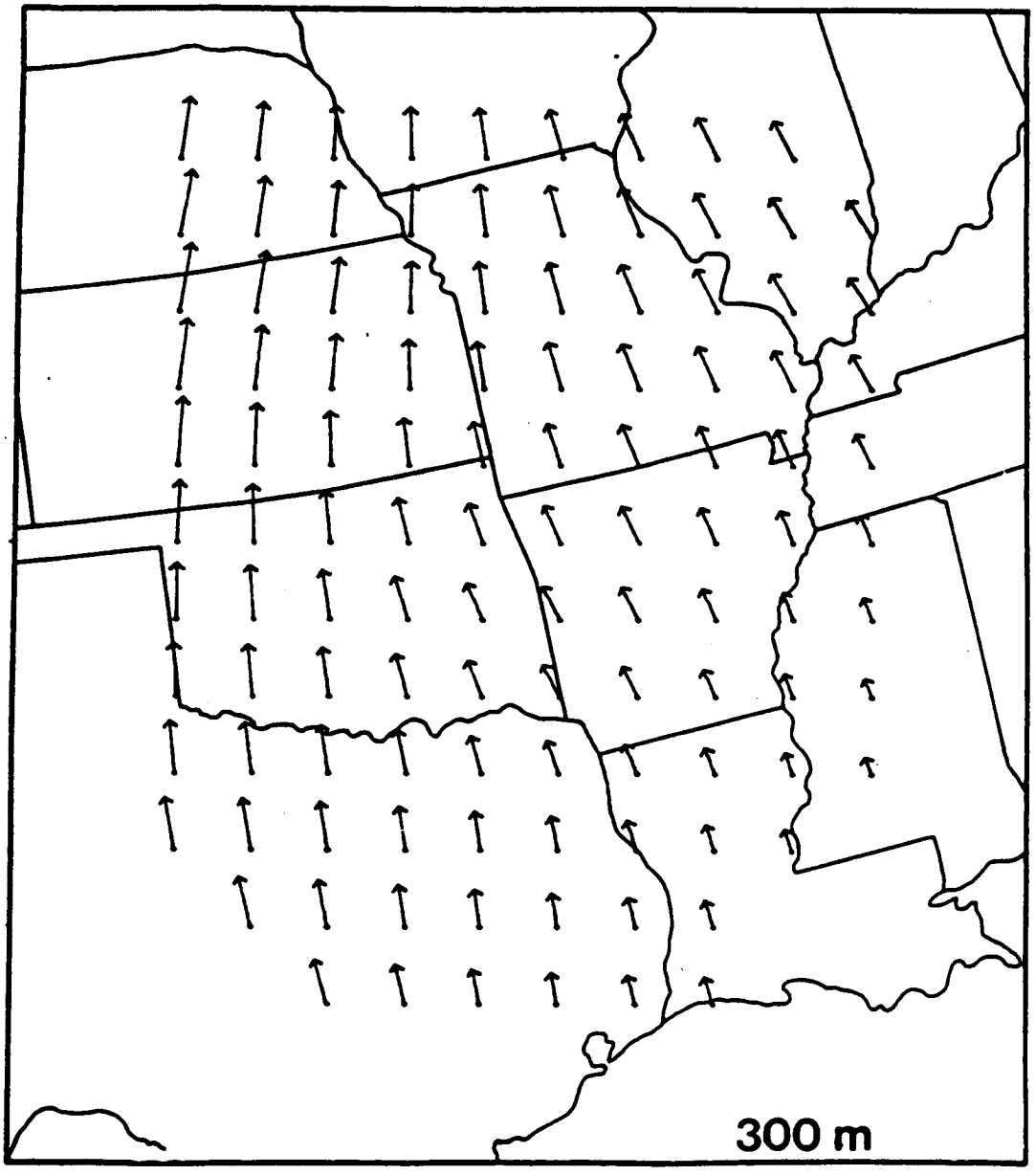


Fig. 15. Continued.

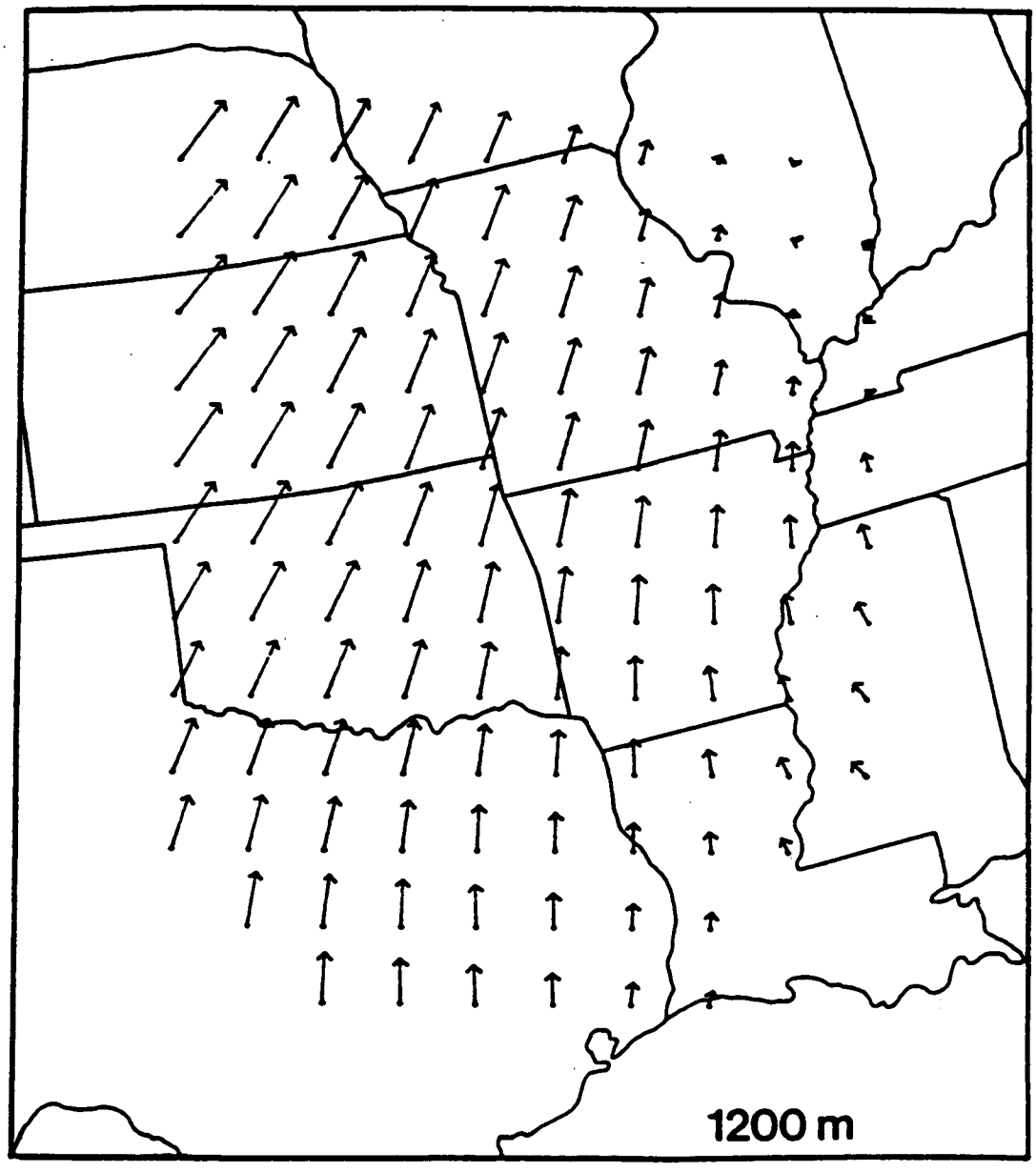


Fig. 15. Continued.

Table 2. Mean values and standard deviations (m $s^{-1}$) for "actual" wind data. Values at each above-ground model level, as well as vertical averages, are given for the u- and v-components and wind speed.

| | Level (m) | Mean | σ |
|---|---|---|---|
| u-component: | 1600 | 1.9 | 2.9 |
| | 1200 | 0.8 | 3.4 |
| | 900 | 0.3 | 3.0 |
| | 600 | -1.2 | 2.6 |
| | 300 | -4.7 | 2.3 |
| | 150 | -5.3 | 2.6 |
| | 50 | -5.1 | 2.5 |
| | Average | -1.9 | 2.8 |
| v-component: | 1600 | 9.3 | 3.8 |
| | 1200 | 11.4 | 5.3 |
| | 900 | 12.3 | 5.4 |
| | 600 | 12.4 | 4.8 |
| | 300 | 10.2 | 3.3 |
| | 150 | 8.6 | 3.1 |
| | 50 | 7.6 | 3.2 |
| | Average | 10.3 | 3.7 |
| Wind Speed: | 1600 | 10.4 | 3.6 |
| | 1200 | 12.4 | 5.2 |
| | 900 | 13.2 | 5.3 |
| | 600 | 13.3 | 4.5 |
| | 300 | 12.1 | 2.8 |
| | 150 | 11.1 | 2.6 |
| | 50 | 10.1 | 2.7 |
| | Average | 11.8 | 3.8 |

Standard geostrophic wind fields, computed using (3-26) and (3-27), are presented as an often-used procedure with which to assess the usefulness of the modified Ekman technique. RAOB-derived geostrophic winds, shown in Fig. 16, appear unrealistic at 50 m AGL. Speeds are as great as 33.0 m $s^{-1}$, much stronger than "actual" values (Fig. 15). Differences in wind direction are also quite pronounced. The area of light and variable winds in the eastern portion of the area is quite reasonable since it is located near the center of the high pressure ridge (Fig. 13). One should note that this feature was not resolved by the "actual" winds due to inadequate contact data in the area (Fig. 4). Geostrophic winds at 300 m AGL are more compatible with "actual" values, however they still are stronger than observed speeds. At 1200 AGL, the RAOB-derived geostrophic winds most closely resemble their "actual" counterparts. This improvement with increasing altitude is expected since the effects of friction decrease with height.

Application of the modified Ekman scheme (Chapter 5, Section c) results in the RAOB-derived winds shown in Fig. 17. The Ekman winds appear quite comparable to corresponding "actual" values (Fig. 15), particularly at 300 m AGL. The modified wind patterns appear more reasonable than "actual" values in two areas. First, the Ekman fields exhibit a more realistic light and variable character in the lower levels near the high pressure ridge. Second, along the western border of

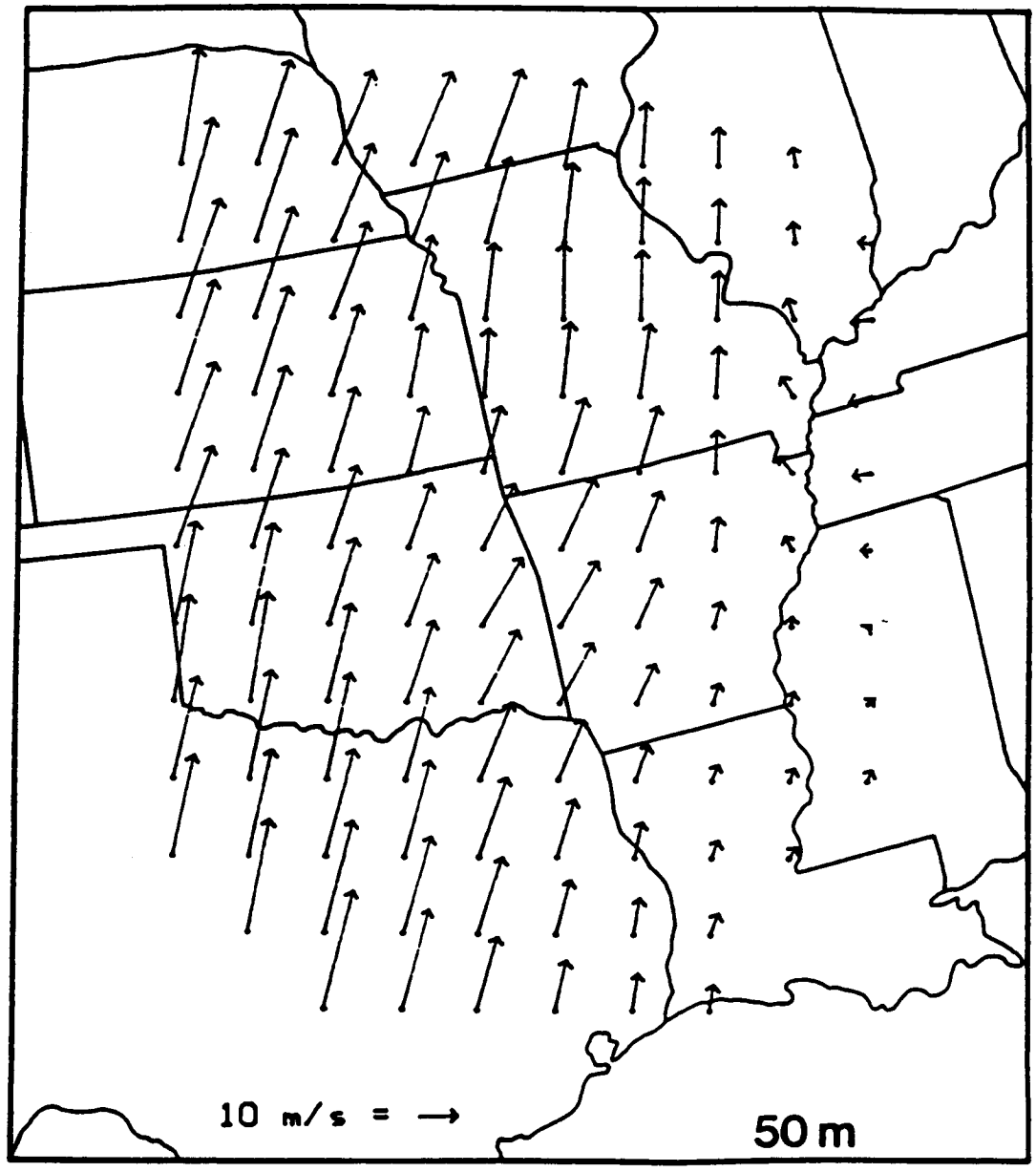


Fig. 16. RAOB-derived standard geostrophic wind fields (m $s^{-1}$) at 50, 300 and 1200 m AGL.

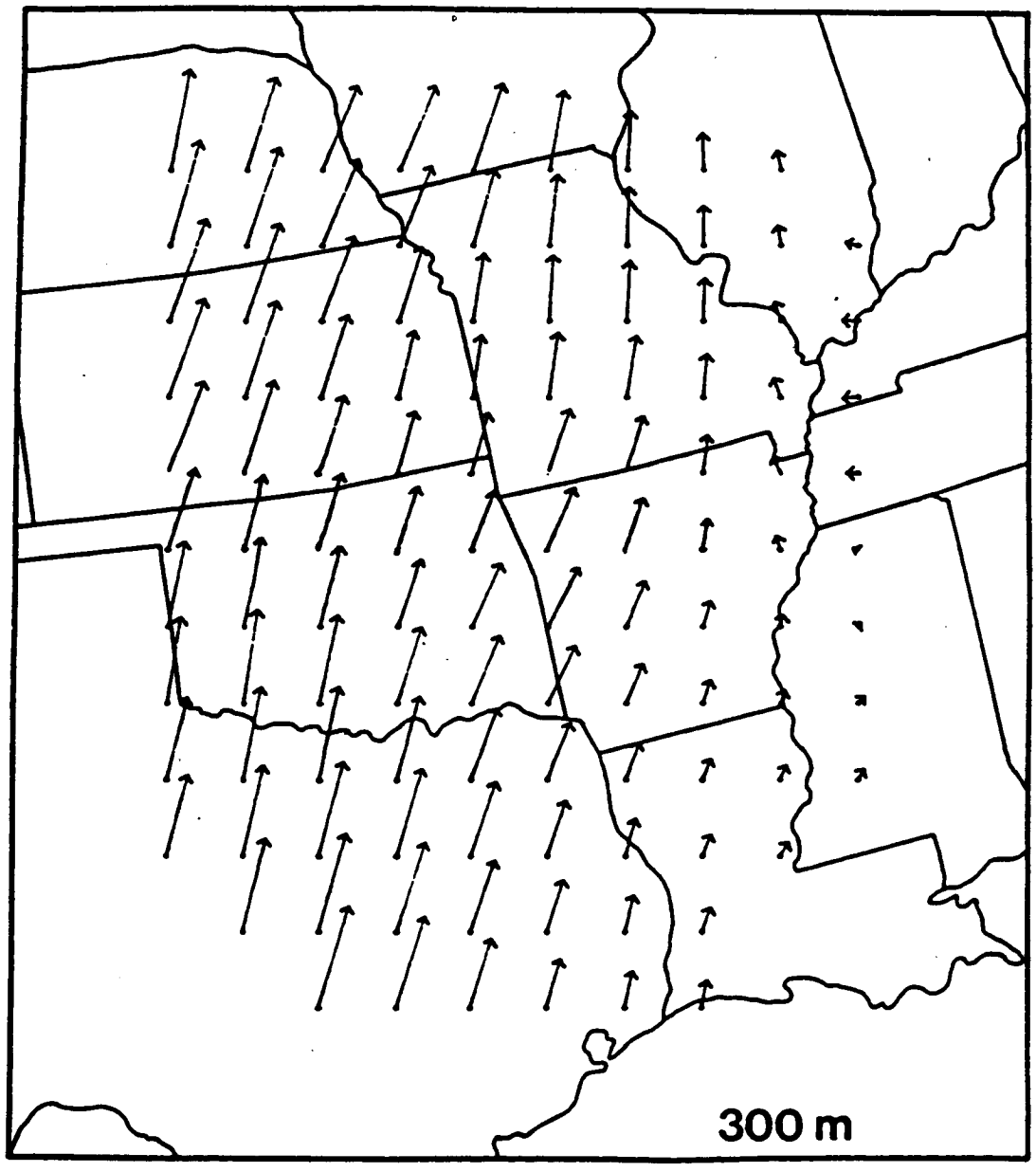


Fig. 16. Continued.

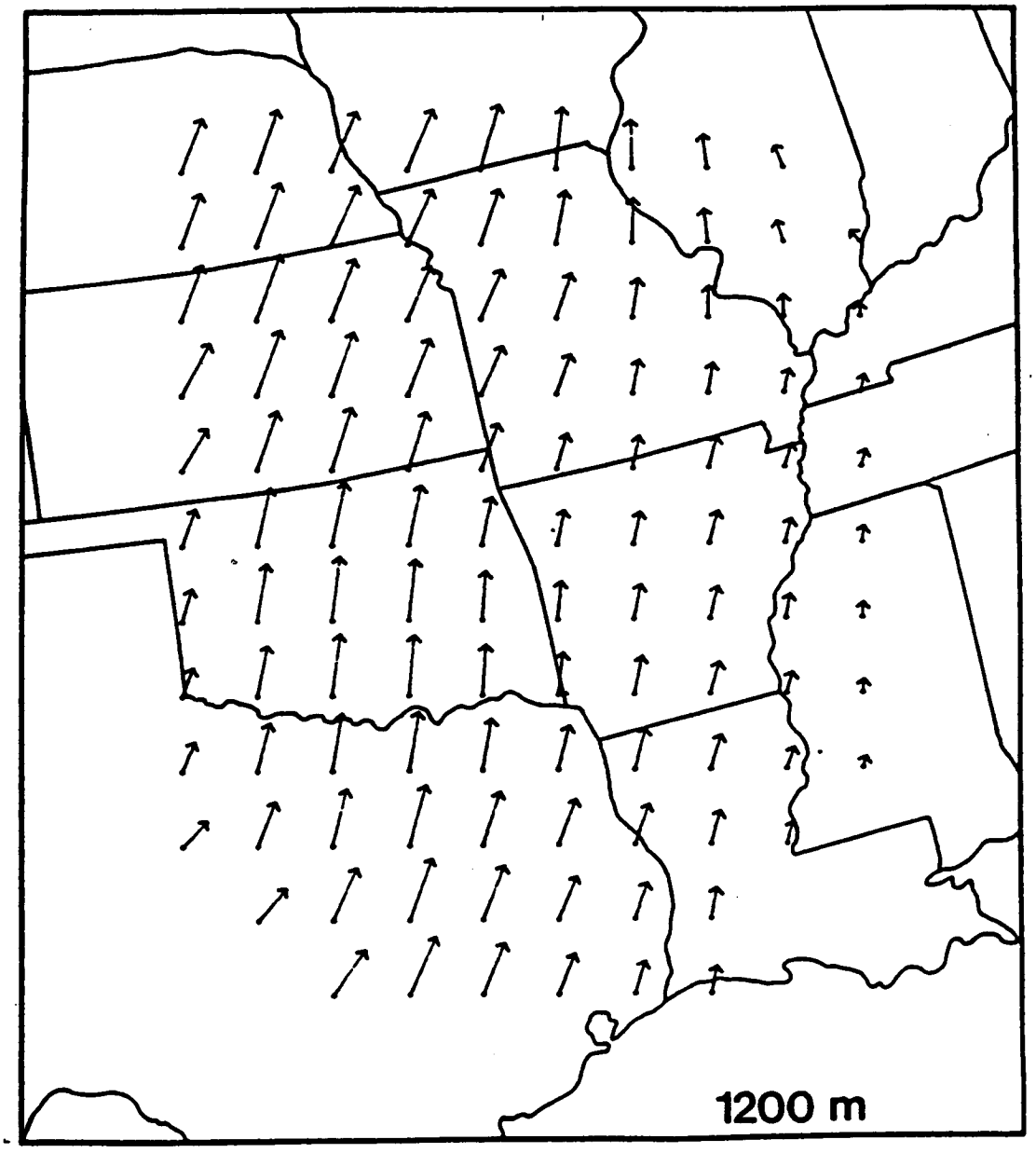


Fig. 16. Continued.

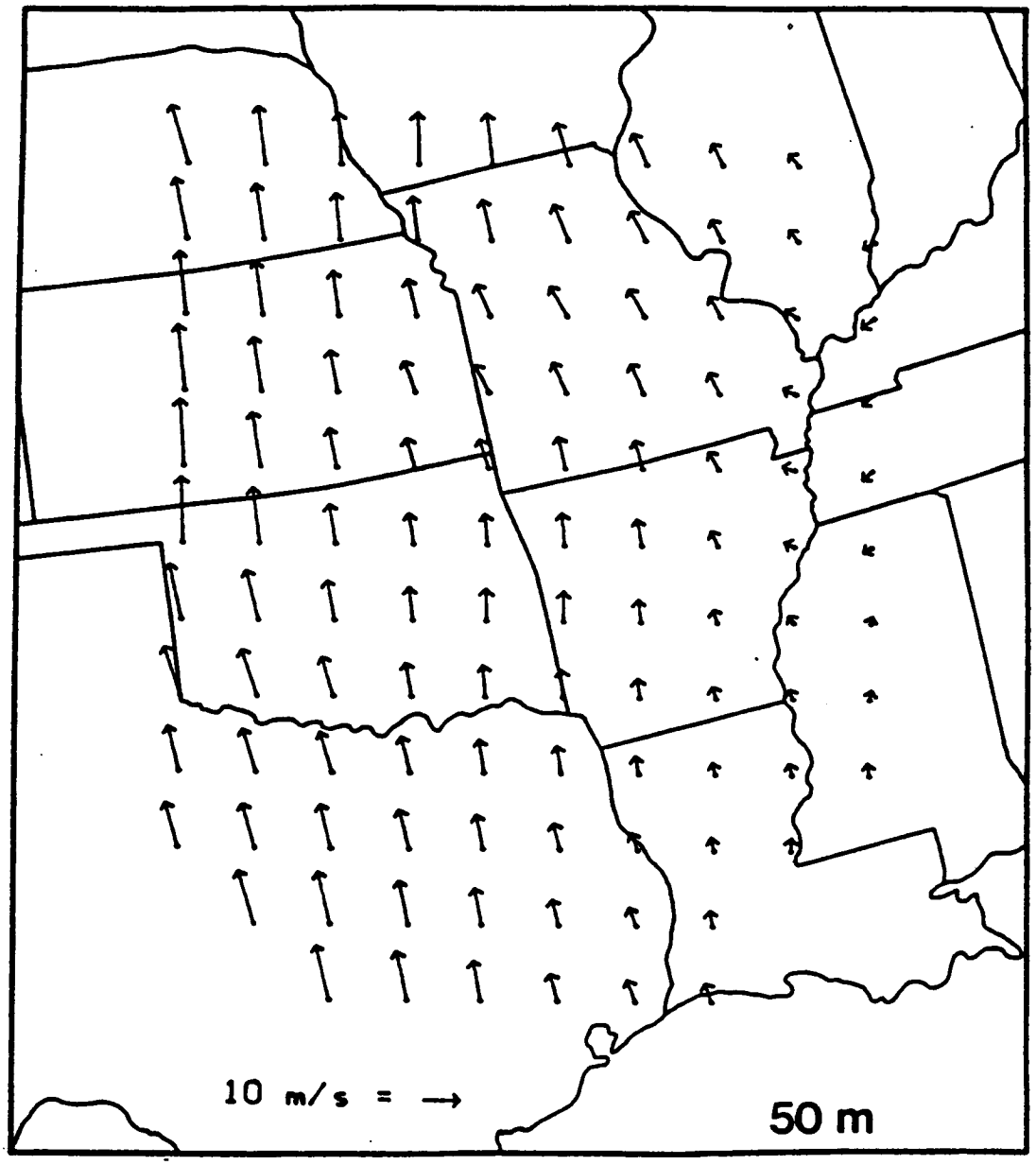


Fig. 17. RAOB-derived modified Ekman wind fields (m $s^{-1}$) at 50, 300 and 1200 m AGL.

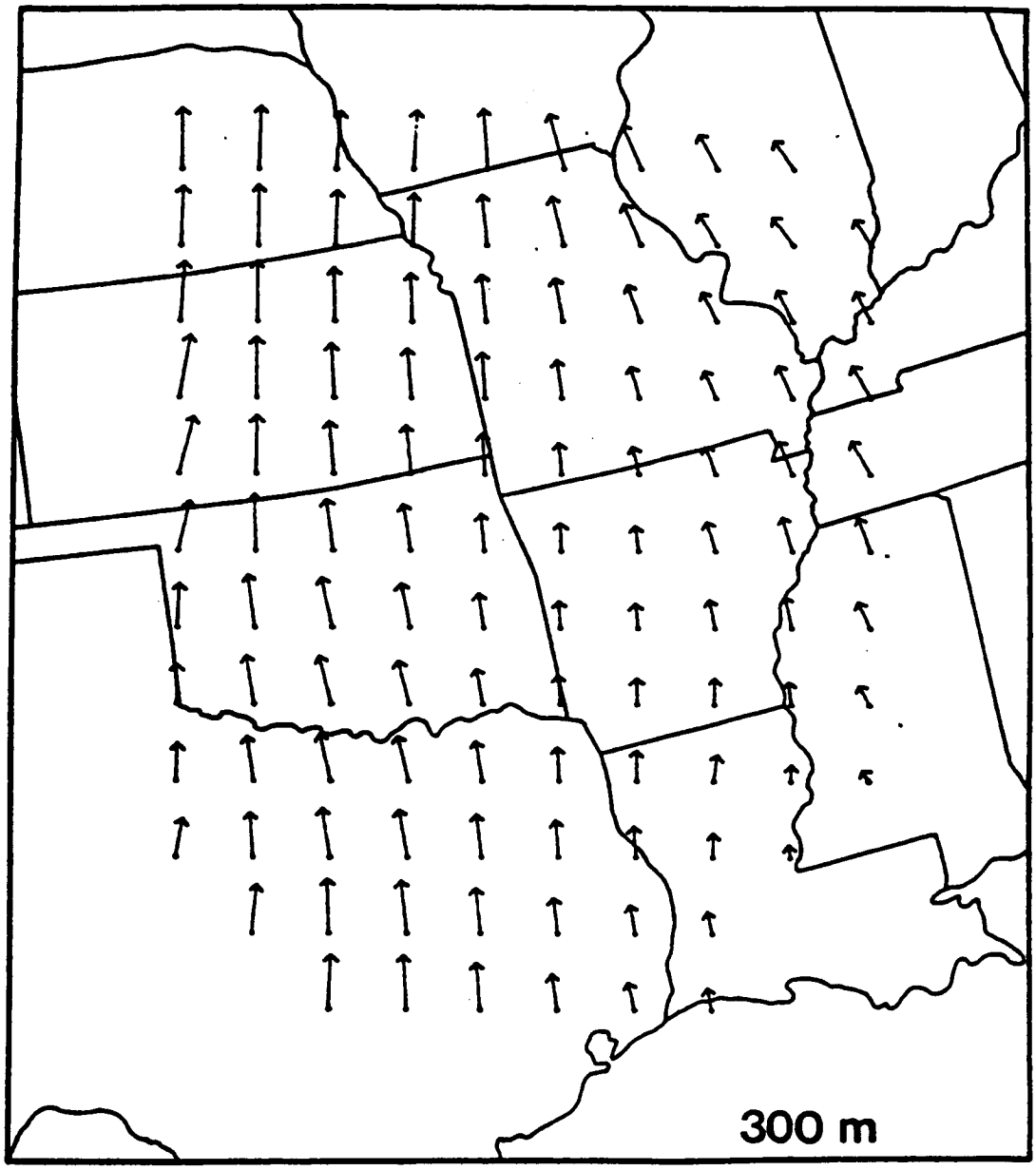


Fig. 17. Continued.

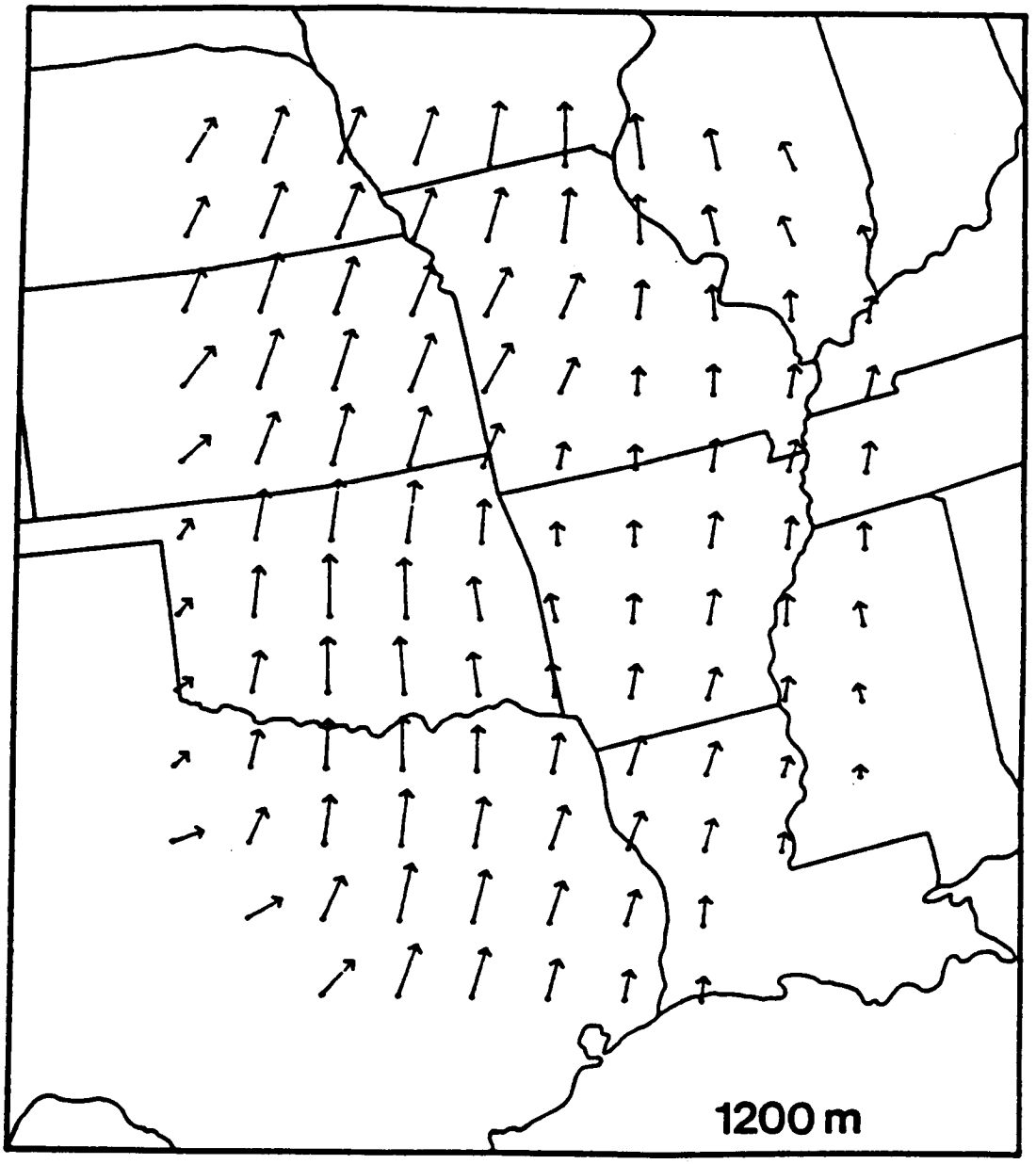


Fig. 17. Continued.

the region above 300 m AGL, the Ekman winds depict more counterclockwise flow, reflecting the presence of a north-south oriented trough located just outside the grid area. Comparing Figs. 16 and 17, it is apparent that the Ekman approach has produced more realistic wind speeds at the lowest levels than the geostrophic technique. Although both geostrophic and Ekman winds reflect the western trough and eastern pressure ridge, the Ekman vectors flow more toward low pressure than do their stronger geostrophic counterparts.

Various statistical comparisons between the "actual" and two RAOB-derived wind sets are given in Tables 4 through 6. First, however, mean values and standard deviations of the fields represented by Figs. 16 and 17 are presented in Table 3. Horizontal means again reflect fairly light u-components, with the geostrophic values being smaller than Ekman values. Since isobars are predominantly oriented along a north-south direction (Fig. 13), the greater Ekman u-components reflect an enhanced cross-isobaric flow than occurs with observed values (Table 2). The Ekman wind speeds are, correspondingly, smaller than their geostrophic counterparts. Maximum Ekman winds occur at 600-900 m AGL (as do the "actual" winds), as opposed to the geostrophic values which continually decrease with altitude. Standard deviations for the Ekman data generally are much less than those for the geostrophic winds, particularly in the lowest levels. The only exceptions are for the u-component;

Table 3. Same as Table 2, except for RAOB-derived standard geostrophic and modified Ekman winds.

| | | Geostrophic | | Ekman | |
|---|---|---|---|---|---|
| | Level (m) | Mean | σ | Mean | σ |
| u-component: | 1600 | 0.4 | 2.6 | 0.5 | 2.8 |
| | 1200 | 0.7 | 2.2 | -0.2 | 2.9 |
| | 900 | 0.9 | 2.1 | -1.1 | 2.8 |
| | 600 | 0.9 | 2.1 | -2.3 | 2.5 |
| | 300 | 0.8 | 2.5 | -3.7 | 2.0 |
| | 150 | 0.7 | 2.7 | -4.2 | 1.5 |
| | 50 | 0.7 | 2.9 | -3.8 | 1.5 |
| | Average | 0.7 | 2.4 | -2.1 | 2.3 |
| v-component: | 1600 | 9.6 | 3.4 | 9.9 | 3.6 |
| | 1200 | 11.6 | 4.3 | 10.4 | 3.7 |
| | 900 | 13.1 | 5.4 | 10.7 | 3.7 |
| | 600 | 14.5 | 6.8 | 10.7 | 3.5 |
| | 300 | 16.0 | 8.2 | 9.8 | 3.4 |
| | 150 | 16.8 | 9.1 | 8.6 | 3.9 |
| | 50 | 17.4 | 9.6 | 7.5 | 4.6 |
| | Average | 14.1 | 6.7 | 9.7 | 3.8 |
| Wind Speed: | 1600 | 10.5 | 3.2 | 10.8 | 3.3 |
| | 1200 | 12.3 | 4.2 | 11.3 | 3.5 |
| | 900 | 13.7 | 5.4 | 11.6 | 3.5 |
| | 600 | 15.2 | 6.6 | 11.7 | 3.3 |
| | 300 | 16.9 | 7.9 | 11.2 | 3.1 |
| | 150 | 17.8 | 8.6 | 10.4 | 3.3 |
| | 50 | 18.4 | 9.0 | 9.3 | 4.1 |
| | Average | 15.0 | 6.4 | 10.9 | 3.4 |

Table 4. Standard deviations of "actual" u, v and wind speed (repeated from Table 2) compared with root-mean-square errors of RAOB-derived standard geostrophic and modified Ekman wind data. Units are m $s^{-1}$.

| | Level (m) | "Actual" σ | RAOB-Geo RMSE | RAOB-Ekman RMSE |
|---|---|---|---|---|
| u-component: | 1600 | 2.9 | 3.4 | 3.4 |
| | 1200 | 3.4 | 3.2 | 3.5 |
| | 900 | 3.0 | 2.5 | 3.1 |
| | 600 | 2.6 | 2.9 | 2.6 |
| | 300 | 2.3 | 5.8 | 2.0 |
| | 150 | 2.6 | 6.4 | 2.5 |
| | 50 | 2.5 | 6.2 | 3.2 |
| | Average | 2.8 | 4.3 | 2.9 |
| v-component: | 1600 | 3.8 | 3.6 | 3.6 |
| | 1200 | 5.3 | 3.0 | 4.4 |
| | 900 | 5.4 | 2.6 | 4.4 |
| | 600 | 4.8 | 3.7 | 3.3 |
| | 300 | 3.3 | 8.1 | 1.5 |
| | 150 | 3.1 | 10.7 | 2.2 |
| | 50 | 3.2 | 12.4 | 2.8 |
| | Average | 3.7 | 6.3 | 3.2 |
| Wind Speed: | 1600 | 3.6 | 3.4 | 3.3 |
| | 1200 | 5.2 | 3.2 | 4.4 |
| | 900 | 5.3 | 2.7 | 4.4 |
| | 600 | 4.5 | 3.7 | 3.3 |
| | 300 | 2.8 | 7.7 | 1.9 |
| | 150 | 2.6 | 10.0 | 2.6 |
| | 50 | 2.7 | 11.5 | 3.2 |
| | Average | 3.8 | 6.0 | 3.3 |

Table 5. Mean "actual" values of u, v and wind speed (repeated from Table 2) compared with mean arithmetic (bias) errors of RAOB-derived standard geostrophic and modified Ekman wind data. A positive bias indicates that RAOB values are greater than "actual" values. Units are m s-1.

| | Level (m) | "Actual" Mean | RAOB-Geo Bias | RAOB-Ekman Bias |
|---|---|---|---|---|
| u-component: | 1600 | 1.9 | -1.5 | -1.4 |
| | 1200 | 0.8 | -0.1 | -1.0 |
| | 900 | 0.3 | 0.5 | -1.4 |
| | 600 | -1.2 | 2.1 | -1.1 |
| | 300 | -4.7 | 5.5 | 1.0 |
| | 150 | -5.3 | 6.1 | 1.2 |
| | 50 | -5.1 | 5.8 | 1.3 |
| | Average | -1.9 | 2.6 | -0.2 |
| v-component: | 1600 | 9.3 | 0.4 | 0.6 |
| | 1200 | 11.4 | 0.2 | -1.0 |
| | 900 | 12.3 | 0.8 | -1.7 |
| | 600 | 12.4 | 2.1 | -1.7 |
| | 300 | 10.2 | 5.8 | -0.4 |
| | 150 | 8.6 | 8.2 | 0.0 |
| | 50 | 7.6 | 9.9 | -0.1 |
| | Average | 10.3 | 3.9 | -0.6 |
| Wind Speed: | 1600 | 10.4 | 0.1 | 0.4 |
| | 1200 | 12.4 | -0.1 | -1.1 |
| | 900 | 13.2 | 0.6 | -1.6 |
| | 600 | 13.3 | 2.0 | -1.6 |
| | 300 | 12.1 | 4.8 | -0.8 |
| | 150 | 11.1 | 6.7 | -0.7 |
| | 50 | 10.1 | 8.3 | -0.8 |
| | Average | 11.8 | 3.2 | -0.9 |

Table 6. Correlation coefficients comparing "actual" wind fields with RAOB-derived standard geostrophic and modified Ekman winds. Linear correlations examine wind speeds, while vector values denote total wind comparisons.

| Linear Correlation Coefficient, r | | |
|---|---|---|
| Level (m) | "Actual"/R-Geo | "Actual"/R-Ekman |
| 1600 | 0.766 | 0.792 |
| 1200 | 0.873 | 0.764 |
| 900 | 0.926 | 0.804 |
| 600 | 0.937 | 0.888 |
| 300 | 0.821 | 0.931 |
| 150 | 0.693 | 0.845 |
| 50 | 0.696 | 0.786 |

| Vector Correlation Coefficient, R | | |
|---|---|---|
| Level (m) | "Actual"/R-Geo | "Actual"/R-Ekman |
| 1600 | 0.642 | 0.664 |
| 1200 | 0.789 | 0.694 |
| 900 | 0.859 | 0.763 |
| 600 | 0.877 | 0.850 |
| 300 | 0.837 | 0.882 |
| 150 | 0.763 | 0.833 |
| 50 | 0.744 | 0.801 |

however, one should recall that this component is relatively small and variable since the flow is mainly meridional. Standard deviations of the Ekman winds agree better with those of the "actual" data (Table 2) than do geostrophic values. Thus, the Ekman procedure better describes both vertical and horizontal variations in the observed flow than does the geostrophic technique.

Agreements between computed and observed winds can be investigated further using Table 4. Here, root-mean-square errors of the geostrophic and modified Ekman winds are compared with standard deviations of the "actual" data. Examination of vertically averaged RMS errors shows that the Ekman winds yield smaller values than do their geostrophic counterparts. The same relationship generally holds also for the horizontal means at the three levels below 900 m AGL. This pattern of Ekman winds yielding "better" statistical values than geostrophic winds in the lower levels will be reflected in other statistics to be examined as well. It is assumed to be due primarily to handling of frictional effects by the Ekman procedure. The standard geostrophic wind equations do not account for friction, thereby "degrading" winds in the lower levels. On the other hand, the Ekman scheme retains the effects of friction equally at all levels (through $K_m$), "degrading", to a slight degree, winds in the upper levels.

An important point is that Ekman winds have RMS errors which are almost always smaller than standard deviations of the "actual" wind data (Table 4). Conversely, geostrophic winds in the three lowest levels possess RMS errors that are considerably greater than the observed horizontal variability. The Ekman technique is thus considered the preferred method for computing PBL winds.

In Table 5, systematic errors of the two computational methods are examined by comparing mean arithmetic (bias) errors of the geostrophic and modified Ekman winds to mean values of the "actual" wind data. Comparison of the two righthand columns shows that a strong positive bias generally results from using the geostrophic approach. On the other hand, the Ekman method yields a much smaller negative bias. This can be seen particularly in the lower levels where, for example, "actual" wind speeds at 50 m AGL are overestimated by 8.3 m $s^{-1}$ using standard geostrophic equations, but are underestimated by less than 1.0 m $s^{-1}$ using the Ekman approach. Although both methods yield systematic errors that are smaller than observed means (except for u-components in the upper levels), the Ekman technique usually produces the least bias.

Finally, the correlation between the RAOB-derived wind sets and the "actual" wind fields is examined (Table 6). Two types of correlation coefficients have been employed. The

"product moment" formula for the linear correlation coefficient, $r$, is used to quantify a linear relationship between wind speeds of the two data sets. A second parameter, Court's total vector correlation coefficient, $R$, expands upon the simpler linear version by including a multiple correlation between vectors (Lambeth, 1966). This results in a statistic which relates two wind vectors that are separated in time, space, or both time and space. The mechanics of both statistics are presented in Appendix C.

Examination of the linear correlation coefficients (Table 6) shows that geostrophic wind speeds exhibit slightly better agreement with their "actual" counterparts in the midlevels than do the Ekman data. However, at 1600 m AGL and below 600 m AGL, the Ekman wind speeds are more highly correlated to the "actual" data, with linear values ranging from 0.786 at 50 m AGL to 0.931 at 300 m AGL. Similar results occur with the vector coefficients. From 600-1200 m AGL, the geostrophic winds show slightly better agreement with observed values than the Ekman fields (maximum vector value, 0.877). However, at 1600 m and below 600 m AGL, the Ekman winds are not only more highly correlated to the "actual" winds, but they exhibit the largest vector correlation coefficient of all levels (0.882 at 300 m AGL). A consideration here is that 300 m AGL is the level at which input data are most affected by low-level inversions (Fig. 6). Since inversion conditions more nearly reflect the

hydrostatically stable regime upon which the Ekman equations are based, data at 300 m AGL would be assumed to yield the most representative winds.

3) Validation

Qualitative comparisons (Figs. 15, 16 and 17) have shown that the modified Ekman technique, coupled with standard RAOB data, yields wind fields which agree very favorably to corresponding "actual" values. Furthermore, the statistical comparisons (Tables 3 through 6) indicate that the Ekman approach is not only well founded, but is preferred over the simpler geostrophic method. Best agreements between Ekman and observed winds occur near the surface. These comparisons establish the modified Ekman procedure with rawinsonde input as a standard against which to compare satellite-derived Ekman winds.

c. Satellite-derived modified Ekman winds

Fields of modified Ekman winds obtained from TIROS-N thermal data are presented in Fig. 18. The satellite-derived winds compare quite favorably to the "actual" wind fields in Fig. 15. As with the RAOB-derived Ekman winds, patterns exhibit more detail than the observed data by indicating the presence of the pressure ridge in the east and, in the upper levels, the trough just west of the grid. Mean values and standard deviations for

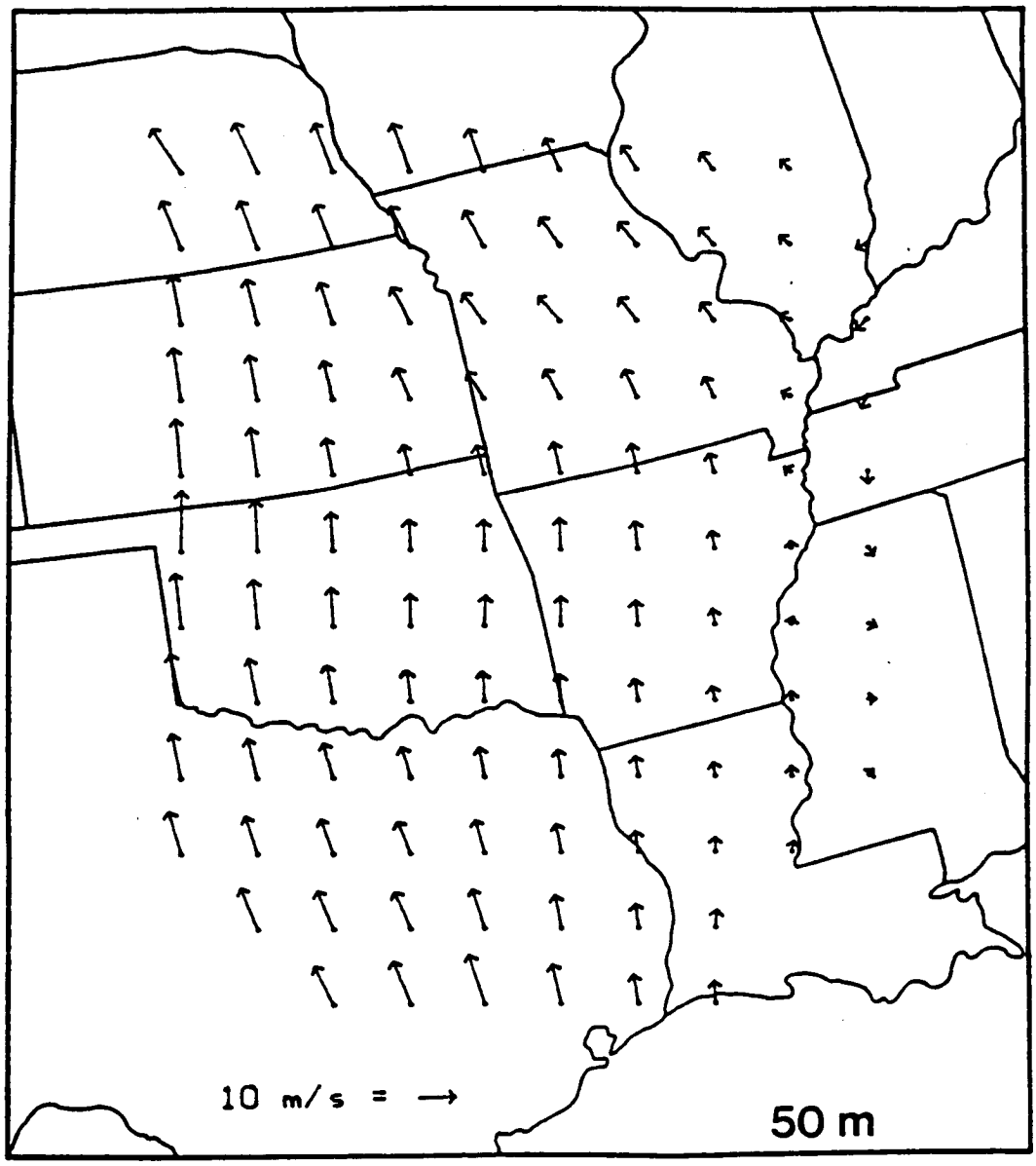


Fig. 18. Satellite-derived modified Ekman wind fields (m $s^{-1}$) at 50, 300 and 1200 m AGL.

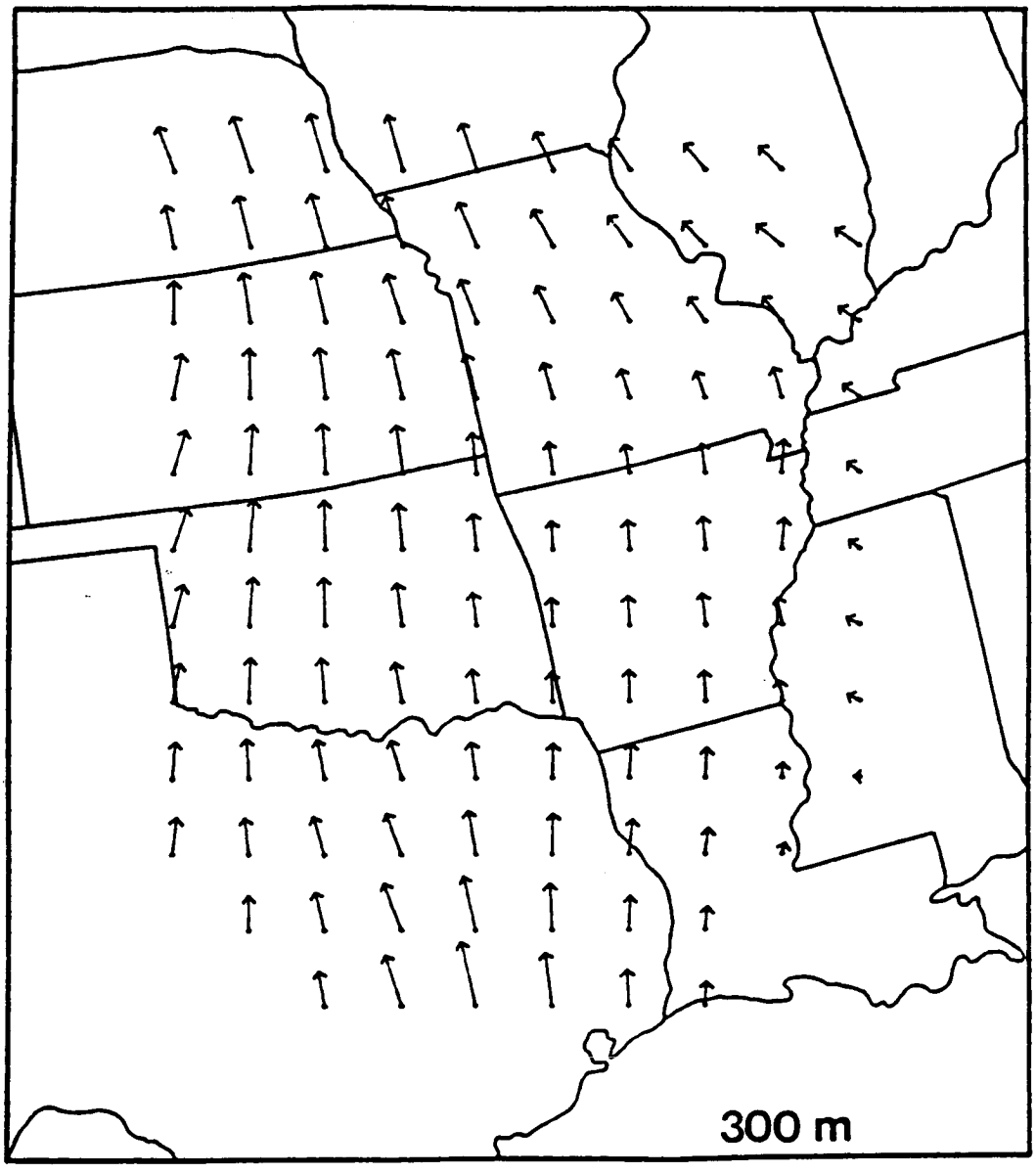


Fig. 18. Continued.

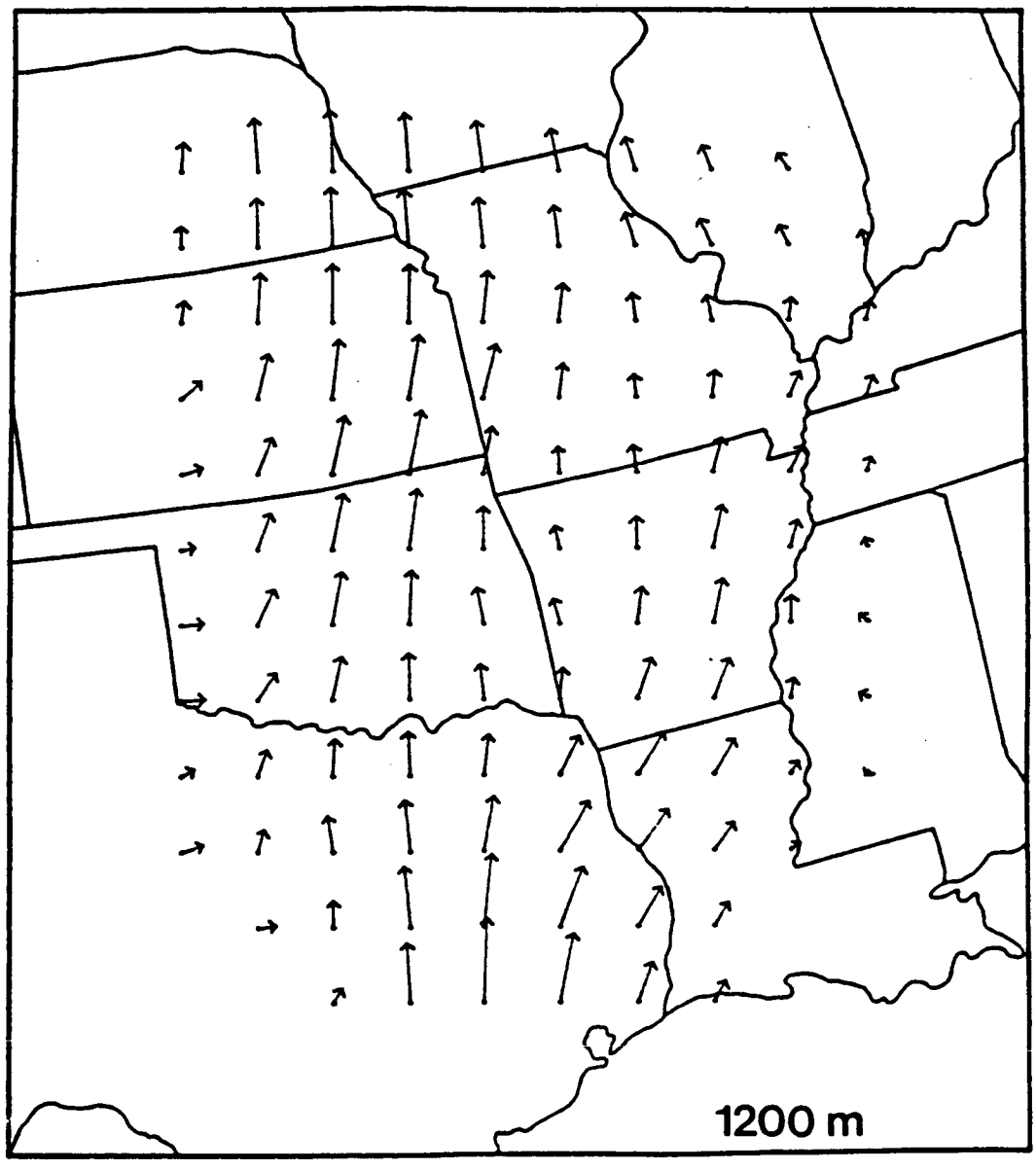


Fig. 18. Continued.

the satellite-derived u,v components and wind speeds are given in Table 7. Comparison with corresponding "actual" data in Table 2 identifies the satellite winds as having a more westerly (more negative "u") component above 300 m AGL. Vertical averages of the v-components show satellite-derived values to be $\sim$1.7 m $s^{-1}$ less than the observed data, resulting in mean wind speeds 1.8 m $s^{-1}$ slower than "actual" winds. The greatest mean speeds again occur at 600 m AGL. Vertical averages of the standard deviations are quite similar, with the maximum difference at an individual level being 1.3 m $s^{-1}$.

A qualitative comparison of the RAOB- and satellite-derived modified Ekman winds (Figs. 17 and 18, respectively) indicates a very good correspondence, particularly in the lowest levels. Statistical comparisons between mean values in Tables 3 and 7 show satellite Ekman winds have a slightly stronger u-component and are $\sim$0.9 m $s^{-1}$ weaker than RAOB winds. Standard deviations indicate a somewhat greater degree of variability in the satellite data, with differences in RAOB-derived values being less than 1.6 m $s^{-1}$ at any given level.

Root-mean-square errors between the satellite-derived and "actual" wind fields are given in Table 8. Comparisons with the two righthand columns of Table 4 show that near the surface and in the vertical average the satellite errors are between corresponding statistics for the RAOB-derived geostrophic and

Table 7. Same as Table 2, except for satellite-derived modified Ekman winds.

| | Level (m) | Mean | σ |
|---|---|---|---|
| u-component: | 1600 | 0.1 | 2.7 |
| | 1200 | -0.7 | 2.8 |
| | 900 | -1.2 | 3.0 |
| | 600 | -2.7 | 2.9 |
| | 300 | -3.8 | 2.5 |
| | 150 | -4.0 | 2.1 |
| | 50 | -3.7 | 2.3 |
| | Average | -2.3 | 2.6 |
| v-component: | 1600 | 8.6 | 5.1 |
| | 1200 | 9.2 | 4.7 |
| | 900 | 9.6 | 4.3 |
| | 600 | 9.6 | 3.6 |
| | 300 | 8.7 | 3.4 |
| | 150 | 7.7 | 3.8 |
| | 50 | 6.8 | 4.1 |
| | Average | 8.6 | 4.1 |
| Wind Speed: | 1600 | 9.8 | 4.5 |
| | 1200 | 10.3 | 4.3 |
| | 900 | 10.7 | 4.0 |
| | 600 | 10.9 | 3.5 |
| | 300 | 10.4 | 3.0 |
| | 150 | 9.5 | 3.3 |
| | 50 | 8.7 | 3.7 |
| | Average | 10.0 | 3.8 |

Table 8. Root-mean-square errors and mean arithmetic (bias) errors of satellite-derived modified Ekman winds (m $s^{-1}$).

| | Level (m) | SAT-Ekman RMSE | SAT-Ekman Bias |
|---|---|---|---|
| u-component: | 1600 | 4.3 | -1.9 |
| | 1200 | 4.3 | -1.5 |
| | 900 | 4.3 | -1.9 |
| | 600 | 3.7 | -1.5 |
| | 300 | 2.8 | 0.9 |
| | 150 | 3.4 | 1.4 |
| | 50 | 3.9 | 1.5 |
| | Average | 3.8 | -0.4 |
| v-component: | 1600 | 5.0 | -0.6 |
| | 1200 | 5.8 | -2.2 |
| | 900 | 5.8 | -2.8 |
| | 600 | 4.9 | -2.9 |
| | 300 | 3.0 | -1.6 |
| | 150 | 2.8 | -1.0 |
| | 50 | 2.8 | -0.7 |
| | Average | 4.3 | -1.7 |
| Wind Speed: | 1600 | 4.6 | -0.6 |
| | 1200 | 5.6 | -2.1 |
| | 900 | 5.6 | -2.5 |
| | 600 | 4.6 | -2.4 |
| | 300 | 3.0 | -1.7 |
| | 150 | 3.2 | -1.6 |
| | 50 | 3.3 | -1.3 |
| | Average | 4.3 | -1.7 |

modified Ekman winds. Furthermore, satellite values at individual levels are no more than 1.6 m $s^{-1}$ greater than those for the RAOB Ekman winds. Smallest satellite-derived RMS errors occur in the lower levels, particularly at 300 m AGL. The satellite-derived Ekman winds have RMS errors that are slightly greater than the standard deviations of the "actual" wind data (Table 2).

Mean arithmetic errors of the satellite Ekman winds are also presented in Table 8. Comparison with corresponding RAOB-derived errors in Table 5 reveals a similar pattern of negative biases for u-components above 300 m AGL, and v-components and winds speeds at nearly all levels. Although vertical averages of satellite bias errors are slightly greater than those for RAOB Ekman winds, they are significantly smaller than those of corresponding RAOB-derived geostrophic values. Furthermore, these bias errors are significantly smaller than the degree of natural variability seen in the "actual" wind data (Table 2).

Correlation coefficients relating the satellite Ekman fields to observed winds are presented in the center column of Table 9. Values of the linear coefficient show that satellite-derived wind speeds are most highly correlated to their "actual" counterparts in the lower levels in general, and at 300 m AGL in particular (where $r$ equals 0.844). This pat-

Table 9. Same as Table 6, except comparing satellite-derived modified Ekman winds with "actual" and RAOB-derived modified Ekman wind fields.

| Linear Correlation Coefficient, r | | |
|---|---|---|
| Level (m) | "Actual"/S-Ekman | R-Ekman/S-Ekman |
| 1600 | 0.627 | 0.842 |
| 1200 | 0.632 | 0.857 |
| 900 | 0.662 | 0.870 |
| 600 | 0.746 | 0.890 |
| 300 | 0.844 | 0.921 |
| 150 | 0.795 | 0.941 |
| 50 | 0.757 | 0.979 |

| Vector Correlation Coefficient, R | | |
|---|---|---|
| Level (m) | "Actual"/S-Ekman | R-Ekman/S-Ekman |
| 1600 | 0.334 | 0.725 |
| 1200 | 0.401 | 0.751 |
| 900 | 0.498 | 0.768 |
| 600 | 0.597 | 0.784 |
| 300 | 0.718 | 0.828 |
| 150 | 0.735 | 0.893 |
| 50 | 0.749 | 0.957 |

tern is similar to that shown by the RAOB-derived coefficients in Table 6. Satellite values are slightly lower than those obtained using RAOB Ekman data, yet remain significantly high at all levels.

The added effect of wind direction is evaluated by the vector correlation coefficients given in the lower center column of Table 9. Note that values below 600 m are quite high. In the upper levels, values of $R$ indicate, at first glance, a disturbingly low correlation between satellite-derived and "actual" winds. Investigation of this discrepancy revealed that the problem lies primarily in comparing two "total" wind fields which differ significantly in the "smoothness" of their flow patterns. As noted previously, "actual" fields are based on 26 observations, while RAOB and satellite grids are derived from 39 and 62 soundings, respectively. The increased amount of detail available from the larger RAOB and satellite data bases has been shown to be most evident along the eastern and western borders of the grid area. Values of $R$ which do not consider these border gridpoints reveal a much higher correlation between satellite-derived and observed winds, raising the lowest value (at 1600 m AGL) from 0.334 to over 0.620.

This problem is not as obvious in the RAOB-derived $R$-values of Table 6. Superimposing the three types of fields

("actual", RAOB and satellite) at any given upper level reveals that RAOB-derived vectors generally lie between those of corresponding satellite-derived and observed winds. Figure 19 shows, for example, fields at 1600 m AGL. In other words, satellite and RAOB vectors exhibit a similar amount of detail (Figs. 17 and 18); however, RAOB winds show less directional (and speed) departures from observed vectors than do satellite winds.

A more appropriate statistical test of the significance of satellite-derived PBL winds, then, is to compare them directly with their (more equally detailed) RAOB counterparts. The righthand column of Table 9 gives the results of such a comparison. Immediately, we see the very high correlation between wind speeds at all levels, ranging from an $r$-value of 0.979 at 50 m AGL to 0.842 at 1600 m AGL. A similar pattern is seen in the values of $R$, which range from 0.957 to 0.725 at 50 m and 1600 m AGL, respectively. The slight decrease in correlation with height probably occurs because the satellite winds retain (with increasing altitude) the light and variable pattern along the eastern border of the grid, whereas the RAOB winds yield stronger and more southerly vectors at the higher levels. This may be a result of the denser satellite coverage (recall Figs. 3 and 4) in the area of the high pressure ridge.

Synoptic-scale PBL winds computed using satellite-derived

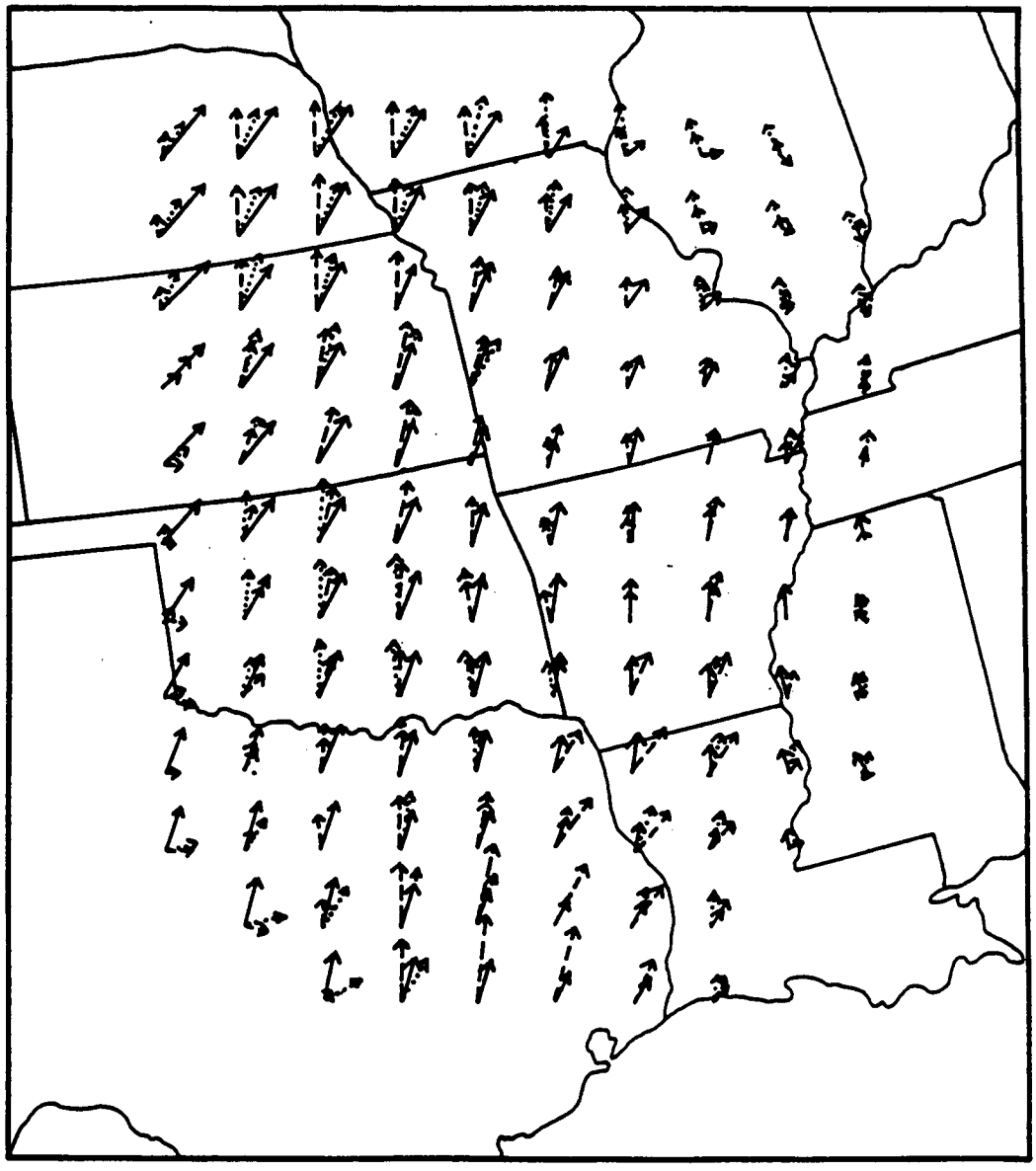

Fig. 19. "Actual" (solid), RAOB (dotted) and satellite (dashed) wind vectors at 1600 m AGL superimposed.

temperatures have thus been shown to be very comparable to winds obtained in a similar manner using RAOB thermal data. Overall, the most favorable comparisons, both qualitative and statistical, are at 300 m AGL (the average height of the numerous inversions). Satellite winds tend to be slightly weaker and exhibit more cross-isobaric flow. Both RAOB and satellite modified Ekman winds reproduce the general flow pattern of the observed fields; given a denser observed data base, however, much higher correlation to "actual" winds is anticipated.

d. Sensitivity analysis

The sensitivity of three parameters which variously affect nearly all terms in the modified Ekman equations is investigated in this section. Variations in the height of the surface layer/transition layer interface are examined first. Second, the preference for a horizontally variable, rather than a constant, $K_m$ is discussed. Finally, the ability of the computational scheme to handle random error in satellite-derived temperature data is explored.

Ekman winds are quite sensitive to the appropriate selection of the depth of the surface layer because $h$ determines, in part, the values of $S$, $K_m$, $\vartheta_*$ and the modified geostrophic wind components at $z = h$ ($u_g^h$ and $v_g^h$). To evaluate this dependence,

fields of both RAOB- and satellite-derived modified Ekman winds were computed using values of $h$ ranging from 0 to 125 m AGL. Six values, at 25 m intervals, were used in all. For $h = 0$, a constant flux layer was not considered to exist, and $K_m$ was set equal to its classic value of 1.0 $m^2$ $s^{-1}$. Standard deviations of differences between "actual" winds and the RAOB and satellite Ekman fields were computed, along with corresponding linear correlation coefficients. Statistical results for wind speed are presented in Figs. 20 and 21. Recall that Gerrity's empirical model sets $h$ equal to 50 m; this value is supported by the RAOB data (Fig. 20), yielding overall the smallest standard deviations and highest correlations. Closer agreement between "actual" and satellite-derived winds can be achieved by setting $h$ equal to 75 m as indicated in the results displayed in Fig. 21. However, the 25 m increase in the depth of the surface layer produces "smoother" fields of satellite winds, which are more compatible with the observed data. This suggestion of a higher value for $h$ is thus considered to stem from the same problem of differing degrees of detail outlined in the previous section. The value of 50 m, therefore, is deemed optimum for $h$.

The second parameter under discussion is $K_m$. Recall from Chapter 2 that $K_m$ is regarded as a function of height in the surface layer. Within the transition layer, however, the Ekman approach assumes the eddy viscosity to be equal to its value at

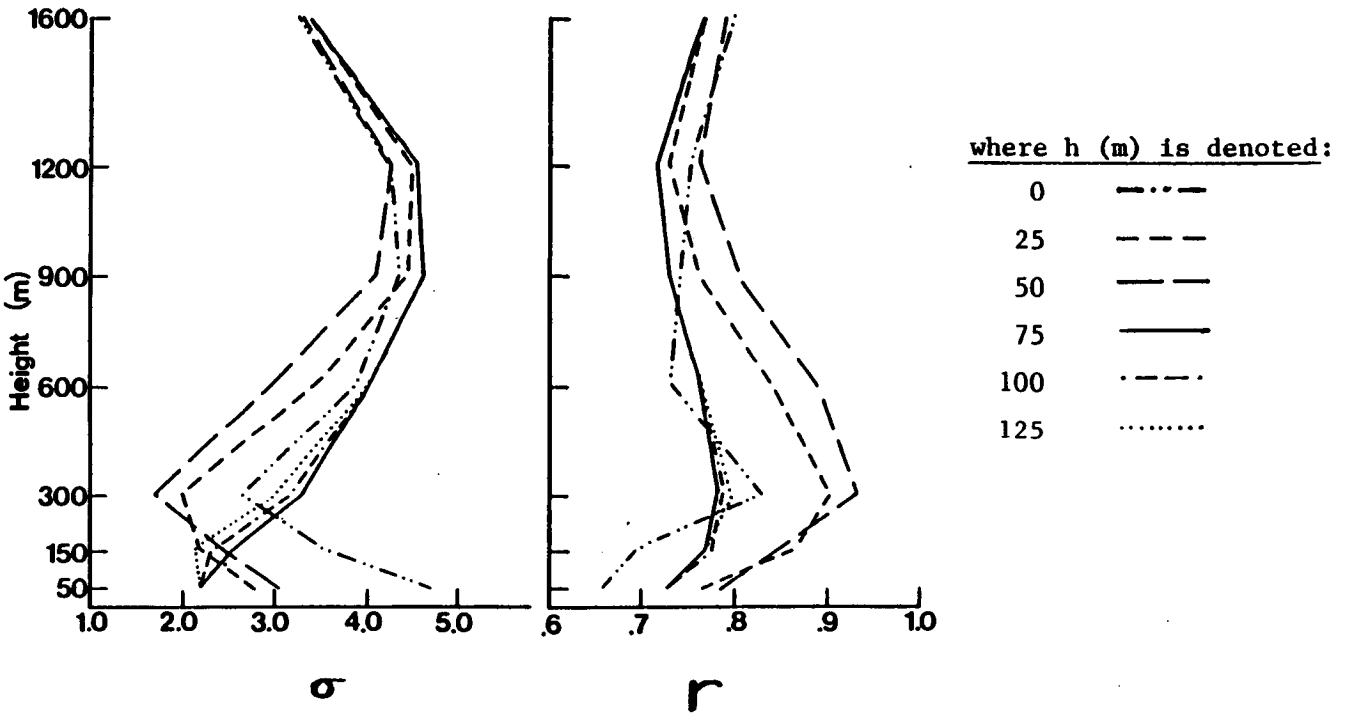


Fig. 20 Vertical profiles of standard deviations (m $s^{-1}$) of the differences between "actual" wind speeds and RAOB-derived modified Ekman wind speeds based on varying values of $h$ (left graph). Corresponding linear correlation coefficients are shown in the right graph.

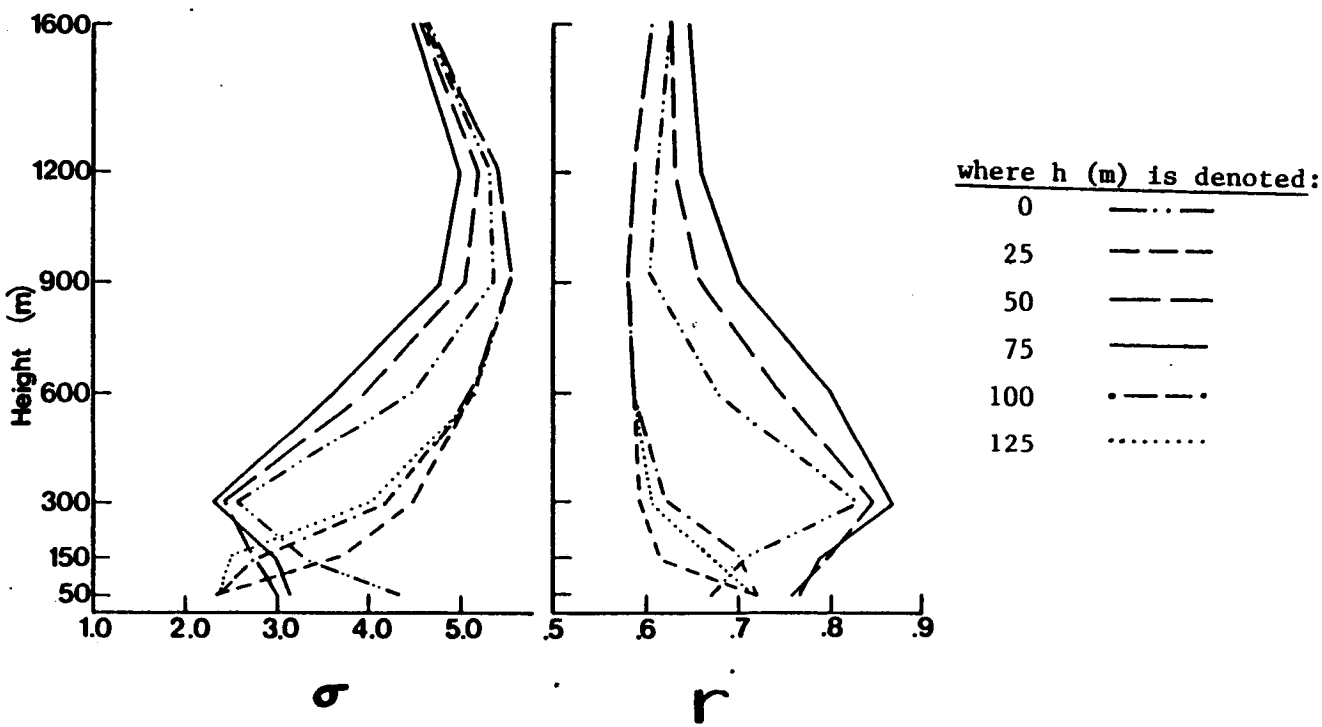


Fig. 21. Same as Fig. 20, except using satellite-derived modified Ekman wind speeds.

$z = h$ and independent of altitude. In the current scheme, $K_m$ is computed separately at each gridpoint in the plane $z' = h$. Holton (1979) and Hess (1959) both note a mean value of $\sim 5.0$ $m^2$ $s^{-1}$ for $K_m$ in a stable boundary layer 1 km in depth.

Holton's expression relating $K_m$ to the depth of the Ekman layer yields 13.0 $m^2$ $s^{-1}$ for the current boundary layer which extends to 1600 m AGL. Richardson numbers computed for the present case indicate forced convective, though nearly stable, conditions exist throughout the surface layer; thus, a similar or slightly higher mean value for the turbulent exchange coefficient should be anticipated (see Appendix E for baroclinic effects). Indeed, RAOB data yield a mean of 13.1 $m^2$ $s^{-1}$, while the average satellite-derived value of $K_m$ is 13.6 $m^2$ $s^{-1}$. Horizontal depictions of the RAOB- and satellite-generated values of $K_m$ are shown in Figs. 22 and 23, respectively. Note that higher values (indicating greater instability) are located in the western halves of both areas, while smallest values are in the vicinity of the eastern pressure ridge.

Assigning an appropriate mean value to $K_m$ would simplify the computational procedure appreciably. A test of the significance of using individually computed turbulent exchange coefficients, rather than a mean value, was therefore indicated. Fields of modified Ekman winds were computed using a constant (mean) $K_m$ set, variously, at 1.0, 5.0, 10.0, and 15.0 $m^2$ $s^{-1}$.

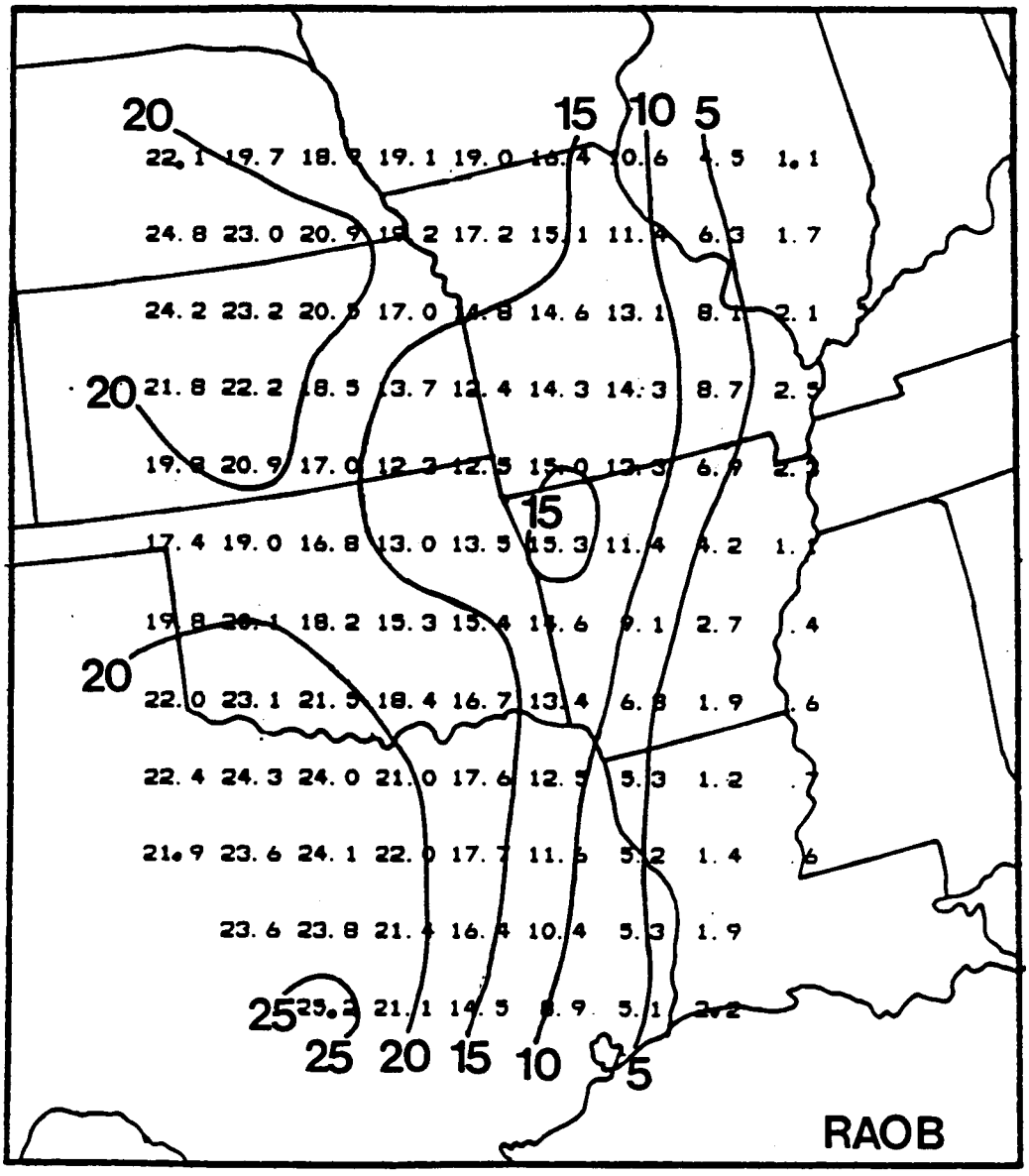


Fig. 22. RAOB-generated values of $K_m$ ($m^2$ $s^{-1}$).

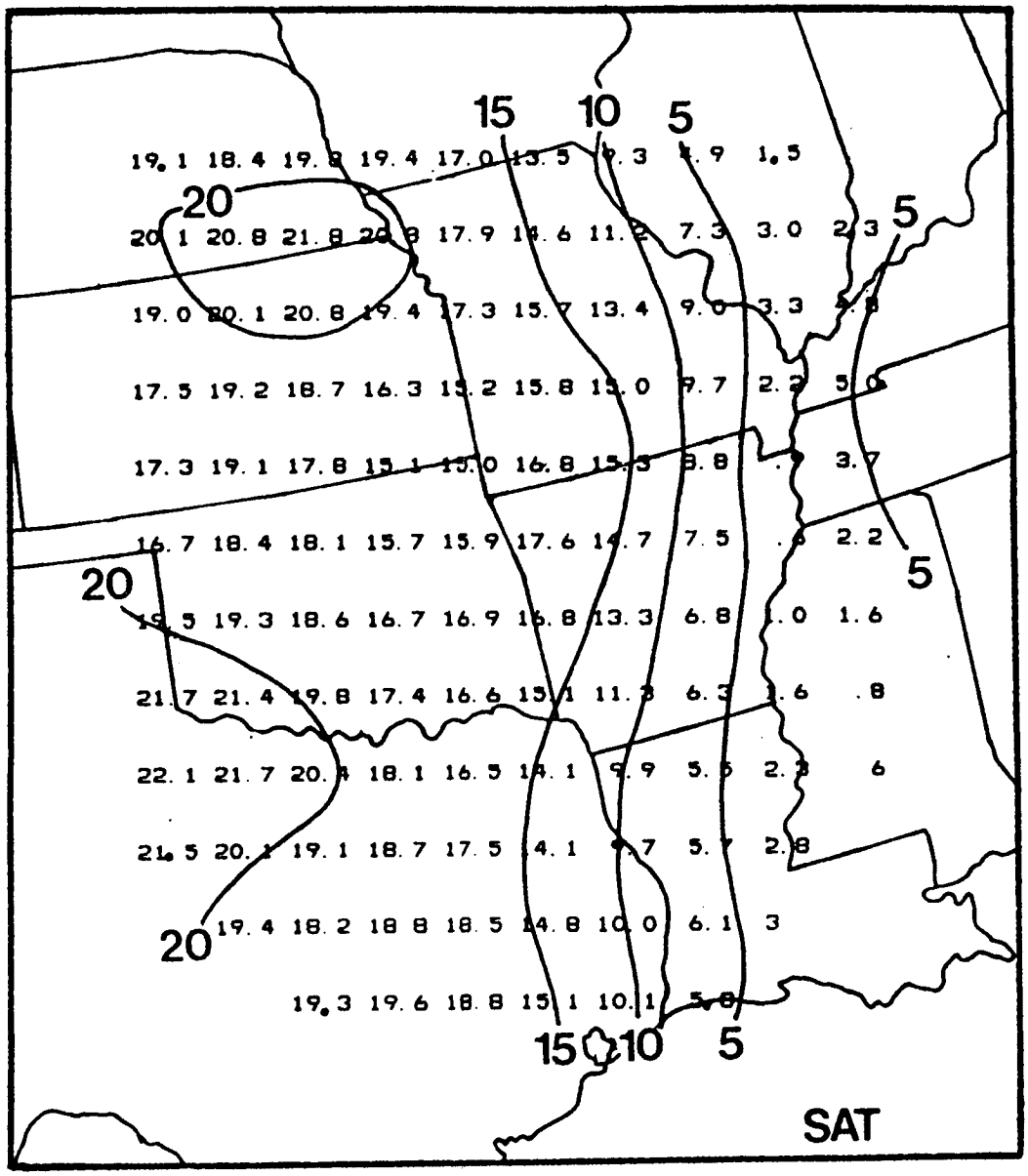


Fig. 23. Satellite-generated values of $K_m$ ($m^2$ $s^{-1}$).

Standard deviations of differences between these and "actual" fields were compared to previously derived statistics relating the "variable $K_m$" Ekman fields to the observed data. Corresponding linear correlation coefficients were also calculated. Results of these comparisons, again represented by the statistics for wind speed, are shown in Figs. 24 and 25 for RAOB and satellite data, respectively. Comparisons involving winds based on the "variable $K_m$" approach yield lower standard deviations and a higher degree of correlation. Of the constant values investigated, 15.0 $m^2$ $s^{-1}$ produced the closest agreement to fields derived from a variable $K_m$. Although use of 15.0 $m^2$ $s^{-1}$ would provide comparable results at 600 m and 900 m AGL for both data sets, an even higher mean value would be needed to produce the variable $K_m$ pattern from 50-300 m AGL and above 900 m AGL. Use of a (horizontally) variable $K_m$ is thus indicated as the preferred technique.

Finally, the ability of the computational scheme to handle errors in satellite thermal data is investigated. Recall from Chapter 4 (Section a) that the majority of past studies documenting these errors have presented comparison statistics which relate differences between corresponding RAOB and satellite soundings. A RMS error of 1.3°C is representative of such studies near the surface (Bruce et al., 1977; Smith et al., 1978; Schlatter, 1980; Scoggins et al., 1981). Also noted was a random error (or noise level) value of 0.5°C for satellite-derived

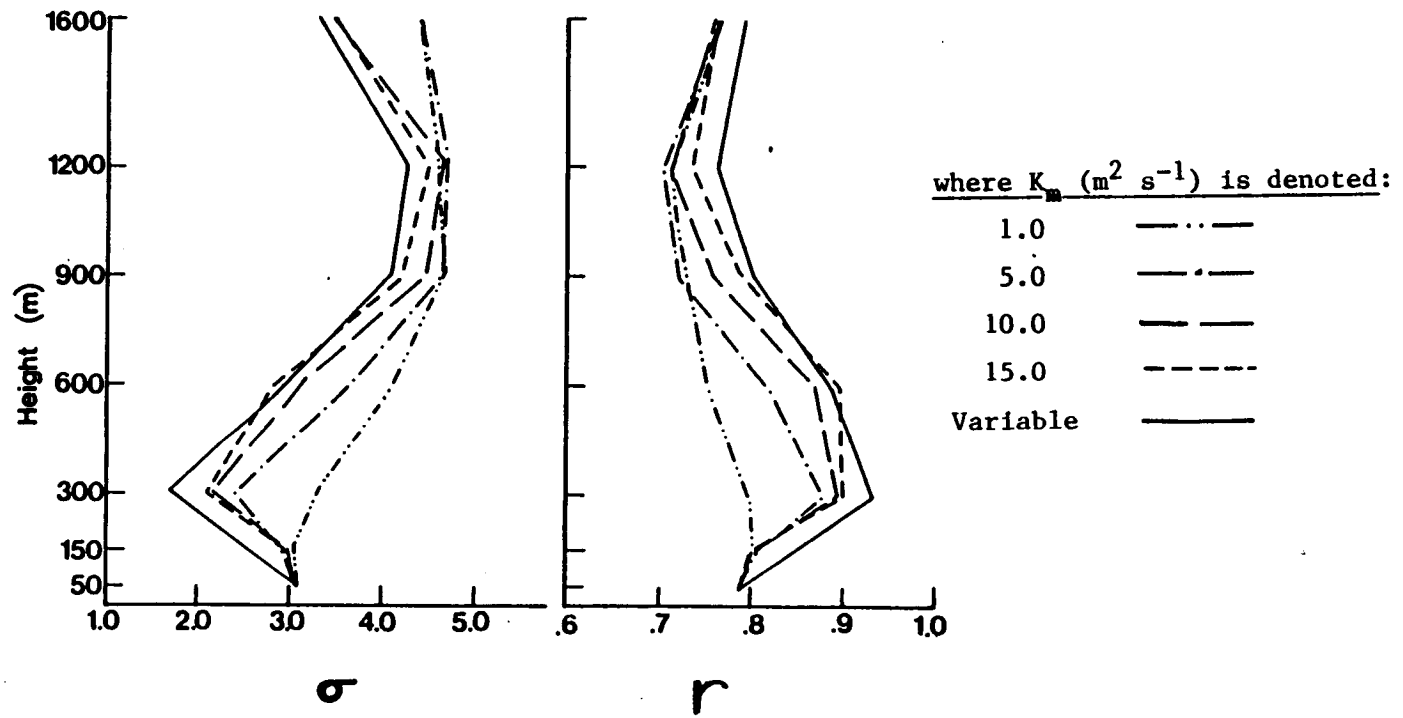


Fig. 24. Vertical profiles of standard deviations (m $s^{-1}$) of the differences between "actual" wind speeds and RAOB-derived modified Ekman wind speeds based on varying values of $K_m$ (left graph). Corresponding linear correlation coefficients are shown in the right graph.

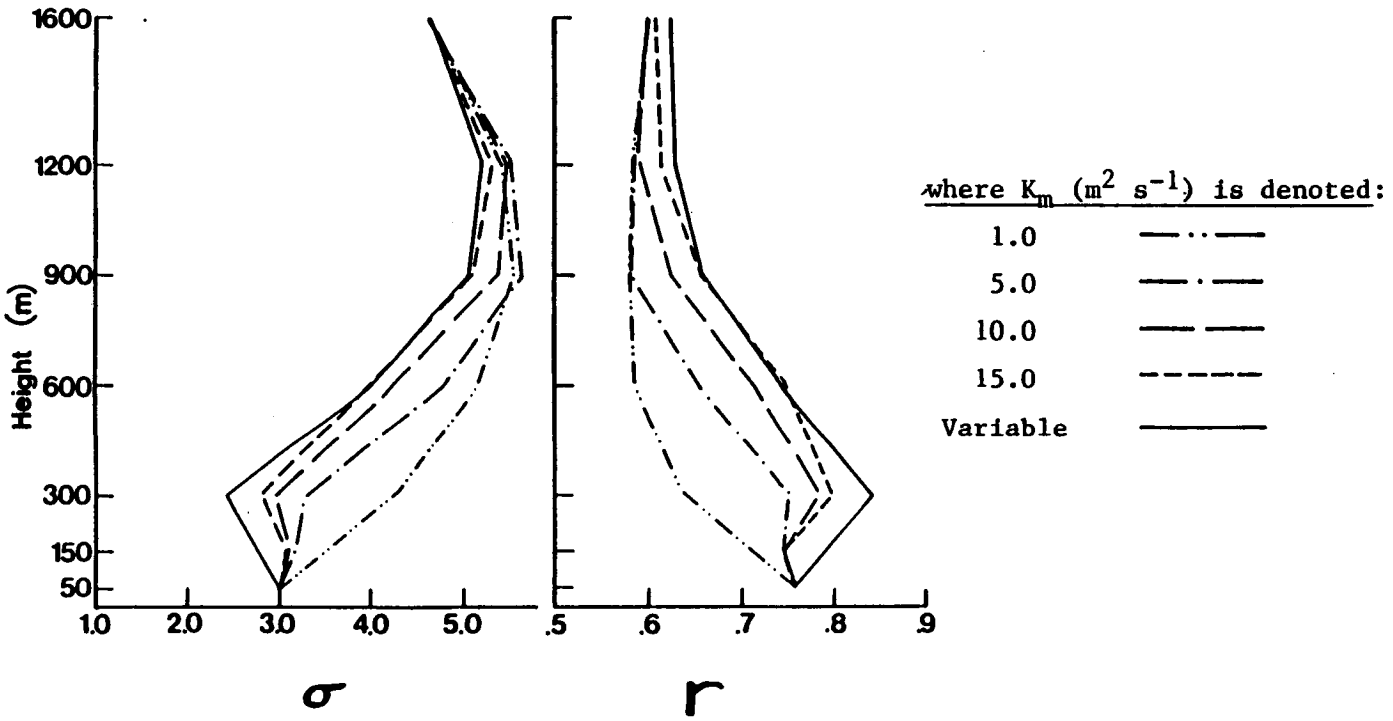


Fig. 25. Same as Fig. 24, except using satellite-derived modified Ekman wind speeds.

temperatures alone, documented by Hillger and Vonder Haar (1979) using structure function techniques.

A test to determine the effects of these errors on the resulting wind fields was performed in the following manner. The original TIROS-N thermal data were perturbed using computer-generated random errors which were normally distributed about zero. Five sets of perturbed satellite temperatures were based on a standard deviation of 1.3°C and another five on 0.5°C. (Degree of cloud combination at a given sounding was not considered.) Each of the ten perturbed data sets exhibited a different combination of errors. As with the original TIROS-N temperatures, these various data sets were then objectively analyzed using the Barnes (1973) scheme. Standard deviations of differences between the (objectively analyzed) original and perturbed thermal data are depicted in the upper half of Fig. 26. Note that in all cases, standard deviations of differences between the gridded data are less than 50% of the deviations originally introduced at the sounding sites.

Modified Ekman winds computed using the ten perturbed data sets then were compared to the unperturbed satellite-derived wind fields. Standard deviations of differences in wind speed are given in the lower half of Fig. 26. Winds below 600 m AGL were most affected by the deliberately perturbed temperature data, with greatest deviations near the surface. At 50 m AGL,

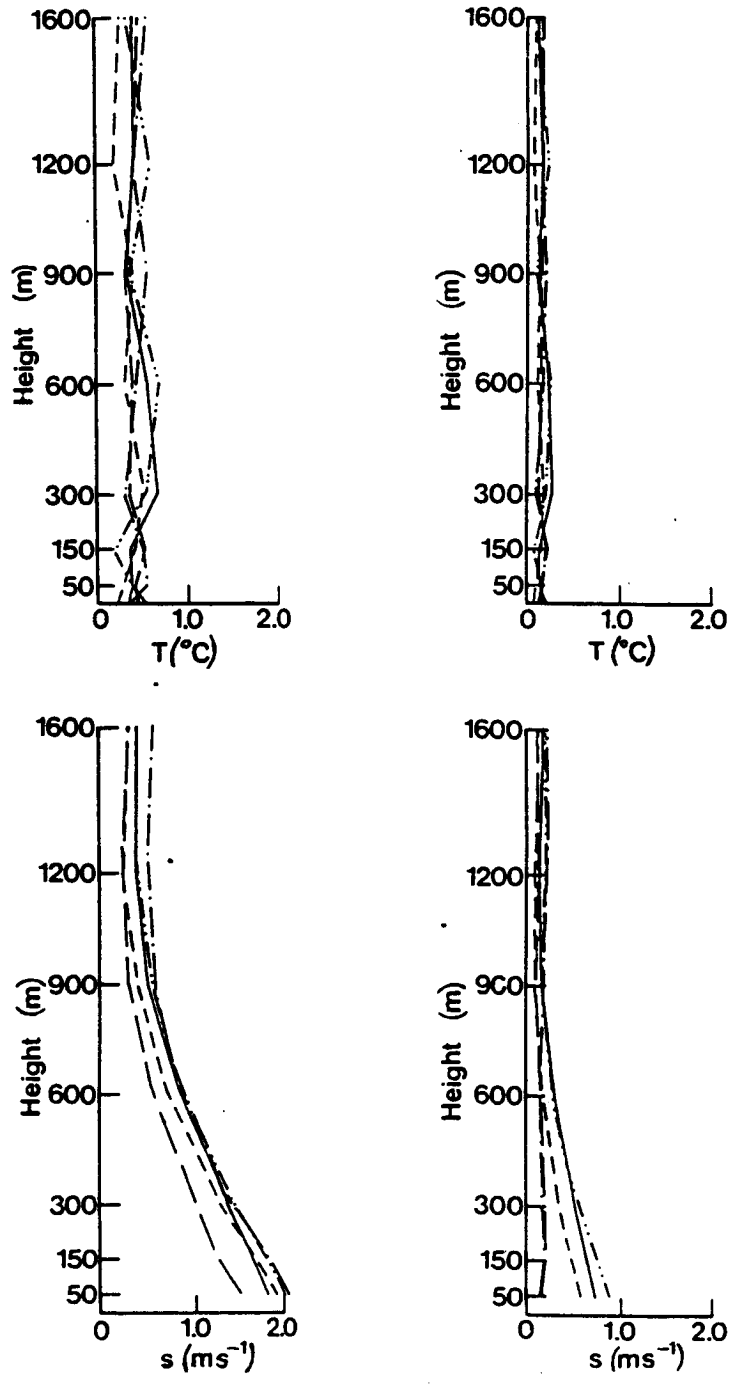


Fig. 26. Vertical profiles of standard deviations of the differences between original and perturbed TIROS-N thermal data (°C) (upper graphs) and their resulting modified Ekman wind speeds (m $s^{-1}$) (lower graphs). Statistics based on input random temperature errors of 1.3 and 0.5°C are shown on the lefthand and righthand graphs, respectively.

a 1.3°C error in the input temperature field yielded a difference as great as 2.2 m $s^{-1}$ from winds speeds based on unperturbed satellite data. Assuming a 0.5°C error, on the other hand, resulted in maximum differences of less than 0.9 m $s^{-1}$ at 50 m AGL and less than 0.3 m $s^{-1}$ above 600 m AGL.

The sensitivity study indicates that the objective analysis scheme filters approximately half of the random error present in satellite temperature data. Of the two values tested, 0.5°C is considered to be more representative since it was deduced from satellite data alone. Thus, variations in wind speeds attributable to random temperature errors are expected to be less than 0.9 m $s^{-1}$ near the surface and 0.3 m $s^{-1}$ in the upper half of the PBL.

e. Kinematic parameters

Results of Sections b and c indicate that the "best" RAOB- and satellite-derived modified Ekman winds occur at 300 m AGL. Four kinematic parameters were computed from data at this level: horizontal moisture divergence, moisture advection, velocity divergence, and relative vorticity. A fifth parameter, vertical motion, was determined at the top of the PBL using step-wise integration through the model levels below.

Fields of horizontal moisture divergence were computed in three ways. First, a "control" data set was obtained using

RAOB-derived modified Ekman winds and mixing ratios generated from RAOB dewpoint temperatures. A second set was computed using corresponding satellite-derived modified Ekman winds and mixing ratios. Finally, as a test of the TIROS-N moisture data, a third set was obtained by combining satellite Ekman winds with RAOB-derived mixing ratios. The first two pairs of fields are shown in Fig. 27. The combination of satellite winds with RAOB mixing ratios yielded patterns (not shown) nearly identical to those generated strictly from satellite data; differences were only $\pm 0.1 \times 10^{-5}$ g kg$^{-1}$ s$^{-1}$. This indicates that, for this particular synoptic situation, horizontal gradients of satellite-derived mixing ratios are comparable to their RAOB counterparts in the lower portion of the PBL.

The fields shown in Fig. 27 exhibit very similar features. Centers of moisture convergence (negative values) are located along the western and eastern borders of both areas, while moisture divergence is evident through the central section. Negri and Vonder Haar (1980) noted that moisture convergence $\geq 10^{-3}$ g kg$^{-1}$ s$^{-1}$ was favorable for severe convective activity in their study utilizing mesoscale cloud-tracked winds. In the current case, however, maximum values of both RAOB- and satellite-derived moisture convergence are approximately $10^{-4}$ g kg$^{-1}$ s$^{-1}$ (western centers). Larger values were not expected as the data are synoptic-scale in nature and indicate, overall, weak dynamic forcing at this predawn period (Fig. 5).

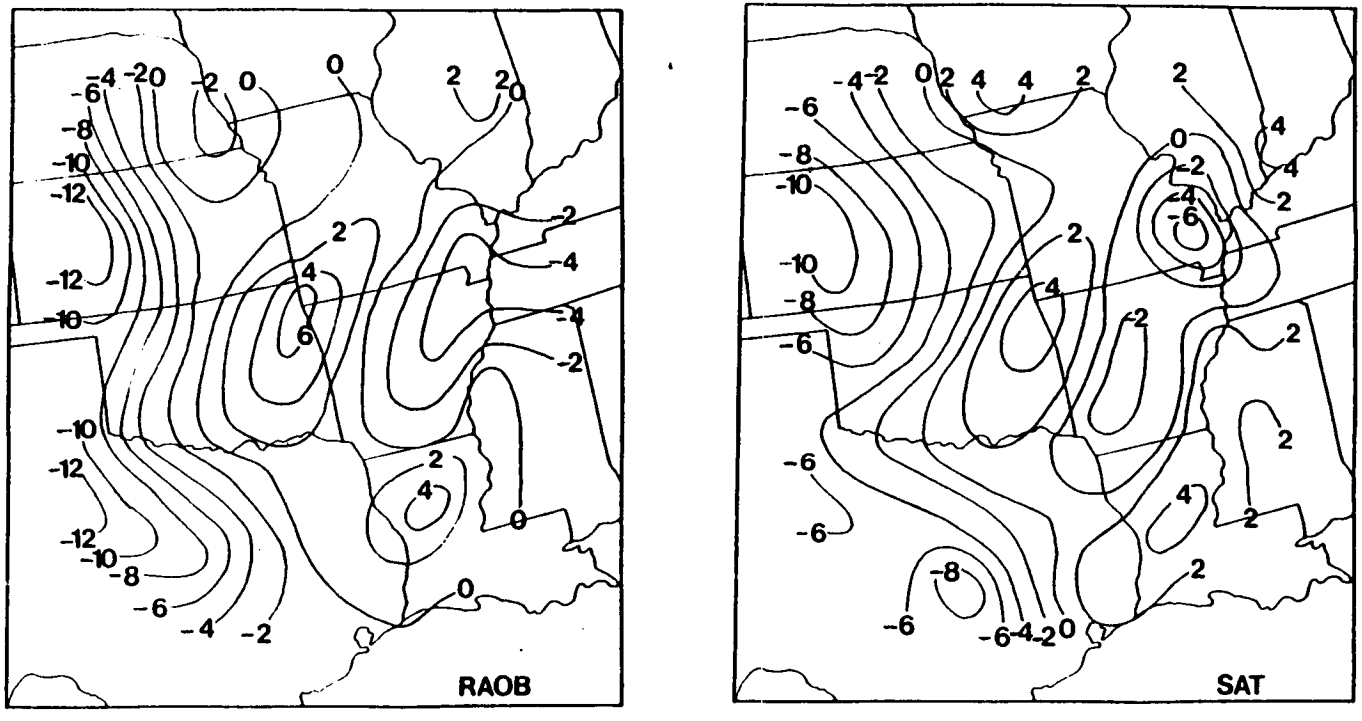


(a) (b)

Fig. 27. Fields of horizontal moisture divergence ($10^{-4}$ g $kg^{-1}$ $s^{-1}$) generated from (a) RAOB- and (b) satellite-derived modified Ekman winds and moisture data at 300 m AGL.

Radar summaries issued later in the day (Fig. 28) show that areas of moisture convergence agree closely with the intense convection which occurred in the region. Activity in northeastern Arkansas and the Missouri "bootheel" (Fig. 28, 1135 to 1735 GMT) corresponds to centers of moisture convergence obtained from both sounding data sources (Fig. 27). Similarly, convective cells in southcentral Texas (already formed at 1135 GMT) occur in regions of convergence. Further, weather watch boxes issued in the afternoon for the region extending from Nebraska to the Texas Panhandle correspond particularly well to areas of both RAOB and satellite moisture convergence. It is noteworthy that the greatest moisture convergence based on satellite (as well as RAOB) data coincide with the strongest convective cells which developed in central Kansas by 2235 GMT.

To further investigate the moisture divergence patterns, fields of its two components ($w(\vec{\nabla}_2 \cdot \vec{V}_2)$ and $\vec{V}_2 \cdot (\vec{\nabla}_2 w)$) were computed. Values for $\vec{V}_2 \cdot (\vec{\nabla}_2 w)$ (Fig. 29) were generally two orders of magnitude smaller than those for $w(\vec{\nabla}_2 \cdot \vec{V}_2)$ (not shown, but similar to Fig. 27). Patterns of moisture advection at 300 m AGL show similar features for both satellite and RAOB data. Positive advection (recall sign convention of (5-8)) predominates in the western half of the area, with greatest values over Oklahoma ($\sim 0.023 \times 10^{-4}$ g kg$^{-1}$ s$^{-1}$). Negative moisture advection occurs along the extreme western and eastern edges of

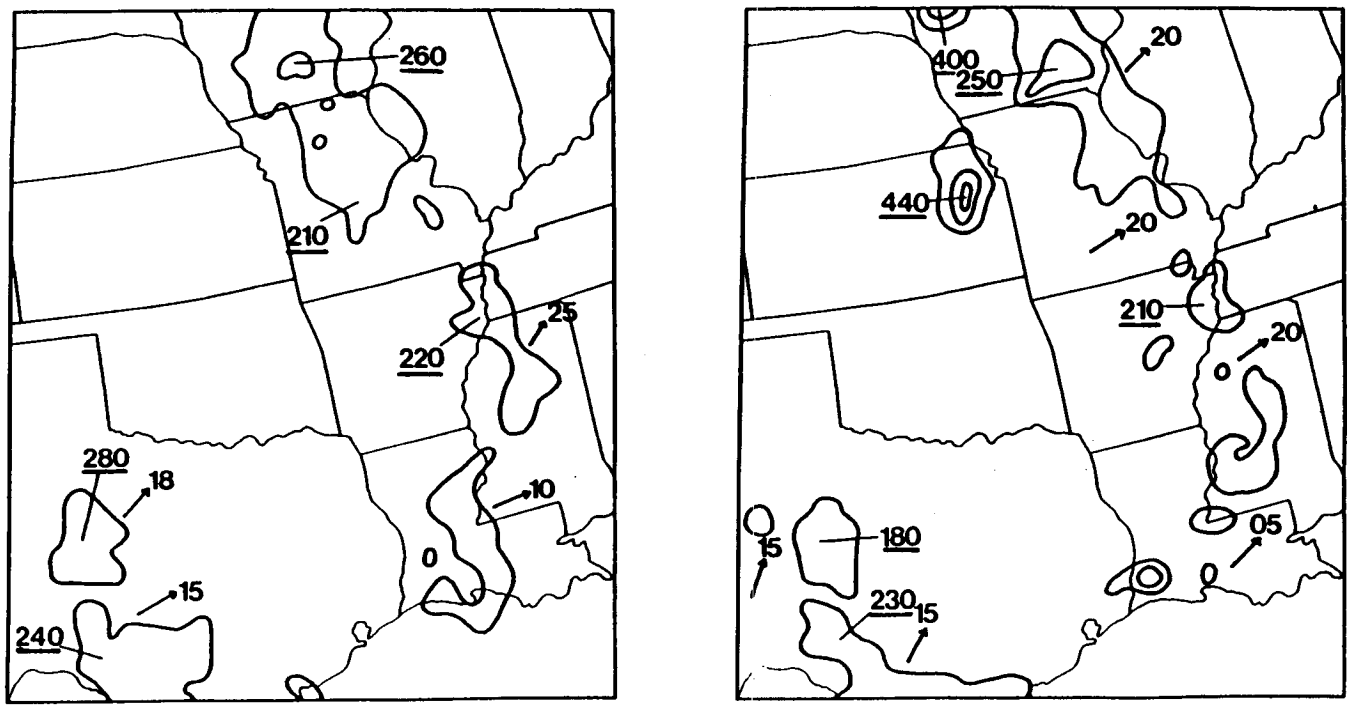


1135 GMT

1435 GMT

Fig. 28. Radar summaries for 1135, 1435, 1735, 1935, 2035 and 2235 GMT 19 April 1979.

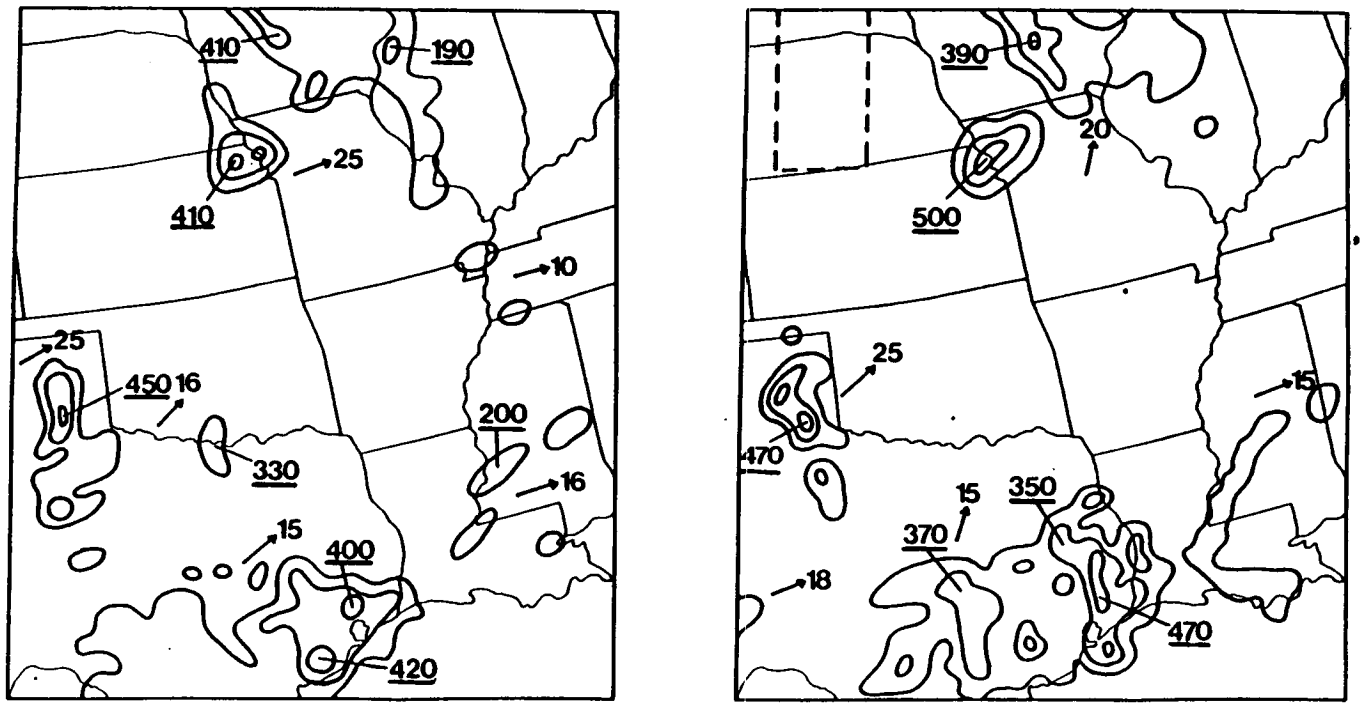


1735 GMT

1935 GMT

Fig. 28. Continued.

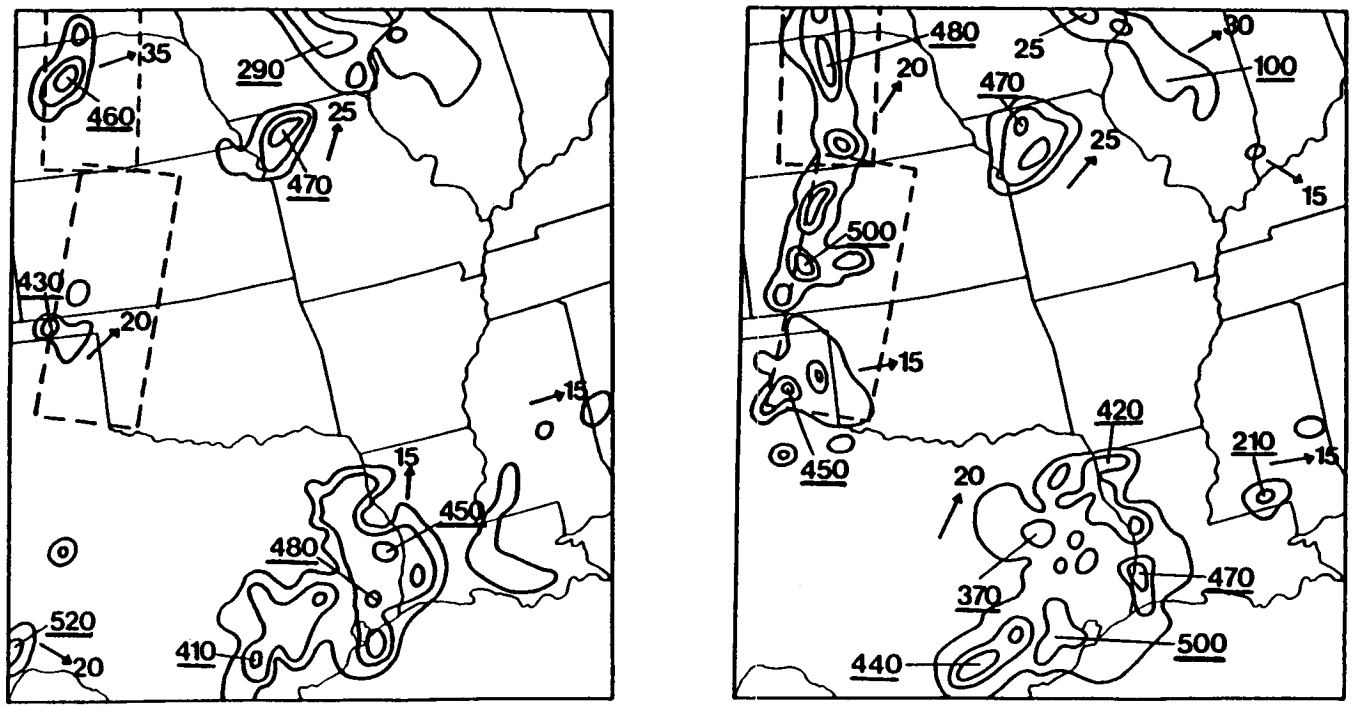


2035 GMT

2235 GMT

Fig. 28. Continued.

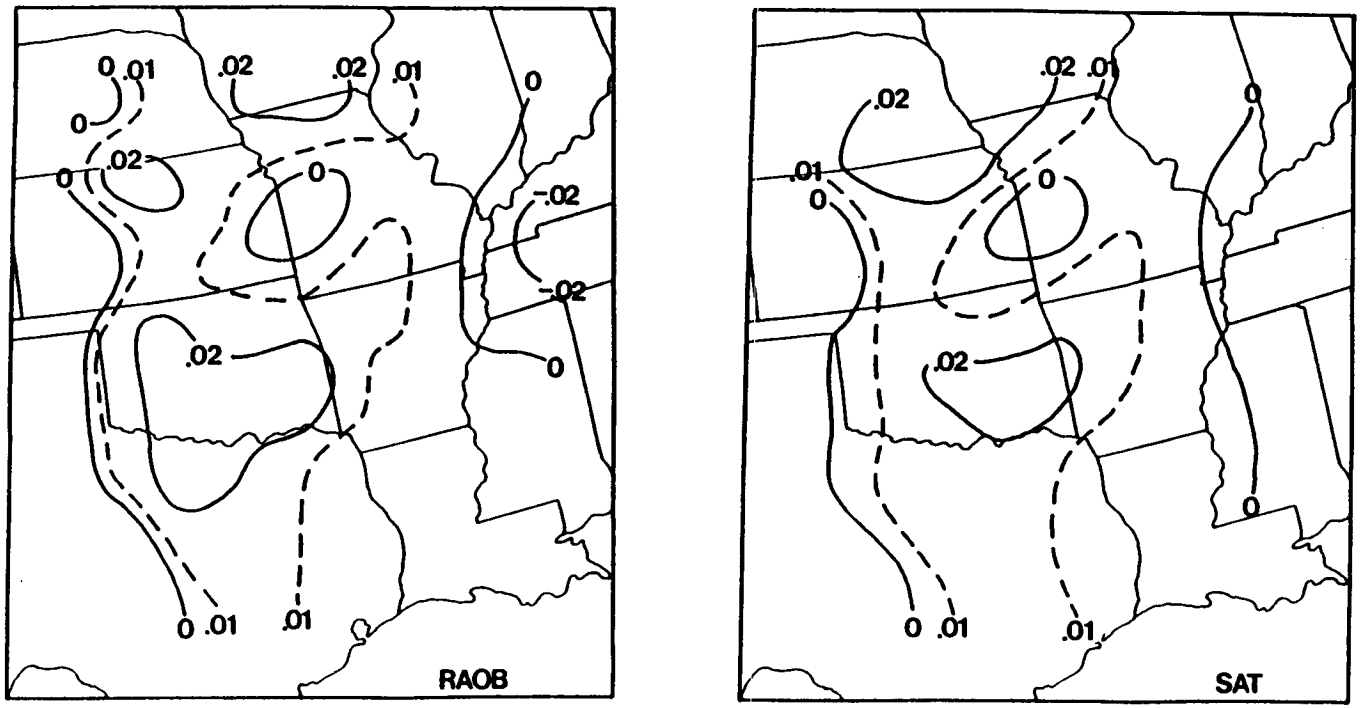


(a) (b)

Fig. 29. Fields of moisture advection ($10^{-4}$ g $kg^{-1}$ $s^{-1}$) at 300 m AGL derived from (a) RAOB and (b) satellite data.

the area, with an additional small center over the Kansas-Missouri border.

Fields of horizontal velocity divergence were also computed (Fig. 30). Since it contributes most of the variability in $w(\vec{\nabla}_2 \cdot \vec{V}_2)$, $\vec{\nabla}_2 \cdot \vec{V}_2$ reflects the same general features exhibited by moisture divergence (Fig. 27). Maximum convergence (negative divergence) values of $-3.3 \times 10^{-5}$ $s^{-1}$ and $-2.9 \times 10^{-5}$ $s^{-1}$ are observed in western Kansas for RAOB and satellite data, respectively.

Patterns of relative vorticity based on RAOB and satellite modified Ekman winds are given in Fig. 31 for 300 m AGL. Again, the two types of wind data produce very similar results. Both fields show positive vorticity in the western portion of the grid area. Positive vorticity is also indicated over southeastern Missouri and eastern Arkansas. These positive areas correspond to centers of moisture convergence detailed in Fig. 27.

Finally, vertical motion was computed at the top of the PBL using the approach described in Chapter 5, Section g. Similar patterns result from the two data sets (Fig. 32). Specifically, maximum upward vertical motion (UVM) occurs in the western third of the grid area where the majority of the convective activity later developed (Fig. 28). Values derived from satellite data are slightly weaker than those based on

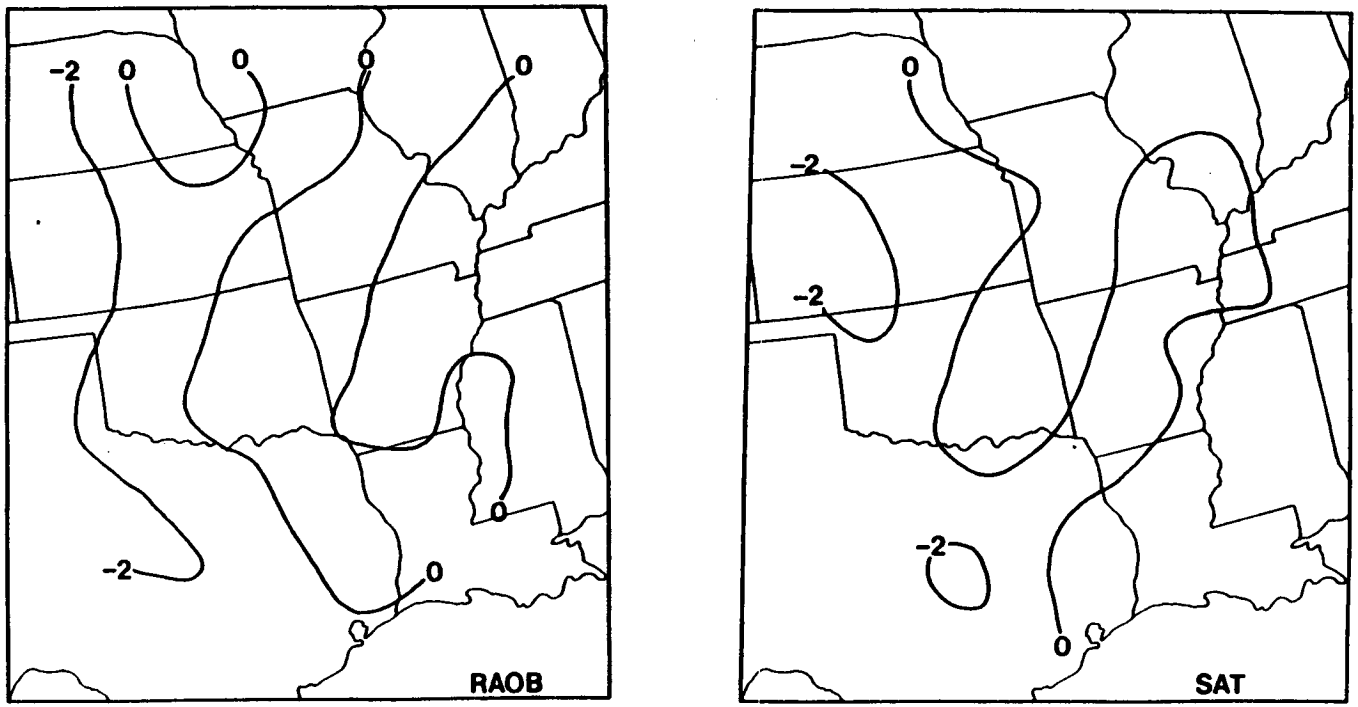


(a) (b)

Fig. 30. Fields of horizontal velocity divergence ($10^{-5}$ $s^{-1}$) at 300 m AGL derived from (a) RAOB and (b) satellite data.

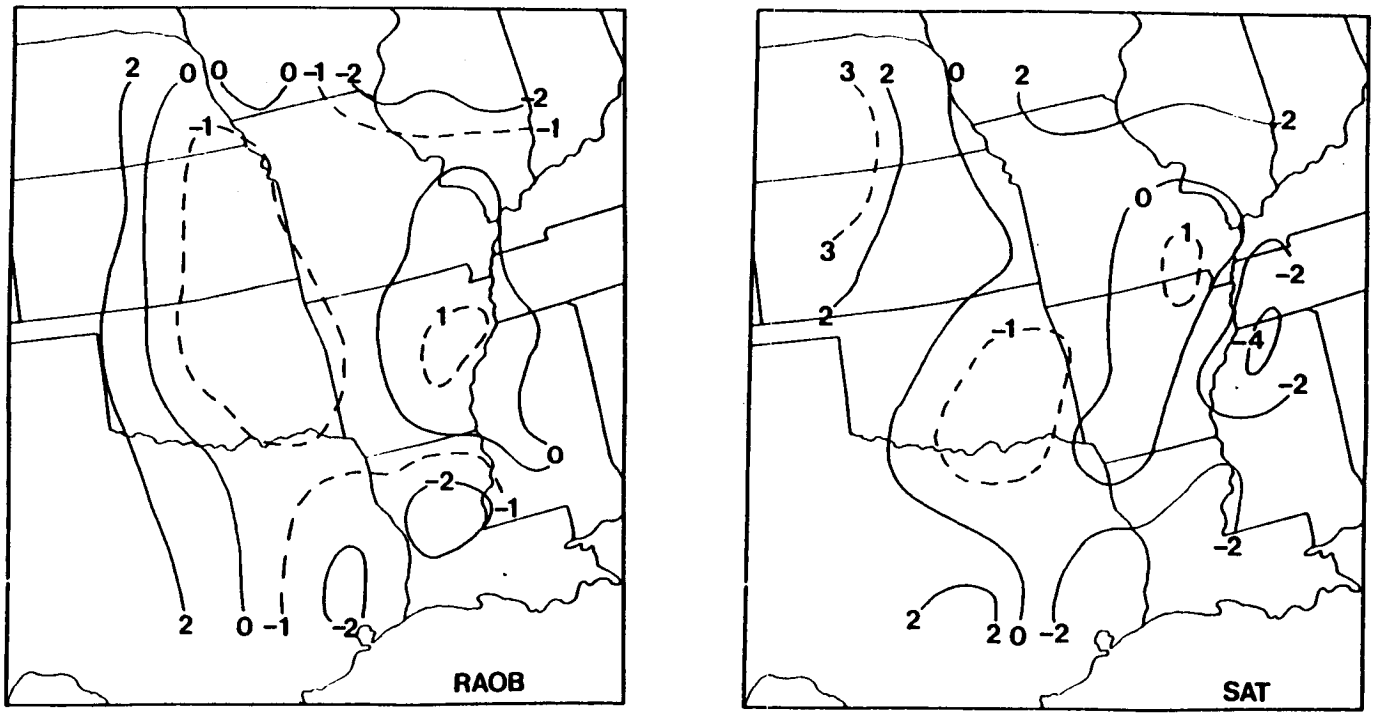


(a) (b)

Fig. 31. Fields of relative vorticity ($10^{-5}$ $s^{-1}$) at 300 m AGL derived from (a) RAOB and (b) satellite data.

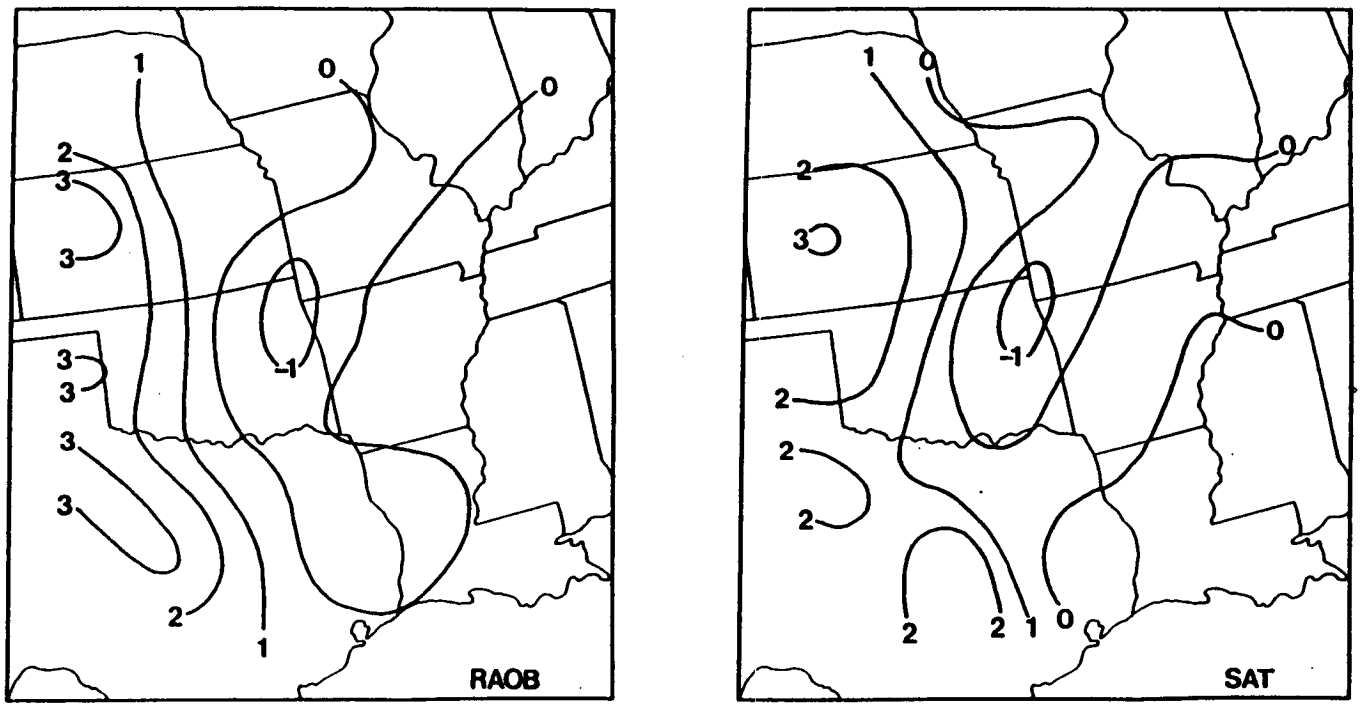


(a) (b)

Fig. 32. Fields of vertical motion (cm $s^{-1}$) at the top of the PBL based on (a) RAOB and (b) satellite data.

RAOB data (e.g., 3.0 versus 3.6 cm $s^{-1}$, respectively, in western Kansas). Weak UVM also is indicated by both types of winds in the southeastern portion of the network. Areas of UVM coincide closely with regions of moisture convergence (Fig. 27), velocity convergence (Fig. 30) and positive vorticity (Fig. 31). This correspondence among parameters holds for both RAOB and satellite data. Finally, descending motion occurs in the central section where values are $\sim$-1.0 cm $s^{-1}$ in both cases.

Again, it is prudent to recall that the satellite-derived vertical velocities and other kinematic parameters are based on data observed approximately 2 h prior to their RAOB-derived counterparts. Given the already close correspondence between kinematic fields from RAOB and satellite sources, it is conceivable that even better agreement would have been obtained from concurrent data.

## 7. SUMMARY AND CONCLUSIONS

In summary, this study has examined the feasibility of using satellite-derived thermal data to obtain synoptic-scale winds in the planetary boundary layer. A diagnostic computational scheme based on the AFGWC-BLM modified Ekman equations was employed. Sixty-two predawn (0921 GMT 19 April 1979) TIROS-N soundings provided the data necessary to compute modified Ekman winds at seven levels between the surface and 1600 m AGL. Similarly-derived wind fields based on 39 rawinsonde soundings (taken approximately 2 h later) were used as a basis for comparison. Comparisons were also made with "observed" winds generated from contact data for 26 of the RAOB soundings.

Qualitative and statistical comparisons revealed that satellite-derived modified Ekman winds show excellent agreement with corresponding wind fields derived from RAOB thermal data. Satellite winds tended to be slightly weaker than their RAOB counterparts (due primarily to their slightly weaker thermal gradients), and exhibited a greater degree of cross-isobaric flow. Closest agreement between the two data sets was at 300 m AGL, the level at which nearly half of the RAOB soundings were affected by inversions. Although both sets of thermally-derived winds compared favorably with the "observed" patterns, the RAOB-derived values were slightly better in this regard. The Ekman winds were clearly superior to geostrophic winds in the

levels nearest the surface.

A sensitivity analysis was performed to determine the effect on the computed winds of the depth of the surface layer ($h$), horizontal variations of $K_m$ and the random error in the satellite-derived temperature data. Through comparisons with the "actual" wind fields, $h = 50$ m was found optimum for use in computing RAOB- and satellite-derived modified Ekman winds. Values of $K_m$ calculated separately at each gridpoint in the plane $z = h$, rather than the use of the mean value, also yielded more satisfactory results overall, particularly between the surface and 300 m AGL. And finally, variations in the wind speeds attributable to random temperature errors in satellite data were reduced (through objective analysis) to less than 0.9 m $s^{-1}$ near the surface and 0.3 m $s^{-1}$ in the upper half of the PBL.

Kinematic parameters computed using satellite thermal data were very comparable to their RAOB-derived counterparts. Areas of horizontal moisture convergence, velocity convergence, and positive vorticity were nearly coincident and aligned in regions which later developed significant convection. Moisture advection was shown by both satellite and RAOB data to be two orders of magnitude smaller than values of moisture divergence/convergence and, thus, relatively insignificant in this synoptic situation. Patterns of vertical motion at 1600 m

AGL that were deduced from satellite winds in the PBL reflected values and features similar to their RAOB-derived counterparts. Regions of maximum upward motion (for both data sets) corresponded to the areas of greatest moisture convergence.

The main conclusion to be drawn from this research is that thermal gradients obtained from satellite data were sufficient to generate realistic synoptic-scale winds in the PBL. These wind patterns were comparable to those obtained from RAOB-derived thermal gradients. The quality of the satellite-generated winds suggests that they could either augment, or be used in the lieu of (e.g., over oceanic areas), RAOB winds in the lowest levels of the atmosphere. A further conclusion is that satellite-derived moisture fields, long considered to be poorly defined, yielded low-level patterns of horizontal moisture convergence which successfully indicated areas of later developing intense convection.

Further research expanding upon the findings of this study are indicated in several areas. Two limitations have been the smallness of the size of the sample case and the fact that only one map time was available. Generation of satellite-derived modified Ekman winds (and associated kinematic parameters) at several time periods would provide a temporal continuity not available during the current study. VAS satellite soundings, taken at 3 h intervals for example, would be particularly

suited to such research. Additional case studies, including the selection of a more unstable period, would further test the usefulness of the computational procedure.

The aim of the present study was not to explore the intricacies of the AFGWC-BLM (e.g., systematic model errors) but rather to use this operational model as a tool to make preliminary calculations of satellite-derived PBL winds. It is felt, however, that the model could yield improved results by allowing the eddy viscosity to vary with altitude, e.g., linearly decreasing $K_m$ with height such that it vanishes at the top of the Ekman layer (as suggested by Estoque, 1973). Application of satellite data to other (improved) boundary layer models which deal with mean motion is also worth future examination.

## APPENDIX A

## DERIVATION OF MODEL EQUATIONS

### DERIVATIONS OF SURFACE LAYER EQUATIONS

Recall equations (3-3), (3-4), and (2-11):

$$K\frac{\partial s}{\partial z} = u_*^2 \tag{A-1}$$

$$K\left[\frac{\partial T}{\partial z} + \frac{g}{c_p}\right] = u_*\vartheta_* \tag{A-2}$$

$$R_i = \frac{g}{\vartheta}\left[\frac{\partial T}{\partial z} + \frac{g}{c_p}\right]\left[\frac{\partial s}{\partial z}\right]^{-2} \tag{A-3}$$

Forced Convection Regime

Recall the "forced" expression for the eddy viscosity, equation (3-6):

$$K = [kz(1-\beta R_i)]^2 \frac{\partial s}{\partial z} \tag{A-4}$$

Derivation 1: Forced S

Substituting (A-3) into (A-4):

$$K = \left[kz\left[1-\beta\left\{\frac{g}{\vartheta}\left[\frac{\partial T}{\partial z} + \frac{g}{c_p}\right]\left[\frac{\partial s}{\partial z}\right]^{-2}\right\}\right]\right]^2 \frac{\partial s}{\partial z} \tag{A-5}$$

Multiplying by $K$:

$$K^2 = \left[kz\left[1-\beta\left\{\frac{g}{\vartheta}\left[\frac{\partial T}{\partial z} + \frac{g}{c_p}\right]\left[\frac{\partial s}{\partial z}\right]^{-2}\right\}\right]\right]^2 K\frac{\partial s}{\partial z} \tag{A-6}$$

Substituting (A-1) into (A-6):

$$K^2 = \left[ kz \left[ 1 - \beta \left\{ \frac{g}{\vartheta} \left[ \frac{\partial T}{\partial z} + \frac{g}{c_p} \right] \left[ \frac{\partial s}{\partial z} \right]^{-2} \right\} \right] \right]^2 u_*^2 \qquad \text{(A-7)}$$

Taking the square root of (A-7):

$$K = kz \left[ 1 - \beta \left\{ \frac{g}{\vartheta} \left[ \frac{\partial T}{\partial z} + \frac{g}{c_p} \right] \left[ \frac{\partial s}{\partial z} \right]^{-2} \right\} \right] u_*$$

$$= kzu_* - kzu_* \frac{\beta g}{\vartheta} \left[ \frac{\partial T}{\partial z} + \frac{g}{c_p} \right] \left[ \frac{\partial s}{\partial z} \right]^{-2} \qquad \text{(A-8)}$$

Rearranging:

$$K \left[ \frac{\partial s}{\partial z} \right]^2 = kzu_* \left[ \frac{\partial s}{\partial z} \right]^2 - kzu_* \frac{\beta g}{\vartheta} \left[ \frac{\partial T}{\partial z} + \frac{g}{c_p} \right] \qquad \text{(A-9)}$$

Multiplying again by $K$:

$$K^2 \left[ \frac{\partial s}{\partial z} \right]^2 = K \left[ \frac{\partial s}{\partial z} \right]^2 kzu_* - kzu_* \frac{\beta g}{\vartheta} K \left[ \frac{\partial T}{\partial z} + \frac{g}{c_p} \right] \qquad \text{(A-10)}$$

Substituting (A-1) and (A-2) into (A-10):

$$u_*^4 = u_*^2 \left[ \frac{\partial s}{\partial z} \right] kzu_* - kzu_* \frac{\beta g}{\vartheta} u_* \vartheta_* \qquad \text{(A-11)}$$

Dividing by $u_*^2$:

$$u_*^2 = \left[ \frac{\partial s}{\partial z} \right] kzu_* - kz\vartheta_* \frac{\beta g}{\vartheta} \qquad \text{(A-12)}$$

Rearranging:

$$\left[ \frac{\partial s}{\partial z} \right] kzu_* = u_*^2 + kz\vartheta_* \frac{\beta g}{\vartheta} \qquad \text{(A-13)}$$

Dividing by $kzu_*$:

$$\frac{\partial s}{\partial z} = \frac{u_*}{kz} + \frac{\vartheta_*}{u_*} \frac{\beta g}{\vartheta} \qquad \text{(A-14)}$$

Integrating with respect to $z$ from $z_*$ to $h$:

$$\int_{z_o}^{h} \frac{\partial s}{\partial z} dz = \int_{z_o}^{h} \frac{u_*}{kz} dz + \int_{z_o}^{h} \frac{\vartheta_*}{u_*} \frac{\beta g}{\vartheta} dz$$

$$= \frac{u_*}{k} \int_{z_o}^{h} \left(\frac{1}{z}\right) dz + \frac{\vartheta_*}{u_*} \frac{\beta g}{\vartheta} \int_{z_o}^{h} dz$$

$$s(z=h) - s(z=z_o) = \frac{u_*}{k} \ln\left(\frac{h}{z_o}\right) + \frac{\vartheta_*}{u_*} \frac{\beta g}{\vartheta} (h - z_o) \qquad \text{(A-15)}$$

The wind speed is assumed to vanish at $z = z_o$, thus:

$$S = s(z=h) = \frac{u_*}{k} \ln\left(\frac{h}{z_o}\right) + \frac{\vartheta_*}{u_*} \frac{\beta g}{\vartheta} (h - z_o) \qquad \text{(A-16)}$$

Derivation 2: Forced $K_m$

Substituting (A-1) into (A-2):

$$u_*^2 \left[\frac{\partial s}{\partial z}\right]^{-1} \left[\frac{\partial T}{\partial z} + \frac{g}{c_p}\right] = u_* \vartheta_* \qquad \text{(A-17)}$$

Rearranging:

$$\left[\frac{\partial T}{\partial z} + \frac{g}{c_p}\right] \left[\frac{\partial s}{\partial z}\right]^{-1} = \frac{\vartheta_*}{u_*} \qquad \text{(A-18)}$$

Substituting (A-18) into (A-3):

$$R_i = \frac{g}{\vartheta} \left[\frac{\partial s}{\partial z}\right]^{-1} \frac{\vartheta_*}{u_*} \qquad \text{(A-19)}$$

Rearranging (A-1):

$$\frac{K}{u_*^2} = \left[\frac{\partial s}{\partial z}\right]^{-1} \qquad \text{(A-20)}$$

Substituting (A-20) into (A-19):

$$R_i = \frac{g}{\vartheta} \frac{K}{u_*^2} \frac{\vartheta_*}{u_*} \qquad \text{(A-21)}$$

Inverting (A-20) and substituting into (A-4):

$$K = [kz(1-\beta R_i)]^2 \frac{u_*^2}{K} \qquad \text{(A-22)}$$

Multiplying (A-22) by $\frac{K}{u_*^2}$:

$$\frac{K^2}{u_*^2} = [kz(1-\beta R_i)]^2 \tag{A-23}$$

Taking the square root of (A-23):

$$\frac{K}{u_*} = kz(1-\beta R_i) \tag{A-24}$$

Substituting (A-24) into (A-21):

$$R_i = \frac{g}{\vartheta}\frac{\vartheta_*}{u_*^2} kz(1-\beta R_i) \tag{A-25}$$

Let us now examine the term $(1-\beta R_i)$:

$$(1-\beta R_i) = 1 - \frac{(1-\beta R_i)}{(1-\beta R_i)}\beta R_i \tag{A-26}$$

Substituting (A-25) for the last $R_i$ on the RHS of (A-26):

$$(1-\beta R_i) = 1 - \frac{(1-\beta R_i)}{(1-\beta R_i)}\beta\left[\frac{g}{\vartheta}\frac{\vartheta_*}{u_*^2} kz(1-\beta R_i)\right]$$

$$= 1 - (1-\beta R_i)\frac{\beta g}{\vartheta}\frac{\vartheta_*}{u_*^2} kz \tag{A-27}$$

Rearranging (A-27):

$$(1-\beta R_i) + (1-\beta R_i)\frac{\beta g}{\vartheta}\frac{\vartheta_*}{u_*^2} kz = 1 \tag{A-28}$$

$$(1-\beta R_i)\left[1 + \frac{\beta g}{\vartheta}\frac{\vartheta_*}{u_*^2} kz\right] = 1 \tag{A-29}$$

$$(1-\beta R_i) = \left[1 + \frac{\beta g}{\vartheta}\frac{\vartheta_*}{u_*^2} kz\right]^{-1} \tag{A-30}$$

Substituting (A-30) into (A-24):

$$K = kzu_*\left[1 + \frac{\beta g}{\vartheta}\frac{\vartheta_*}{u_*^2} kz\right]^{-1} \tag{A-31}$$

Evaluating $K$ at $z = h$, the exchange coefficient for momentum for forced convection conditions becomes:

$$K_m = khu_*\left[1 + \frac{\beta g}{\vartheta}\frac{\vartheta_*}{u_*^2} kh\right]^{-1} \tag{A-32}$$

[As an intermediate result of the above derivation,

(A-30) may be rearranged to yield the alternate expression for $R_i$ given in equation (3-19).]

Free Convection Regime

Recall the "free" expression for the eddy exchange coefficient, equation (3-5):

$$K = \lambda z^2 \left[ \frac{g}{\vartheta} \left| \frac{\partial T}{\partial z} + \frac{g}{c_p} \right| \right]^{1/2} \tag{A-33}$$

where $\lambda$ is a dimensionless constant equal to 1.2 (Gerrity, 1967). In terms of momentum, however, the "free" eddy viscosity is only 70% of (A-33) (Priestly, 1959), i.e.,

$$K_{(M)} = 0.70 \left\{ \lambda z^2 \left[ \frac{g}{\vartheta} \left| \frac{\partial T}{\partial z} + \frac{g}{c_p} \right| \right]^{1/2} \right\} . \tag{A-34}$$

Derivation 3: Free S

Rearranging (A-2), take the absolute value (recalling that $K$ is always positive):

$$\left| \frac{\partial T}{\partial z} + \frac{g}{c_p} \right| = \frac{|u_* \vartheta_*|}{K} \tag{A-35}$$

Substituting (A-35) into (A-34):

$$K = 0.70 \left\{ \lambda z^2 \left[ \frac{g}{\vartheta} \frac{|u_* \vartheta_*|}{K} \right]^{1/2} \right\} \tag{A-36}$$

Squaring (A-36):

$$K^2 = 0.49 \lambda^2 z^4 \frac{g}{\vartheta} \frac{|u_* \vartheta_*|}{K} \tag{A-37}$$

Multiplying by $K$:

$$K^3 = 0.49 \lambda^2 z^4 \frac{g}{\vartheta} |u_* \vartheta_*| \tag{A-38}$$

Rearranging (A-1) and cubing:

$$K^3 = u_*^6 \left[\frac{\partial s}{\partial z}\right]^{-3} \tag{A-39}$$

Substituting (A-39) into (A-38):

$$u_*^6 \left[\frac{\partial s}{\partial z}\right]^{-3} = 0.49\,\lambda^2 z^4 \frac{g}{\bar{\vartheta}} |u_*\vartheta_*| \tag{A-40}$$

Rearranging:

$$\left[\frac{\partial s}{\partial z}\right]^3 = 2.04 \frac{u_*^6}{\lambda^2 z^4} \frac{\bar{\vartheta}}{g} \frac{1}{|u_*\vartheta_*|} \tag{A-41}$$

Taking the cube root:

$$\begin{aligned}\frac{\partial s}{\partial z} &= \left[2.04 \frac{u_*^6}{\lambda^2 z^4} \frac{\bar{\vartheta}}{g} \frac{1}{|u_*\vartheta_*|}\right]^{1/3} \\ &= (2.04)^{1/3} \frac{u_*^2}{\lambda^{2/3} z^{4/3}} \left[\frac{\bar{\vartheta}}{g}\right]^{1/3} \frac{1}{|u_*\vartheta_*|^{1/3}} \\ &= 1.27 \frac{u_*^2}{\lambda^{2/3} |u_*\vartheta_*|^{1/3}} \left[\frac{\bar{\vartheta}}{g}\right]^{1/3} z^{-4/3}\end{aligned} \tag{A-42}$$

Gerrity notes that between $z_*$ and ($z_0$+1 m.) a logarithmic wind profile is assumed to exist. By definition, the logarithmic wind profile for turbulent flow is given by:

$$\bar{s} = \frac{u_*}{k} \ln\left[\frac{z+z_0}{z_0}\right] \tag{A-43}$$

where $z$ and $z_0$ are comparable; for our purposes, $z$ = 1 m. Thus,

$$\int_{z_0}^{z_0+1} \frac{\partial s}{\partial z} dz \equiv \bar{s} = \frac{u_*}{k} \ln\left[\frac{z_0+1}{z_0}\right]$$

$$s(z=z_0+1) - s(z=z_0) = \frac{u_*}{k} \ln\left[\frac{z_0+1}{z_0}\right] \tag{A-44}$$

Now integrating (A-42) with respect to $z$ from $z_0$+1 m. to $h$:

$$\int_{z_o+1}^{h} \frac{\partial s}{\partial z} dz = \int_{z_o+1}^{h} 1.27 \frac{u_*^2}{\lambda^{2/3} |u_* \vartheta_*|^{1/3}} \left[\frac{\bar{\vartheta}}{g}\right]^{1/3} z^{-4/3} \, dz$$

$$= 1.27 \frac{u_*^2}{\lambda^{2/3} |u_* \vartheta_*|^{1/3}} \left[\frac{\bar{\vartheta}}{g}\right]^{1/3} \int_{z_o+1}^{h} z^{-4/3} dz$$

$$= 1.27 \frac{u_*^2}{\lambda^{2/3} |u_* \vartheta_*|^{1/3}} \left[\frac{\bar{\vartheta}}{g}\right]^{1/3} [-3z^{-1/3}]\Big|_{z_o+1}^{h}$$

$$s(z=h) - s(z=z_o+1) = -3.8 \frac{u_*^2}{\lambda^{2/3} |u_* \vartheta_*|^{1/3}} \left[\frac{\bar{\vartheta}}{g}\right]^{1/3} \times$$

$$[h^{-1/3} - (z_o + 1\,m)^{-1/3}] \qquad \text{(A-45)}$$

Substituting (A-44) into (A-45) and rearranging:

$$S \equiv s(z = h) = \frac{u_*}{k} \ln\left[\frac{z_o+1}{z_o}\right] - 3.8 \frac{u_*^2}{\lambda^{2/3} |u_* \vartheta_*|^{1/3}} \left[\frac{\bar{\vartheta}}{g}\right]^{1/3} \times$$

$$[h^{-1/3} - (z_o+1)^{-1/3}], \qquad \text{(A-46)}$$

Derivation 4: Free $K_m$

An expression for "free" $K_m$ is obtained by following the above derivation of $S$ to equation (A-38). Evaluating (A-38) at $z = h$ and taking the cube root:

$$K_m = \left[0.49 \lambda^2 h^6 \left[\frac{g}{\bar{\vartheta}}\right] |u_* \vartheta_*|\right]^{1/3}$$

The constant $\vartheta_*$ is common to both free and forced convection equations. Deriving an expression for $\vartheta_*$ using the "free" equations yields a highly constrained equation involving complex variables. However, a more suitable expression may be obtained using the "forced" equations.

Derivation 5: $\vartheta_*$

Rearranging (A-1):

$$\frac{\partial s}{\partial z} = \frac{u_*^2}{K} \tag{A-48}$$

Rearranging (A-2):

$$K = u_* \vartheta_* \left[\frac{\partial T}{\partial z} + \frac{g}{c_p}\right]^{-1} \tag{A-49}$$

Substituting (A-49) into (A-48):

$$\frac{\partial s}{\partial z} = \frac{u_*^2}{u_* \vartheta_*} \left[\frac{\partial T}{\partial z} + \frac{g}{c_p}\right] \tag{A-50}$$

Recall (A-14). Substituting (A-50) into (A-14):

$$\frac{u_*}{\vartheta_*} \left[\frac{\partial T}{\partial z} + \frac{g}{c_p}\right] = \frac{u_*}{kz} + \frac{\vartheta_*}{u_*} \frac{\beta g}{\bar{\vartheta}} \tag{A-51}$$

Multiplying by $\frac{\vartheta_*}{u_*}$:

$$\left[\frac{\partial T}{\partial z} + \frac{g}{c_p}\right] = \frac{\vartheta_*}{kz} + \frac{\vartheta_*^2}{u_*^2} \frac{\beta g}{\bar{\vartheta}} \tag{A-52}$$

Integrating with respect to $z$ from the height of the instrument shelter, $z_i$ (~1m.), to $h$:

$$\int_{z_i}^{h} \left[\frac{\partial T}{\partial z} + \frac{g}{c_p}\right] dz = \int_{z_i}^{h} \left[\frac{\vartheta_*}{kz} + \frac{\vartheta_*^2}{u_*^2} \frac{\beta g}{\bar{\vartheta}}\right] dz \tag{A-53}$$

$$\int_{z_i}^{h} \frac{\partial T}{\partial z} dz + \int_{z_i}^{h} \frac{g}{c_p} dz = \int_{z_i}^{h} \frac{\vartheta_*}{kz} dz + \int_{z_i}^{h} \frac{\vartheta_*^2}{u_*^2} \frac{\beta g}{\bar{\vartheta}} dz \tag{A-54}$$

$$(T_h - T_i) + \frac{g}{c_p}(h - z_i) = \frac{\vartheta_*}{k} \ln\left(\frac{h}{z_i}\right) + \frac{\vartheta_*^2}{u_*^2} \frac{\beta g}{\bar{\vartheta}} (h - z_i) \tag{A-55}$$

Dividing by $(h - z_i)$ and rearranging:

$$\left[\frac{\beta g}{\bar{\vartheta} u_*^2}\right] \vartheta_*^2 + \left[\frac{\ln\left(\frac{h}{z_i}\right)}{k(h - z_i)}\right] \vartheta_* = \frac{T_h - T_i}{h - z_i} + \frac{g}{c_p} \tag{A-56}$$

Equation (A-56) can be solved for $\vartheta_*$ through use of the quadratic formula. Let:

$$a = \frac{\beta g}{\bar{\vartheta} u_*^2}, \qquad b = \frac{\ln\left(\frac{h}{z_i}\right)}{k(h - z_i)}, \qquad c = -\left[\frac{T_h - T_i}{h - z_i} + \frac{g}{c_p}\right]$$

Thus,

$$a\vartheta_*^2 + b\vartheta_* + c = 0 \tag{A-57}$$

Using the quadratic formula:

$$\vartheta_* = \frac{-b \pm \sqrt{b^2-4ac}}{2a} \tag{A-58}$$

There are two possible roots to (A-58):

$$r_1 = \frac{-b + \sqrt{b^2-4ac}}{2a} \quad \text{and} \quad r_2 = \frac{-b - \sqrt{b^2-4ac}}{2a} .$$

$\vartheta_*$ must vanish for neutral stratification. Under neutral conditions the lapse rate becomes $\left[-\frac{g}{c_p}\right]$; looking at the constant c:

$$c = -\left[\frac{T_h - T_i}{h - z_i} + \frac{g}{c_p}\right] = -\left[\frac{\partial T}{\partial z} + \frac{g}{c_p}\right] = -\left[-\frac{g}{c_p} + \frac{g}{c_p}\right] = 0$$

Thus, $r_1$ is the appropriate solution, giving:

$$\vartheta_* = \frac{-\left[\frac{\ln(\frac{h}{z_i})}{k(h-z_i)}\right] + \left\{\left[\frac{\ln(\frac{h}{z_i})}{k(h-z_i)}\right]^2 + \frac{4\beta g}{\bar{\vartheta} u_*^2}\left[\frac{T_h - T_i}{h - z_i} + \frac{g}{c_p}\right]\right\}^{1/2}}{\frac{2\beta g}{\bar{\vartheta} u_*^2}}$$

$$= \frac{u_*^2 \bar{\vartheta}}{2\beta g}\left[-\frac{\ln(\frac{h}{z_i})}{k(h-z_i)} + \left\{\left[\frac{\ln(\frac{h}{z_i})}{k(h-z_i)}\right]^2 + \frac{4\beta g}{\bar{\vartheta} u_*^2}\left[\frac{T_h - T_i}{h - z_i} + \frac{g}{c_p}\right]\right\}^{1/2}\right]$$

$$= -\frac{u_*^2 \bar{\vartheta}}{2\beta g}\,\frac{\ln(\frac{h}{z_i})}{k(h-z_i)}\left[1.0 - \frac{k(h-z_i)}{\ln(\frac{h}{z_i})}\left\{\left[\frac{\ln(\frac{h}{z_i})}{k(h-z_i)}\right]^2 + \frac{4\beta g}{\bar{\vartheta} u_*^2}\left[\frac{T_h - T_i}{h - z_i} + \frac{g}{c_p}\right]\right\}^{1/2}\right]$$

$$= -\frac{u_*^2 \bar{\vartheta}}{2\beta g}\,\frac{\ln(\frac{h}{z_i})}{k(h-z_i)}\left[1.0 - \left\{1.0 + \frac{4\beta g}{\bar{\vartheta} u_*^2}\left[\frac{T_h - T_i}{h - z_i} + \frac{g}{c_p}\right]\left[\frac{k(h-z_i)}{\ln(\frac{h}{z_i})}\right]^2\right\}^{1/2}\right] \tag{A-59}$$

Derivation 6: Modified Ekman Equations

Recall from Chapter 3 (Sections a and d), the horizontal equations of motion, (3-1) and (3-2), and the simplifying assumptions (3) and (4):

$$\frac{du}{dt} = fv - \frac{1}{\rho}\left[\frac{\partial p}{\partial x} + \rho g \frac{\partial E}{\partial x}\right] + \frac{\partial}{\partial z}\left[K_m \frac{\partial u}{\partial z}\right] \tag{A-60a}$$

$$0 = fv - fv_g + K_m \frac{\partial^2 u}{\partial z^2} \tag{A-60b}$$

and

$$\frac{dv}{dt} = -fu - \frac{1}{\rho}\left[\frac{\partial p}{\partial y} + \rho g \frac{\partial E}{\partial y}\right] + \frac{\partial}{\partial z}\left[K_m \frac{\partial v}{\partial z}\right] \tag{A-61a}$$

$$0 = -fu + fu_g + K_m \frac{\partial^2 v}{\partial z^2} \tag{A-61b}$$

We now introduce the complex variable $i$, where $i = \sqrt{-1}$ and $i^2 = -1$. Multiplying (A-61b) by $i$ and combining with (A-60b):

$$0 = -ifu + ifu_g + K_m \frac{\partial^2}{\partial z^2}(iv) \tag{A-62}$$

$$0 = \quad fv - fv_g + K_m \frac{\partial^2}{\partial z^2}(u)$$

$$0 = -ifu + fv + ifu_g - fv_g + K_m \frac{\partial^2}{\partial z^2}(u + iv) \tag{A-63}$$

Rearranging:

$$0 = if(u_g + iv_g) - if(u + iv) + K_m \frac{\partial^2}{\partial z^2}(u + iv) \tag{A-64}$$

Now we define the complex variables:

$$V = u + iv \qquad \text{and} \qquad V_g = u_g + iv_g$$

Substituting these into (A-64):

$$0 = if V_g - if V + K_m \frac{\partial^2 V}{\partial z^2} \tag{A-65}$$

Recall assumption (5) in Chapter 3, Section d. If $\vec{V}_g$ is linear with height, then the change of the geostrophic <u>shear</u> with height must be zero, i.e., $\frac{d^2\vec{V}_g}{dz^2} = \frac{d^2V_g}{dz^2} = 0$. We can subtract this "zero term" from (A-65) with the following result:

$$0 = -if(V-V_g) + K_m\frac{d^2V}{dz^2} - K_m\frac{d^2V_g}{dz^2}$$

$$= -if(V-V_g) + K_m\frac{d^2}{dz^2}(V-V_g) \qquad \text{(A-66)}$$

We now define: $W = V-V_g$. Substituting this into (A-66):

$$0 = -if\,W + K_m\frac{d^2W}{dz^2} \qquad \text{(A-67)}$$

Dividing by $K_m$ and rearranging:

$$\frac{d^2W}{dz^2} - \left[\frac{if}{K_m}\right]W = 0 \qquad \text{(A-68)}$$

Now let $\begin{cases} i \equiv \frac{1}{2}(i+1)^2 \\ m = (\frac{f}{2K_m})^{1/2} \quad \text{or} \quad m^2 = \frac{f}{2K_m} \end{cases}$

Substituting these into (A-68):

$$\frac{d^2W}{dz^2} - (i+1)^2 m^2 W = 0 \qquad \text{(A-69)}$$

The <u>general solution</u> to (A-69) is:

$$W = a\,e^{(i+1)mz} + b\,e^{-(i+1)mz} \qquad \text{(A-70)}$$

We now have two boundary conditions to consider: the upper and lower extremes of the transition layer. Classically, these limits are set equal to infinity ($\infty$) and zero, respectively.

First B.C.: When $z \to H$, then $V \to V_g$ and $W \to 0$. Setting $H$ equal to $\infty$ and plugging these values into (A-70):

$$0 = a\, e^{(i+1)m\infty} + b\, e^{-(i+1)m\infty}$$

Since $e^{\infty} = \infty$, this implies that $a = 0$ and we are left with:

$$W = b\, e^{-(i+1)mz} \tag{A-71}$$

Second B.C.: When $z \to h$, then $W(=V-V_g) \to \tilde{V}-V_g^h$ where V is the wind computed from applicable surface layer equations ($\tilde{V} = U + iV$), and $V_g^h$ is the geostrophic wind at $z = h$ ($V_g^h = u_g^h + iv_g^h$). To set the height coordinate equal to zero at $h$, let us redefine $z$ as $(z-h)$. Plugging these values into (A-71):

$$\tilde{V}-V_g^h = b\, e^{-(i+1)m0}$$

Since $e^0 = 1$, $b = \tilde{V}-V_g^h$ and the particular solution becomes:

$$W = (\tilde{V}-V_g^h)\, e^{-(i+1)mz} \tag{A-72}$$

Expanding the various terms, (A-72) becomes:

$$V-V_g = (\tilde{V}-V_g^h)\, e^{-(i+1)mz}$$

$$(u+iv) - (u_g+iv_g) = [(U+iV) - (u_g^h + iv_g^h)]\, e^{-(i+1)mz} \tag{A-73}$$

Applying Euler's rule ($e^{i\vartheta} = \cos\vartheta + i\sin\vartheta$) to (A-73):

$$(u+iv) - (u_g + iv_g)$$

$$= [(U+iV) - (u_g^h + iv_g^h)]\, e^{-mz}\, [\cos(mz) - i\sin(mz)]$$

$$= (U+iV)\, e^{-mz}\, [\cos(mz) - i\sin(mz)]$$

$$- (u_g^h + iv_g^h)\, e^{-mz}\, [\cos(mz) - i\sin(mz)]$$

$$= Ue^{-mz}\,[\cos(mz) - i\sin(mz)]$$
$$+ iVe^{-mz}\,[\cos(mz) - i\sin(mz)]$$
$$- u_g^h\, e^{-mz}\,[\cos(mz) - i\sin(mz)]$$
$$- iv_g^h\, e^{-mz}[\cos(mz) - i\sin(mz)]$$
$$= Ue^{-mz}\cos(mz) - iUe^{-mz}\sin(mz)$$
$$+ iVe^{-mz}\cos(mz) + Ve^{-mz}\sin(mz)$$
$$- u_g^h\, e^{-mz}\cos(mz) + iu_g^h\, e^{-mz}\sin(mz)$$
$$- iv_g^h\, e^{-mz}\cos(mz) - v_g^h\, e^{-mz}\sin(mz) \qquad \text{(A-74)}$$

Separating the real and imaginary parts of (A-74), we obtain the following equations:

$$u - u_g = Ue^{-mz}\cos(mz) + Ve^{-mz}\sin(mz)$$
$$- u_g^h\, e^{-mz}\cos(mz) - v_g^h\, e^{-mz}\sin(mz)$$
$$= e^{-mz}\,[(U - u_g^h)\cos(mz) + (V - v_g^h)\sin(mz)] \qquad \text{(A-75)}$$

$$v - v_g = -Ue^{-mz}\sin(mz) + Ve^{-mz}\cos(mz)$$
$$+ u_g^h e^{-mz}\sin(mz) - v_g^h\, e^{-mz}\cos(mz)$$
$$= e^{-mz}\,[(V - v_g^h)\cos(mz) - (U - u_g^h)\sin(mz)] \qquad \text{(A-76)}$$

Finally, recall that $z$ was redefined as $(z-h)$. Making the appropriate substitutions and rearranging:

$$u = u_g + e^{-m(z-h)}\{(U - u_g^h)\cos[m(z-h)] + (V - v_g^h)\sin[m(z-h)]\} \qquad \text{(A-77)}$$

$$v = v_g + e^{-m(z-h)}\{(V - v_g^h)\cos[m(z-h)] - (U - u_g^h)\sin[m(z-h)]\} \qquad \text{(A-78)}$$

Derivation I: Modified Geostrophic Equations

Recall assumption (5) from Chapter 3, Section d; as noted previously, if $\vec{V}_g$ is linear with height, then the change of geostrophic shear with height must be zero:

$$\frac{d^2\vec{V}_g}{dz^2} = 0 \tag{A-79}$$

The general solution to (A-79) is of the form:

$$\vec{V}_g = a + bz \tag{A-80}$$

Before determining $a$ and $b$, let us redefine $z$ as $(H-z)$ where $h \leq z \leq H$. Equation (A-80) then becomes:

$$\vec{V}_g = a + b(H-z) \tag{A-81}$$

We now have two boundary conditions to consider:

First B.C.: When $z \to H$, then $\vec{V}_g \to \vec{V}_g^H$. Plugging these into (A-81):

$$\vec{V}_g^H = a + b(H-H)$$

Thus, $a = \vec{V}_g^H$ and (A-81) becomes:

$$\vec{V}_g = \vec{V}_g^H + b(H-z) \tag{A-82}$$

Second B.C.: When $z \to h$, then $\vec{V}_g \to \vec{V}g^h$. Plugging these into (A-82):

$$\vec{V}_g^h = \vec{V}_g^H + b(H-h)$$

Thus, $b = \frac{1}{H-h}(\vec{V}_g^h - \vec{V}_g^H)$ and the particular solution becomes:

$$\vec{V}_g = \vec{V}_g^H + \frac{H-z}{H-h}(\vec{V}_g^h - \vec{V}_g^H) \tag{A-83}$$

This equation is not in a form that suits our needs. We want the component form of (A-83) expressed in terms of temperature. To obtain a more useful form of (A-83), let us consider first the Hypsometric Equation:

$$\left.\begin{aligned} z_2 - z_1 &= -\frac{R\overline{T^*}}{g}\ln\left[\frac{p_2}{p_1}\right] \\ &= \frac{R\overline{T^*}}{g}\ln\left[\frac{p_1}{p_2}\right] \end{aligned}\right\} \quad \text{where } p_2 < p_1$$

Letting $1 \equiv h$ and $2 \equiv H$, and rearranging:

$$\left[\frac{1}{\overline{T^*}}\right] g\ (z_H - z_h) = R \ln\left[\frac{p_h}{p_H}\right] \tag{A-84}$$

Differentiating (A-84) with respect to $x$:

$$\frac{\partial}{\partial x}\left[\left[\frac{1}{\overline{T^*}}\right] g\ (z_H - z_h)\right] = \frac{\partial}{\partial x}\left[R \ln\left[\frac{p_h}{p_H}\right]\right]$$

$$= R\frac{\partial}{\partial x}\left[\ln\left[\frac{p_h}{p_H}\right]\right] + \ln\left[\frac{p_h}{p_H}\right]\frac{\partial}{\partial x}(R)$$

$$= R\left[\left[\frac{p_H}{p_h}\right]\frac{\partial}{\partial x}\left[\frac{p_h}{p_H}\right]\right]$$

$$= R\left[\frac{p_H}{p_h}\right]\left[\left[\frac{1}{p_H}\right]\frac{\partial p_h}{\partial x} - \left[\frac{p_h}{p_H^2}\right]\frac{\partial p_H}{\partial x}\right]$$

$$= R\left[\frac{1}{p_h}\frac{\partial p_h}{\partial x} - \frac{1}{p_H}\frac{\partial p_H}{\partial x}\right] \tag{A-85}$$

From the Equation of State we can write: $p_h = \rho_h R T_h$ and $p_H = \rho_H R T_H$. Substituting these into (A-85):

$$\frac{\partial}{\partial x}\left[\left[\frac{1}{\overline{T^*}}\right] g\ (z_H - z_h)\right] = \frac{p_h}{\rho_h T_h}\left[\frac{1}{p_h}\right]\frac{\partial p_h}{\partial x} - \frac{p_H}{\rho_H T_H}\left[\frac{1}{p_H}\right]\frac{\partial p_H}{\partial x}$$

$$= \left[\frac{1}{\rho_h T_h}\right]\frac{\partial p_h}{\partial x} - \left[\frac{1}{\rho_H T_H}\right]\frac{\partial p_H}{\partial x} \tag{A-86}$$

Multiplying (A-86) by $T_h$:

$$T_h \frac{\partial}{\partial x}\left[\left[\frac{1}{\overline{T^*}}\right] g\ (z_H - z_h)\right] = \frac{1}{\rho_h}\frac{\partial p_h}{\partial x} - \frac{1}{\rho_H}\left[\frac{T_h}{T_H}\right]\frac{\partial p_H}{\partial x} \tag{A-87}$$

Recall that: $v_g = \frac{1}{\rho f}\frac{\partial p}{\partial x} + \frac{g}{f}\frac{\partial E}{\partial x}$. Assuming constant density:

$$T_h \frac{\partial}{\partial x}\left[\left[\frac{1}{\overline{T^*}}\right] g\ (z_H - z_h)\right] = \left[f v_g^h - g\frac{\partial E}{\partial x}\right] - \left[f v_g^H - g\frac{\partial E}{\partial x}\right]\frac{T_h}{T_H} \tag{A-88}$$

Dividing by $f$ and rearranging:

$$T_h \frac{g}{f} \frac{\partial}{\partial x}\left[\left[\frac{1}{\overline{\overline{T^*}}}\right](z_H - z_h)\right] + \frac{g}{f}\frac{\partial E}{\partial x}\left[1 - \frac{T_h}{T_H}\right] + v_g^H\left[\frac{T_h}{T_H}\right] = v_g^h \qquad \text{(A-89)}$$

Subtracting $v_g^H$ from both sides and rearranging terms (b), (c) and (d):

$$T_h \frac{g}{f} \frac{\partial}{\partial x}\left[\left[\frac{1}{\overline{\overline{T^*}}}\right](z_H - z_h)\right] + \overbrace{\frac{g}{f}\frac{\partial E}{\partial x}\left[1 - \frac{T_h}{T_H}\right]}^{\text{(b)}} + \overbrace{v_g^H\left[\frac{T_h}{T_H}\right]}^{\text{(c)}} \overbrace{- v_g^H}^{\text{(d)}} = v_g^h - v_g^H$$

$$\cdots + \frac{g}{f}\frac{\partial E}{\partial x}\left[\frac{T_H}{T_H}\right] - \frac{g}{f}\frac{\partial E}{\partial x}\left[\frac{T_h}{T_H}\right] + v_g^H\left[\frac{T_h}{T_H}\right] - v_g^H\left[\frac{T_H}{T_H}\right] = \cdots$$

$$\cdots - \frac{g}{f}\frac{\partial E}{\partial x}\left[\frac{T_h}{T_H} - \frac{T_H}{T_H}\right] + v_g^H\left[\frac{T_h}{T_H} - \frac{T_H}{T_H}\right] = \cdots$$

$$\cdots - \frac{g}{f}\frac{\partial E}{\partial x}\left[\frac{T_h - T_H}{T_H}\right] + v_g^H\left[\frac{T_h - T_H}{T_H}\right] = \cdots \qquad \text{(A-90)}$$

Rearranging:

$$T_h \frac{g}{f} \frac{\partial}{\partial x}\left[\left[\frac{1}{\overline{\overline{T^*}}}\right](z_H - z_h)\right] - \frac{g}{f}\frac{\partial E}{\partial x}\left[\frac{T_h - T_H}{T_H}\right] + v_g^H\left[\frac{T_h - T_H}{T_H}\right] + v_g^H = v_g^h \qquad \text{(A-91)}$$

Differentiating (A-84) with respect to $y$:

$$\frac{\partial}{\partial y}\left[\left[\frac{1}{\overline{\overline{T^*}}}\right] g\ (z_H - z_h)\right] = \frac{\partial}{\partial y}\left[R \ln\left[\frac{p_h}{p_H}\right]\right]$$

$$\vdots$$

(as in (A-85))

$$\vdots$$

$$= R\left[\frac{1}{p_h}\frac{\partial p_h}{\partial y} - \frac{1}{p_H}\frac{\partial p_H}{\partial y}\right] \qquad \text{(A-92)}$$

Following the same steps as in (A-86) through (A-91), and recalling that $u_g = -\frac{1}{\rho f}\frac{\partial p}{\partial y} - \frac{g}{f}\frac{\partial E}{\partial y}$, we obtain:

$$-T_h \frac{g}{f} \frac{\partial}{\partial y}\left[\left[\frac{1}{\overline{\overline{T^*}}}\right](z_H - z_h)\right] + \frac{g}{f}\frac{\partial E}{\partial y}\left[\frac{T_h - T_H}{T_H}\right] + u_g^H\left[\frac{T_h - T_H}{T_H}\right] + u_g^H = u_g^h \qquad \text{(A-93)}$$

Returning now to our particular solution, (A-83) can be broken down into component form:

Solution for $u_g$:

$$u_g = u_g^H + \frac{H-z}{H-h}\,(u_g^h - u_g^H)$$

Substituting (A-93) for $u_g^h$, and recalling that $z_h \equiv h$ and $z_H \equiv H$:

$$u_g = u_g^H + \frac{H-z}{H-h}\left\{(u_g^H - \tilde{u})\left[\frac{T_h - T_H}{T_H}\right] - T_h \frac{g}{f}\,(H-h)\,\frac{\partial}{\partial y}\left[\frac{1}{\overline{T^*}}\right]\right\} \qquad \text{(A-94)}$$

$$\text{where: } \tilde{u} = -\frac{g}{f}\,\frac{\partial E}{\partial y} \qquad \text{(A-95)}$$

Solution for $v_g$:

$$v_g = v_g^H + \frac{H-z}{H-h}\,(v_g^h - v_g^H)$$

Substituting (A-91) for $v_g^h$:

$$v_g = v_g^H + \frac{H-z}{H-h}\left\{(v_g^H - \tilde{v})\left[\frac{T_h - T_H}{T_H}\right] + T_h \frac{g}{f}\,(H-h)\,\frac{\partial}{\partial x}\left[\frac{1}{\overline{T^*}}\right]\right\} \qquad \text{(A-96)}$$

where

$$\tilde{v} = \frac{g}{f}\,\frac{\partial E}{\partial x} \qquad \text{(A-97)}$$

## APPENDIX B

### RESPONSE DETERMINATION

The Barnes (1973) objective analysis scheme requires selection of two weight function constants (g and 4c) to achieve the desired amplitude response at specific wavelengths. Input temperature, dewpoint, and pressure data were analyzed using the ten combinations of g and 4c given in Table 10. The respective response curves have been shown in Fig. 8. The resulting RAOB- and satellite-derived modified Ekman winds were then compared statistically to "actual" wind fields (objectively analyzed at corresponding responses) to ascertain the most appropriate degree of resolution. The objective analysis that yielded the lowest standard deviations of differences between "actual" and modified Ekman winds, as well as the highest linear correlation coefficients, was judged most appropriate for the investigation. Results from three analyses ($\sim$50% response at wavelengths of 900, 1000, and 1100 km) which most closely matched these criteria are shown in Figs. 33 and 34. Of the three, 900 km exhibited the "best" overall results using RAOB data, but the "worst" results when satellite winds were employed. Conversely, 1100 km had the opposite effect. Thus, a response yielding $\sim$50% resolution of amplitude at 1000 km was deemed best for the three types of data ("actual", RAOB, satellite).

Table 10. Weight function constants selected to achieve approximately 50% response at the indicated wavelengths using the Barnes (1973) objective analysis scheme.

| g | 4c | Wavelength (km) |
|---|---|---|
| 0.2 | 30,000 | 300 |
| 0.4 | 50,000 | 500 |
| 0.3 | 120,000 | 700 |
| 0.4 | 160,000 | 900 |
| 0.4 | 200,000 | 1000 |
| 0.4 | 240,000 | 1100 |
| 0.4 | 400,000 | 1400 |
| 0.4 | 450,000 | 1500 |
| 0.4 | 575,000 | 1700 |
| 0.4 | 800,000 | 2000 |

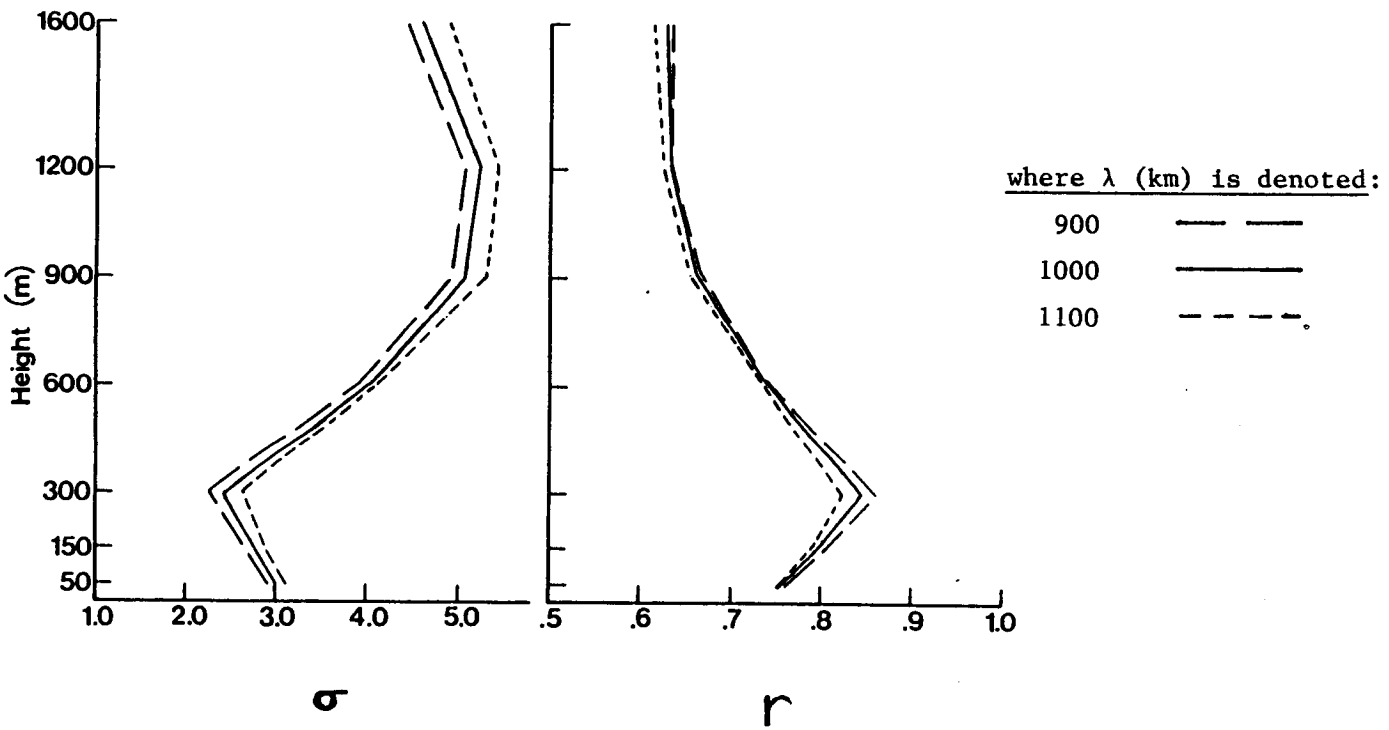


Fig. 33. Vertical profiles of standard deviations (m $s^{-1}$) of the differences between "actual" wind speeds and RAOB-derived modified Ekman wind speeds objectively analyzed for a 50% response at wavelengths of 900, 1000 and 1100 km (left graph). Corresponding linear correlation coefficients are shown in the right graph.

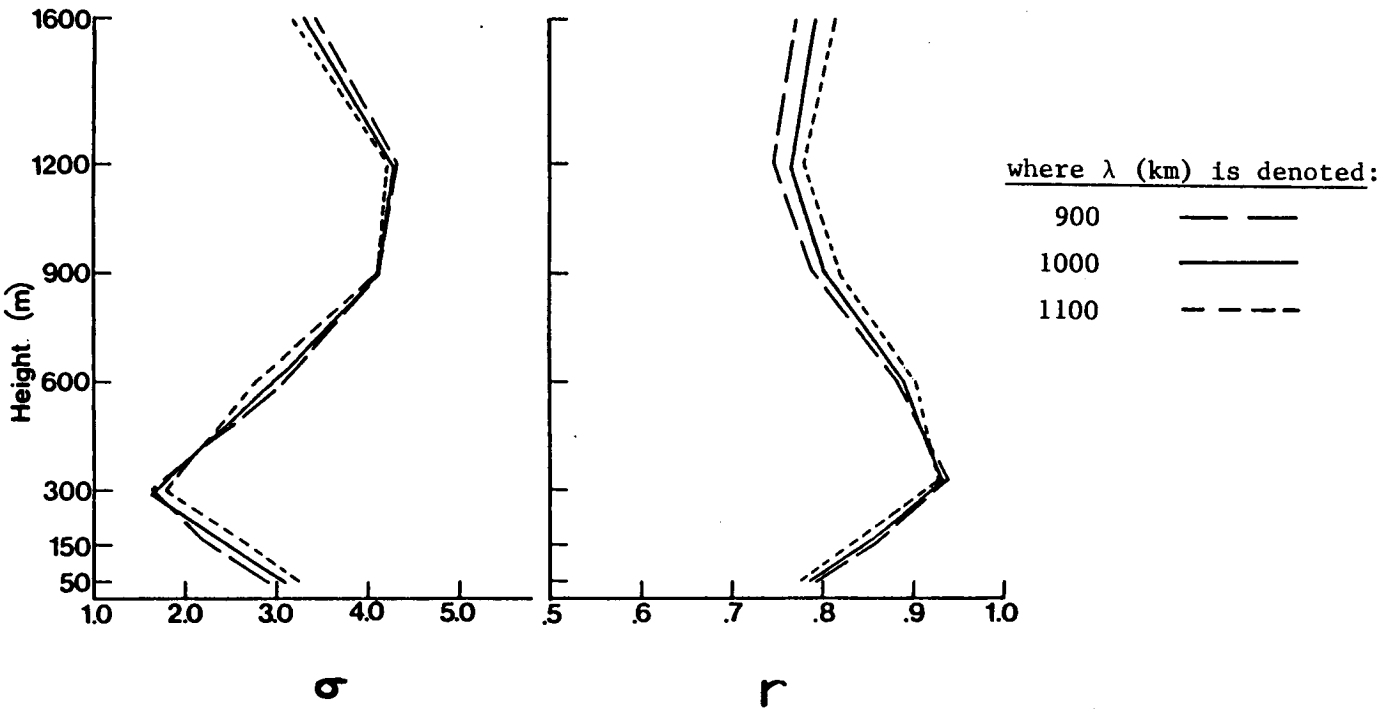


Fig. 34. Same as Fig. 33, except for satellite-derived modified Ekman wind speeds.

## APPENDIX C

## CORRELATION COEFFICIENTS

### LINEAR CORRELATION COEFFICIENT

The product-moment formula for the linear correlation coefficient, $r$, is (see, for example, Panofsky and Brier, 1968):

$$r^2 = \frac{(\Sigma xy)^2}{(\Sigma x^2)(\Sigma y^2)} \tag{A-98}$$

where $x = X - \overline{X}$ and $y = Y - \overline{Y}$. $X$ and $Y$ represent the i-th value of two scalar quantities (temperature, wind speed, etc.) being compared.

### VECTOR CORRELATION COEFFICIENT

Court's total vector correlation coefficient, $R$, relates the wind at one time or space to wind at another time or space (Lambeth, 1966). Given two samples of wind:

$$\vec{W} = U\vec{i} + V\vec{j} \quad \text{and} \quad \vec{Z} = X\vec{i} + Y\vec{j}$$

the vector correlation coefficient is obtained through the expression

$$R^2 = \frac{s_y^2(s_{ux}^2 + s_{vx}^2) + s_x^2(s_{uy}^2 + s_{vy}^2) - 2s_{xy}(s_{ux}s_{uy} + s_{vx}s_{vy})}{(s_u^2 + s_v^2)(s_x^2 s_y^2 - s_{xy}^2)} \tag{A-99}$$

Here $u$, $v$, $x$ and $y$ are deviations from the means, i.e., $u = U - \overline{U}$, etc. The terms $s_u^2$, $s_v^2$, $s_x^2$ and $s_y^2$ denote sample variances of $u$, $v$, $x$ and $y$, respectively; $s_{ux}$, $s_{vx}$, $s_{uy}$, $s_{vy}$ and $s_{xy}$ are covariances of the indicated deviations.

APPENDIX D

## SCALE ANALYSIS OF HORIZONTAL MOMENTUM EQUATIONS

The appropriateness of neglecting individual derivatives (and, hence, the advective terms) in the horizontal momentum equations (Chapter 3, Section d) can be seen in the scale analysis given below. Since only one map time was available for the current study, $\frac{\partial u}{\partial t}$ and $\frac{\partial v}{\partial t}$ were assumed to equal zero. Values of the various terms were computed using "observed" data at 50, 300 and 1200 m AGL for six points representative of the research area (Fig. 35). Averages of values at the six points produced the results shown below. Horizontal and vertical advection terms were one to two orders of magnitude smaller than the Coriolis, pressure gradient and frictional terms at all three levels.

$$u\frac{\partial u}{\partial x},\ v\frac{\partial u}{\partial y},\ u\frac{\partial v}{\partial x},\ v\frac{\partial v}{\partial y}: \quad \sim 10^{-5}\ \mathrm{m\ s^{-2}}$$

$$w\frac{\partial u}{\partial z},\ w\frac{\partial v}{\partial z}: \quad \sim 10^{-5}\ \mathrm{m\ s^{-2}}$$

$$fv,\ -fu: \quad \sim 10^{-4}\ \mathrm{m\ s^{-2}}$$

$$-\frac{1}{\rho}\frac{\partial p}{\partial x},\ -\frac{1}{\rho}\frac{\partial p}{\partial y}: \quad \sim 10^{-3}\ \mathrm{m\ s^{-2}}$$

$$K_m\frac{\partial^2 u}{\partial z^2},\ K_m\frac{\partial^2 v}{\partial z^2}: \quad \sim 10^{-3}\ \mathrm{m\ s^{-2}}$$

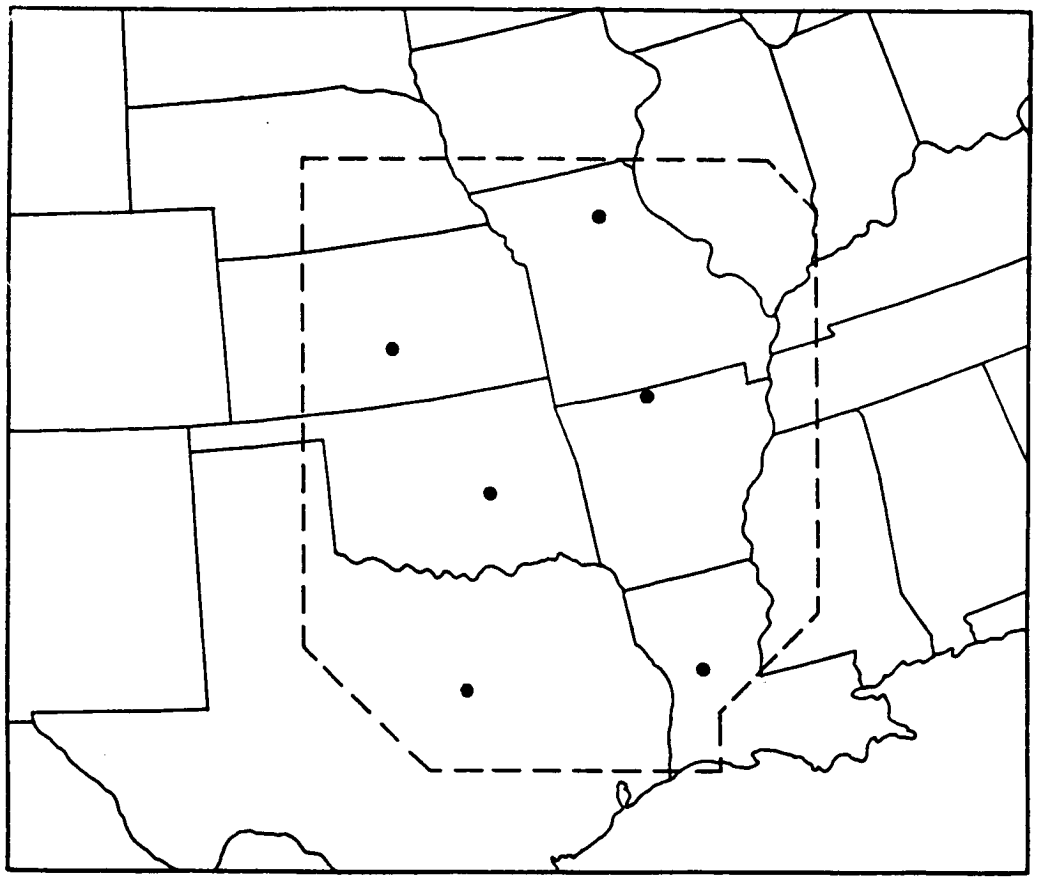

Fig. 35. Data points used in scale analysis.

APPENDIX E

## BAROCLINICITY IN THE PBL

The PBL under study is noted in Chapter 6, Section d, as being forced convective in nature, though nearly stable. The weak baroclinicity that is implied can be described by the amount of vertical geostrophic shear and, near the surface, the degree of stress and cross-isobaric flow.

The terms geostrophic shear and baroclinicity may be considered synonymous. Inserting RAOB-derived thermal data into (3-34) and (3-35) (forms of the thermal wind equations), a mean geostrophic wind shear of 0.8 m $s^{-1}$ $km^{-1}$ is obtained over the research area. This is much smaller than is the $\sim$2.0 m $s^{-1}$ $km^{-1}$ shear given by Krishna (1981) and is less than one-fourth the 3.5 m $s^{-1}$ $km^{-1}$ noted by Arya and Wyngaard (1975) for a typical midlatitude baroclinic PBL.

The amount of stress ($\tau$) in the surface layer may also indicate the degree of baroclinicity. Values of surface stress tabulated by Hoxit (1974) for an average baroclinic PBL range from 0.56 to 1.05 N $m^{-2}$. In the current study, however, values at the top of the surface layer are much smaller, with a mean value of $\sim$0.13 N $m^{-2}$ for each of the RAOB- and satellite-derived modified Ekman and "actual" winds. Since stress in the

surface layer is considered to be constant with height (Hess, 1959; Holton, 1979), the study values are assumed to be representative of stress at the surface. Stress profiles above the surface layer are shown in Fig. 36 for the three wind data sets. ($\tau$ is obtained through (2-1).) "Actual" stress values indicate that the region of maximum baroclinicity occurs at 300 m AGL, the average height (top) of the low level inversion. This maximum (0.157 N $m^{-2}$), however, is also significantly less than Hoxit's values. The RAOB- and satellite-derived profiles show a constant decrease with height, as is "ideally" expected to occur (Hess, 1959).

The degree of baroclinicity can also be inferred from cross-isobaric flow. Ekman winds (as discussed in Chapter 2, Section c) flow toward low pressure at or near the surface, making an angle of $45^{o}$ with the isobars. The modified Ekman equations, however, partially allow for the effects of baroclinicity (via the temperature gradient terms in (3-34) and (3-35)). Thus, a decrease in the cross-isobaric angle at or near the surface is anticipated. In the current study, mean cross-isobaric angles at the top of the surface layer (50 m AGL) are $26.9^{o}$ (with air flowing toward lower pressure) for RAOB-derived modified Ekman winds, and $28.6^{o}$ for their satellite-derived counterparts. "Actual" winds near the surface yield a mean cross-isobaric flow angle of $33.9^{o}$. Strong baroclinicity should yield much smaller crossing angles as the

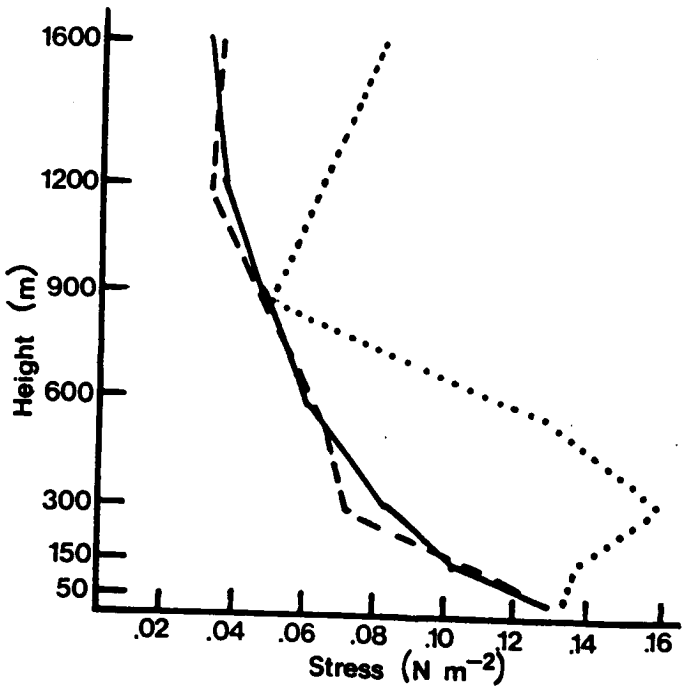


Fig. 36. Stress profiles based on RAOB- (solid) and satellite-derived (dashed) modified Ekman data, as well as "actual" (dotted) winds.

surface winds would be forced (through instability) to flow more parallel to the pressure contours.

# BIBLIOGRAPHY


Alberty, R. L., D. W. Burgess, C. E. Hane, and J. F. Weaver, 1979: Sesame 79 Operations Summary. NOAA/ERL, Boulder, CO, 253 pp.

Arnold, J. E., J. R. Scoggins, and H. E. Fuelberg, 1976: A comparison between Nimbus 5 THIR and ITPR temperatures and derived winds with rawinsonde data obtained in the AVE II experiment. NASA Contractor Report CR-2757, 76 pp.

Arya, S. P. S., and J. C. Wyngaard, 1975: Effect of baroclinicity on wind profiles and the geostrophic drag law for the convective planetary boundary layer. J. Atmos. Sci., 32, 767-778.

Barnes, S. L., 1973: Mesoscale objective map analysis using weighted time series observations. NOAA Tech. Memo. ERL NSSL-62, 60 pp.

Bodin, S., 1980: Applied numerical modeling of the atmospheric boundary layer. Atmospheric Planetary Boundary Layer Physics (A. Longhetto, Ed.), Elsevier Scientific Publishing Company, New York, 1-76.

Boundary Layer Branch, 1967: Wind and temperature profiles from Project Windy Acres. U.S. Air Force Cambridge Res. Lab. Spec. Rep. 65 (AFCRL-67-0339), 36 pp.

Bruce, R. E., L. D. Duncan, and J. H. Pierluissi, 1977: Experimental study of the relationship between radiosonde temperatures and satellite-derived temperatures. Mon. Wea. Rev., 105, 493-496.

Businger, J. A., 1973: Turbulent transfer in the atmospheric surface layer. Workshop on Micrometeorology (D. A. Haugen, Ed.), Amer. Meteor. Soc., 67-100.

Carle, W. E., and J. R. Scoggins, 1981: Determination of wind from Nimbus 6 satellite sounding data. NASA Reference Publication 1072, 72 pp.

Deardorff, J. W., 1972: Parameterization of the planetary boundary layer for use in general circulation models. Mon. Wea. Rev., 100, 93-106.

Dyer, A. J., and B. B. Hicks, 1970: Flux-gradient relationships in the constant flux layer. Quart. J. R. Met.

Soc., 96, 715-721.

Estoque, M. A., 1963: A numerical model of the atmospheric boundary layer. J. Geophys. Res., 68, 1103-1113.

_____, 1973: Numerical modeling of the planetary boundary layer. Workshop on Micrometeorology (D. A. Haugen, Ed.), Amer. Meteor. Soc., 217-270.

Fuelberg, H. E., 1974: Reduction and error analysis of the AVE II pilot experiment data. NASA CR-120496, George C. Marshall Space Flight Center, 364 pp.

Fujita, T. T., E. W. Pearl, and W. E. Shenk, 1975: Satellite-tracked cumulus velocities. J. Appl. Meteor., 14, 407-413.

Gerrity, J. P., 1967: A physical-numerical model for the prediction of synoptic-scale low cloudiness. Mon. Wea. Rev., 95, 261-282.

Hadeen, K. D., 1970: AFGWC boundary layer model. Air Force Global Weather Central Tech. Mem. (AFGWCTM 70-5), 53 pp.

_____, and A. L. Friend, 1972: The Air Force Global Weather Central operational boundary-layer model. Bound.-Layer Meteor., 3, 98-112.

Haltiner, G. T., and R. T. Williams, 1980: Numerical Prediction and Dynamic Meteorology. John Wiley & Sons, New York, 477 pp.

Hasler, A. F., W. E. Shenk, and W. C. Skillman, 1977: Wind estimates from cloud motions: Preliminary results of Phases I, II, and III of an "in situ" aircraft verification experiment. J. Appl. Meteor., 16, 812-815.

_____, W. C. Skillman, W. E. Shenk, and J. Steranka, 1979: "In situ" aircraft verification of the quality of satellite cloud winds over oceanic regions. J. Appl. Meteor., 18, 1481-1489.

Haurwitz, B., 1941: Dynamic Meteorology. McGraw-Hill Book Co., New York, 279 pp.

Hess, G. D., B. B. Hicks, and T. Yamada, 1981: The impact of the Wangara Experiment. Bound.-Layer Meteor., 20, 135-174.

Hess, S. L., 1959: Introduction to Theoretical Meteorology.

Holt, Rinehart and Winston, New York, 362 pp.

Hill, K., G. Wilson, and R. Turner, 1979: NASA's participation in the AVE-SESAME '79 program. Bull. Amer. Meteor. Soc., 60, 1323-1329.

Hillger, D. W. and T. H. Vonder Haar, 1977: Deriving mesoscale temperature and moisture fields from satellite radiance measurements over the United States. J. Appl. Meteor., 16, 715-726.

_____, and _____, 1979: An analysis of satellite infrared soundings at the mesoscale using statistical structure and correlation functions. J. Atmos. Sci., 36, 287-305.

Holton, J. R., 1979: An Introduction to Dynamic Meteorology. Academic Press, New York, 391 pp.

Horn, L. H., R. A. Petersen, and T. M. Whittaker, 1976: Intercomparisons of data derived from Nimbus 5 temperature profiles, rawinsonde observations and initialized LFM model fields. Mon. Wea. Rev., 104, 1362-1371.

Hoxit, L. R., 1974: Plantary boundary layer winds in baroclinic conditions. J. Atmos. Sci., 31, 1003-1020.

Hubert, L. F., and L. F. Whitney, Jr., 1971: Wind estimation from geostationary satellite pictures. Mon. Wea. Rev., 99, 665-672.

Hudson, H. R., 1971: On the relationship between horizontal moisture convergence and convective cloud formation. J. Appl. Meteor., 10, 755-762.

Johnson, G. L., and D. Suchman, 1980: Intercomparisons of SMS wind sets: a study using rapid-scan imagery. Mon. Wea. Rev., 108, 1672-1688.

Krishna, K., 1981: A two-layer first-order closure model for the study of the baroclinic atmospheric boundary layer. J. Atmos. Sci., 38, 1401-1417.

Lambeth, R. L., 1966: On the use of Court's versus Durst's techniques for computing vector correlation coefficients. J. Appl. Meteor., 5, 736-737.

Lenhard, R. W., 1970: Accuracy of radiosonde temperature and pressure height determination. Bull. Amer. Meteor. Soc., 51, 842-846.

Lettau, H. H., and B. Davidson, 1957: Exploring the Atmosphere's First Mile, Vols. 1 and 2. Pergamon Press, New York, 376 pp and 578 pp, respectively.

Lowe, P. R., 1977: An approximating polynomial for the computation of saturation vapor pressure. J. Appl. Meteor., 16, 100-103.

Mancuso, R. L., and R. M. Endlich, 1980: Satellite wind-profile techniques. Naval Environment Prediction Research Facility Contractor Report (NAVENVPREDRSCHFAC CR 80-05), 65 pp.

Mellor, G. L., and T. Yamada, 1974: A heirarchy of turbulence closure models for planetary boundary layers. J. Atmos. Sci., 31, 1791-1806.

Moyer, V., J. R. Scoggins, N. M. Chou, and G. S. Wilson, 1978: Atmospheric structure deduced from routine Nimbus 6 satellite data. Mon. Wea. Rev., 106, 1340-1352.

Negri, A. J., and T. H. Vonder Haar, 1980: Moisture convergence using satellite-derived wind fields: A severe local storm case study. Mon. Wea. Rev., 108, 1170-1182.

O'Brien, J. J., 1970: An alternate solution to the classical vertical velocity problem. J. Appl. Meteor., 9, 197-203.

Panofsky, H. A., and G. W. Brier, 1968: Some Applications of Statistics to Meteorology. Pennsylvania State University Press, 224 pp.

Peslen, C. A., 1980: Short-interval SMS vector determinations for a severe local storm area. Mon. Wea. Rev., 108, 1407-1418.

Petersen, R. A., and L. H. Horn, 1977: An evaluation of 500 mb height and geostrophic wind fields derived from Nimbus 6 soundings. Bull. Amer. Meteor. Soc., 58, 1195-1201.

Phillips, N. A., L. M. McMillin, A. Gruber, and D. A. Wark, 1979: An evaluation of early operational temperature soundings from TIROS-N. Bull. Amer. Meteor. Soc., 60, 1188-1197.

Prandtl, L., 1934: The mechanics of viscous fluids. Aerodynamic Theory (W. Durand, Ed.), Stanford University Press, 34-208.

Priestly, C. H. B., 1959: Turbulent Tranfer in the Lower

Atmosphere. University of Chicago Press, Chicago, 130 pp.

Rao, G. V., and A. W. Hassebrock, 1972: Mesoscale latent heat release and its influence on the mid-tropospheric warming. J. Appl. Meteor., 11, 1271-1283.

Rubenstein, D. M., 1981: The daytime evolution of the East African jet. J. Atmos. Sci., 38, 114-128.

Saucier, W. J., 1955: Principles of Meteorological Analysis. University of Chicago Press, Chicago, 438 pp.

Schlatter, T. W., 1980: An evolution of TIROS-N temperature retrievals and their use in determining large-scale vertical structure of the atmosphere. International Conference on Preliminary FGGE Data Analysis and Results, World Meteorological Organization, Bergen, Norway, 12-20.

_____, 1981: An assessment of operational TIROS-N temperature retrievals over the United States. Mon. Wea. Rev., 109, 110-119.

Scoggins, J. R., W. E. Carle, K. Knight, V. Moyer, and N. Cheng, 1981: A comparative analysis of rawinsonde and Nimbus 6 and TIROS-N satellite profile data. NASA Reference Publication 1070, 71 pp.

Shen, W. C., W. L. Smith, and H. M. Woolf, 1975: An intercomparison of radiosonde and satellite-derived cross sections during the AMTEX. NOAA Technical Report NESS 72, 18 pp.

Smith, W. L., and H. M. Woolf, 1974: An intercomparison of meteorological parameters derived from radiosonde and satellite vertical temperature cross sections. NOAA Technical Report. NESS 71, 13 pp.

_____, _____, C. M. Hayden, and W. C. Shen, 1975: Nimbus 5 sounder data processing system; Part II: Results. NOAA Technical Memorandum NESS 57, 15 pp.

_____, _____, _____, H. B. Howell, and F. W. Nagle, 1978: Interactive processing of TIROS-N sounding data. Conference on Weather Forecasting and Analysis and Aviation Meteorology, Oct. 16-19, 1978, American Meteorological Society, 390-395.

_____, _____, _____, D. Q. Wark, and L. M. McMillin, 1979: The TIROS-N operational vertical

sounder. Bull. Amer. Meteor. Soc., 60, 1177-1187.

_____, F. W. Nagle, C. M. Hayden, and H. M. Woolf, 1981: Vertical mass and moisture structure from TIROS-N. Bull. Amer. Meteor. Soc., 62, 388-393.

Suchman, D., and D. W. Martin, 1976: Wind sets from SMS images: An assessment of quality for GATE. J. Appl. Meteor., 15, 1265-1278.

Sutton, O. G., 1977: Micrometeorology. Krieger Publishing Company, New York, 333 pp.

Wieringa, J., 1980: A revaluation of the Kansas mast influence on the measurements of stress and cup anemometer overspeeding. Bound.-Layer Meteor., 18, 411-430.

Williams, S. F., M. L. Gerhard, and R. E. Turner, 1980a: AVE-SESAME II: 25-mb sounding data. NASA TM-78281, George C. Marshall Space Flight Center, 373 pp.

_____, N. Horvath, and R. E. Turner, 1980b: A preliminary look at AVE-SESAME II conducted on April 19-20, 1979. NASA TM-78280, George C. Marshall Space Flight Center, 50 pp.

Wilson, T. A., and D. D. Houghton, 1979: Mesoscale wind fields for a severe storm situation determined from SMS cloud observations. Mon. Wea. Rev., 107, 1198-1209.

Wyngaard, J. C., S. P. S. Arya, and O. R. Cote, 1974: Some aspects of the structure of convective planetary boundary layers. J. Atmos. Sci., 31, 747-754.

Yates, H. W., 1974: Limitations and prospects for atmospheric sounding. Proc. Photo-Opt. Instrum. Eng., 51, 1-20.